UNIVERSITY OF CALIFORNIA, SAN DIEGO

Quantitative Nondestructive Testing using Infrared Thermography

A dissertation submitted in partial satisfaction of the
requirements for the degree
Doctor of Philosophy

in

Structural Engineering

by

Arun Manohar

Committee in charge:

Professor Francesco Lanza di Scalea, Chair
Professor William Hodgkiss
Professor Hyonny Kim
Professor Michael Todd
Professor Mohan Trivedi

2012

The dissertation of Arun Manohar is approved, and it is acceptable in quality and form for publication on microfilm and electronically:

_____

_____

_____

_____

_____

Chair

University of California, San Diego

2012

DEDICATION

To my family.

EPIGRAPH

A man is but the product of his thoughts; what he thinks, he becomes.

—Mahatma Gandhi

TABLE OF CONTENTS

LIST OF FIGURES

LIST OF TABLES

ACKNOWLEDGEMENTS

Imagine sitting in the "Hollywood Tower" ride at the Disney's California Adventure Park. You don't know when you are about to rapidly accelerate up, or when you are going to accelerate down. My Ph.D. has been an exciting journey filled with lots of highs and lows.

If not for an email from Prof. Francesco Lanza di Scalea in the spring of 2007, this Ph.D. would not have happened. I would like to express my sincerest gratitude to Prof. Lanza di Scalea and I am very thankful to him. This work would not have been possible without his advice and support. He gave me lots of freedom to explore the problems that interested me, while providing me with the direction that I needed. The skills that I developed during these five years have helped me professionally and personally.

Thanks to my committee members Prof. Michael Todd, Prof. Mohan Trivedi, Prof. Hyonny Kim and Prof. William Hodgkiss, for their advice and suggestions during the course of my study. Special thanks to Prof. Michael Todd and Prof. Mohan Trivedi for guiding me when I was stuck in certain problems.

Thanks to my colleagues at the NDE-SHM Lab, Ivan Bartoli, Stefano Coccia, Salvatore Salamone, Giuseppina Vitale, Ankit Srivastava, Robert Phillips, Claudio Nucera, Jeffery Tippmann, Xuan Zhu, Stefano Mariani and Thompson Nguyen, for the collaboration and friendship.

Thanks to staff at the Structural Engineering department, Daryl Rysdyk, Debra Bomar, Raquel Hall, Sonya Wilson, Jeannette Ng and Lindsay Walton, for helping with administrative matters.

My friends, Harish Nagarajan, Damian del Toro, Balaji Sriram, Rajaram Narayanan, Aravind Iyengar, Nitin Udpa and Saurabh Prasad, made me feel at home in UCSD. Special thanks to Harish and Damian for the wonderful friendship, help, advice and thought-provoking discussions.

My family has been a solid support. I would like to thank my father, mother, sister and wife for the unconditional love and unwavering support through these years. Special thanks to my wife and best friend, Chatura. If not for her, this Ph.D. would have taken much longer.

Thanks to Mark Rumsey and Dennis Roach of Sandia National Laboratories for advice on the design and defect lay-out of the CX-100 wind turbine blade.

The research presented in this thesis has been partially funded by the NSF grant # 0729760, NSF grant #1028365 and the von Liebig center at the University of California, San Diego through a DoE Fellowship.

Chapter 2, in part, has been published in Experimental Techniques journal, Manohar, Arun; Lanza di Scalea, Francesco; (2011). The title of this paper is *Wavelet aided Multivariate Outlier Analysis to enhance defect contrast in thermal images.* The dissertation author was the primary investigator and primary author of this paper.

Chapter 3, in part, has been submitted for publication in the Structural Health Monitoring journal, Manohar, Arun; Lanza di Scalea, Francesco; (2012). The title of this paper is *Detection of Defects in Wind Turbine Composite Blades using Statistically-Enhanced Lock-In Thermography.* The dissertation author was the primary investigator and primary author of this paper.

Chapter 4, in part, has been published in the Experimental Mechanics journal, Manohar, Arun; Lanza di Scalea, Francesco; (2012). The title of this paper is *Determination of Defect Depth and Size using Virtual Heat Sources in Pulsed Infrared Thermography.* The dissertation author was the primary investigator and primary author of this paper.

Chapter 5, in part, has been submitted for publication in the Experimental Mechanics journal, Manohar, Arun; Lanza di Scalea, Francesco; (2012). The title of this paper is *Estimation of Defect Size and Depth in Quasi-Isotropic Composite Materials Using Infrared Thermography.* The dissertation author was the primary investigator and primary author of this paper.

VITA

2007	B.Tech. in Aerospace Engineering, Indian Institute of Technology, Madras, India
2009	M.S. in Structural Engineering, University of California, San Diego
2012	Ph.D. in Structural Engineering, University of California, San Diego

JOURNAL ARTICLES, CONFERENCE PROCEEDINGS AND PATENTS

Manohar, A., Lanza di Scalea, F., "Wavelet aided Multivariate Outlier Analysis to Enhance Defect Contrast in Thermal Images", *Experimental Techniques*, 2011.

Manohar, A., Lanza di Scalea, F., "Determination of Defect Depth and Size using Virtual Heat Sources in Pulsed Infrared Thermography", *Experimental Mechanics*, 2012.

Manohar, A., Lanza di Scalea, F., "Detection of Defects in Wind Turbine Composite Blades using Statistically-Enhanced Lock-In Thermography", Submitted to *Structural Health Monitoring*, 2012.

Manohar, A., Lanza di Scalea, F., "Estimation of Defect Size and Depth in Quasi-Isotropic Composite Materials Using Infrared Thermography", Submitted to *Experimental Mechanics*, 2012.

Lanza di Scalea, F. and Manohar, A., "Object Identification by Multispectral Fusion and Haar Classification", *Proceedings of the NSF Civil, Mechanical, and Manufacturing Innovation (CMMI) Engineering Research and Innovation Conference, Honolulu, Hawaii*, 2009.

Manohar, A. and Lanza di Scalea, F., "Object Identification by Multispectral Fusion and Haar Classification", *Proceedings of SPIE Smart Structures/NDE 17th Annual International Symposium Sensors and Smart Structures Technologies for Civil, Mechanical and Aerospace Systems, San Diego, CA*, Volume 7647, pp. 76471Q-1-7, 2010.

Manohar, A. and Lanza di Scalea, F., "Wavelet Aided Multivariate Outlier Analysis to Enhance Defect Contrast in Thermal Images", *Proceedings of the SPIE*, Volume 7981, 2011.

Tippmann, J., Manohar, A. and Lanza di Scalea, F., "Wind Turbine Blade Inspection Tests at UCSD", *Sensors and Smart Structures Technologies for Civil, Mechanical, and Aerospace Systems 2012. Proceedings of the SPIE*, Volume 8345, 2012.

Manohar, A., Tippmann, J. and Lanza di Scalea, F., "Localization of Defects in Wind Turbine Blades and Defect Depth Estimation using Infrared Thermography", *Sensors and Smart Structures Technologies for Civil, Mechanical, and Aerospace Systems 2012. Proceedings of the SPIE*, Volume 8345, 2012.

Manohar, A. and Lanza di Scalea, F., "A Fast Lock-In Infrared Thermography Implementation to Detect Defects in Composite Structures Like Wind Turbine Blades", *Quantitative Nondestructive Evaluation*, 2012.

Manohar, A., Lanza di Scalea, F., "Wavelet aided Multivariate Outlier Analysis to Enhance Defect Contrast in Thermal Images", *Provisional U.S Patent #61624232*, April 2012.

ABSTRACT OF THE DISSERTATION

Quantitative Nondestructive Testing using Infrared Thermography

by

Arun Manohar

Doctor of Philosophy in Structural Engineering

University of California, San Diego, 2012

Professor Francesco Lanza di Scalea, Chair

Nondestructive Testing (NDT) is an important tool to increase the service life of critical structures. Infrared Thermography is an attractive NDT modality because it is a non-contact technique, and it has full-field defect imaging capability. Typically, two problems are relevant in the domain of NDT of structures. The first problem deals with the detection of defects, while the second problem is based on estimating the defect parameters like size and depth. This dissertation aims at enhancing the capability of Infrared Thermography NDT vis-a-vis defect detection and defect quantification in metal and composite structures.

In this dissertation, detection of defects was performed using two active thermography techniques – Pulsed Thermography and Lock-In Thermography. A

two-stage signal reconstruction approach based on Pulsed Thermography was developed to analyze raw thermal data. In the first stage, the data was low-pass filtered using Wavelets. In the second stage, a Multivariate Outlier Analysis was performed on filtered data using a set of signal features. The proposed approach significantly enhances the defective area contrast against the background. In the second part of the study, a Lock-In Thermography technique was developed to detect defects present in a 9m CX-100 wind turbine blade. A set of image processing algorithms and Multivariate Outlier Analysis were used in conjunction with the classical Lock-In thermography technique to counter the "blind frequency" effects and to improve the defect contrast. Receiver Operating Characteristic curves were used to quantify the gains obtained.

Following detection of defects, the determination of defect depth and size was addressed. The problem of defect depth estimation has been previously studied using 1D heat conduction models. Unfortunately, 1D heat conduction based models are generally inadequate in predicting heat flow around defects, especially in composite structures. A novel approach based on virtual heat sources was proposed in this dissertation to model heat flow around defects accounting for 2D axisymmetric heat conduction. The proposed approach was used to quantitatively determine the defect depth and size in isotropic materials. Further, the approach was extended to model 3D heat conduction in quasi-isotropic composite structures. The approach used the excess temperature profile that was obtained over a defective area with respect to a sound area to estimate the defect dimensions and depth. Using coordinate transformations, the anisotropic heat conduction problem was reduced to the isotropic domain, followed by separation of variables to solve the resulting partial differential equation. Relevant experiments were performed to validate the proposed theory.

Chapter 1

Introduction

1.1 Nondestructive Testing

Nondestructive Testing (NDT) encompasses a wide variety of analysis techniques used to evaluate the properties and integrity of a test specimen without causing any damage [1, 2]. Since NDT does not affect the properties of the specimen being inspected, it is a highly valuable technique that can save resources and extend the useful life of the test specimen. NDT has a wide variety of applications in the fields of aviation, railways, transportation, manufacturing, automotive, powerplants, civil structures, art and medicine, to name a few. Commonly NDT of structures is performed using, but it is not limited to, ultrasound [3], Radiographic testing [4], Magnetic-Particle inspection [5], Liquid Penetrant testing [6], eddy-current testing [7], Shearography [8], Acoustic Emission testing [9] and Infrared Thermography [10].

1.2 Infrared Thermography in NDT

Infrared Thermography [10–30] deals with detection of subsurface damage by monitoring the temperature differences that are observed on the surface of the test specimen with an Infrared camera. Infrared Thermography is an attractive technique because it is a non-contact technique and it is capable of rapid, wide-area inspection. Infrared Thermography is is based on the measurement of radiated electromagnetic energy. The energy emitted by a surface at a given temperature is called the "spectral radiance" and is defined by the Planck's law. An Infrared camera is a spectral radiometer measuring this energy and with appropriate calibration based on the Planck's law, allows to retrieve the temperature distribution on the surface of interest [10]. The emissivity of a material is the relative ability of its surface to emit energy by radiation, and it is denoted by e. Values of e lie between 0 to 1. An emissivity value of 0, corresponds to a perfect reflector, while an emissivity of 1, corresponds to a perfect emitter, also called a "blackbody". Emissivity depends on surface orientation, temperature, and wavelength, although, for practical reasons, it is usually considered a constant. A surface having a low emissivity acts like a mirror and makes Infrared Thermography measurements difficult

since spurious radiations emitted by neighboring bodies affect the readings through reflections. In order to avoid that, a thin layer of a high emissivity black colored paint is applied over the surface to be inspected.

Two modes of Infrared Thermography are commonly used in NDT of structures – passive mode and active mode [17, 31–33]. In the passive mode, the defective areas are naturally at a different temperature than the surroundings. Common applications of the passive Infrared Thermography mode in NDT are for the evaluation of buildings, bridges and components. In these applications, abnormal temperature profiles indicate a potential problem relevant to detect. In passive thermography, the temperature difference with respect to the surrounding, often referred to as the ΔT, is a critical parameter. A ΔT of about $4°C$ value is a strong evidence of abnormal behavior and it indicates the presence of an underlying defect [10]. In these applications, passive thermography provides qualitative, but not a quantitative estimate of the damage present.

In the case of active mode [6, 17], an external loading is necessary to induce noticeable thermal contrasts between the defective and sound areas since the test specimen is at uniform temperature prior to the loading. Various modes of thermal loading are possible, and have been studied in literature. The active mode can further be sub-classified based on the source of external loading into Pulsed Thermography, Lock-In Thermography and Vibrothermography [34–39]. The active mode has numerous applications in NDT. Moreover, since the characteristics of the external loading is known along with the material geometry and properties, quantitative measurement and characterization is possible. This aspect of active mode will be subject of this dissertation and it will be discussed in detail in the following chapters.

1.2.1 Pulsed Thermography

In Pulsed Thermography [7, 15, 18, 20, 21, 27, 40–50], the specimen to be inspected is rapidly heated by a "pulse" of thermal energy, which instantaneously heats the front surface of the object. The rate of cooling of the front surface is recorded using an Infrared camera. A typical schematic of the Pulsed Thermogra-

phy setup is shown in Figure 1.1. The temperature of the surface changes rapidly after the initial thermal pulse because the thermal front propagates to the interior of the test specimen, by diffusion. The radiation and convection losses though present, are assumed to be minimal. The presence of a defect offers resistance to the thermal front, hence reducing the diffusion rate. Consider two points, 1 and 2, on the surface of the test specimen containing a defect as shown in Figure 1.2. The rate of cooling at point 2 is much slower than point 1, due to the resistance offered by the defect present directly underneath point 2. Due to this, the areas present over the defect cool at a slower rate. The defects appear on the surface as areas of hotter temperatures with respect to surrounding areas without defects as shown in Figure 1.3. Since the thermal front needs more time to reach the deeper sections, deeper defects will be observed at a later time instant as a hot-spot with reduced contrast.

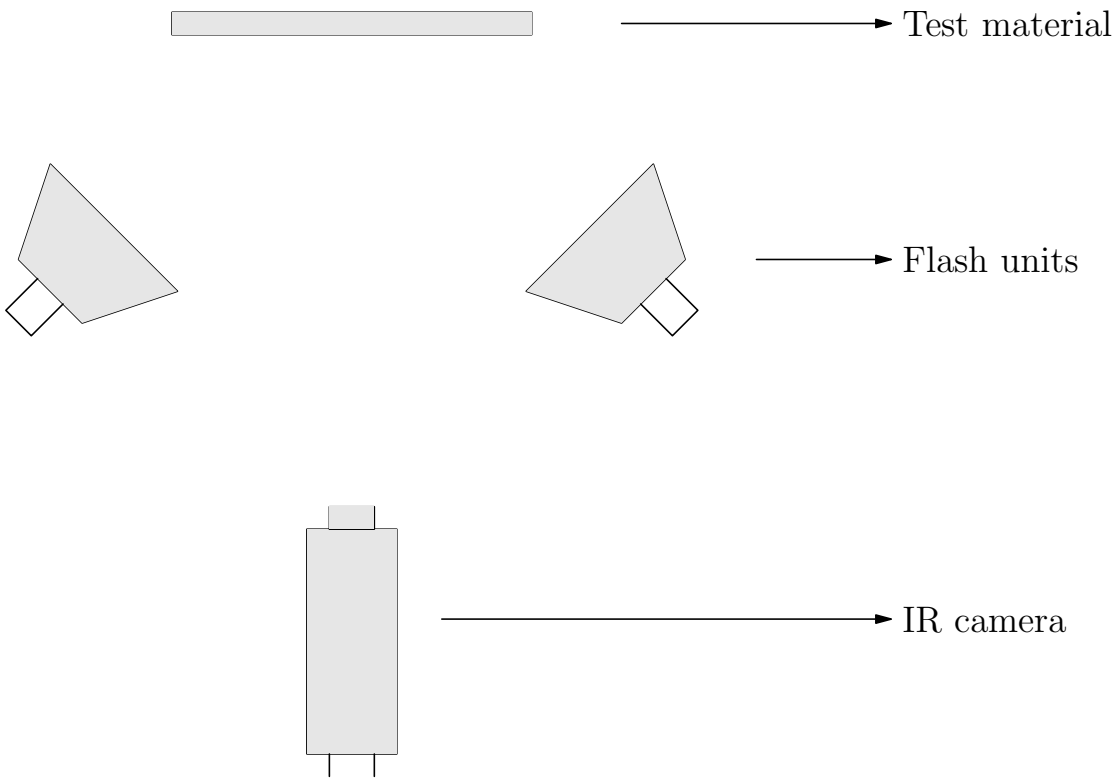

Figure 1.1: A typical Pulsed Thermography setup

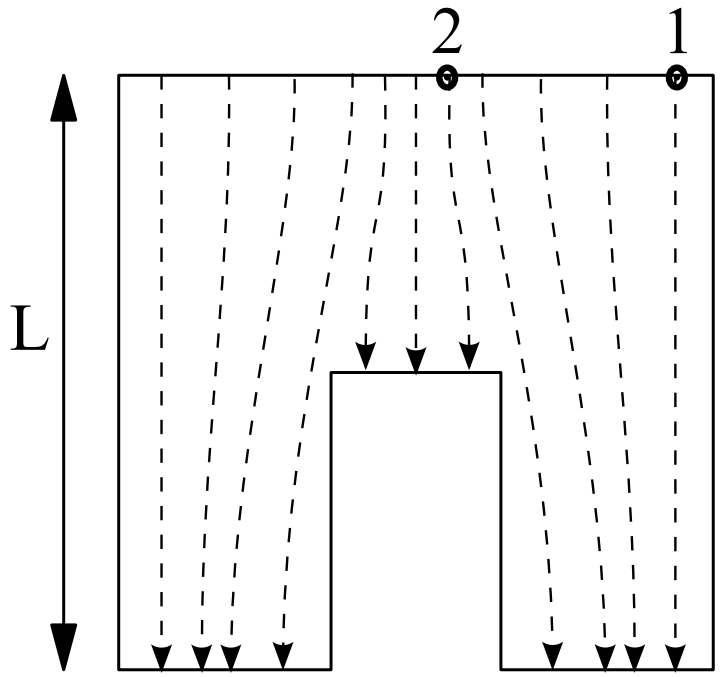

Figure 1.2: Resistance offered by the presence of defect to the pulsed heating

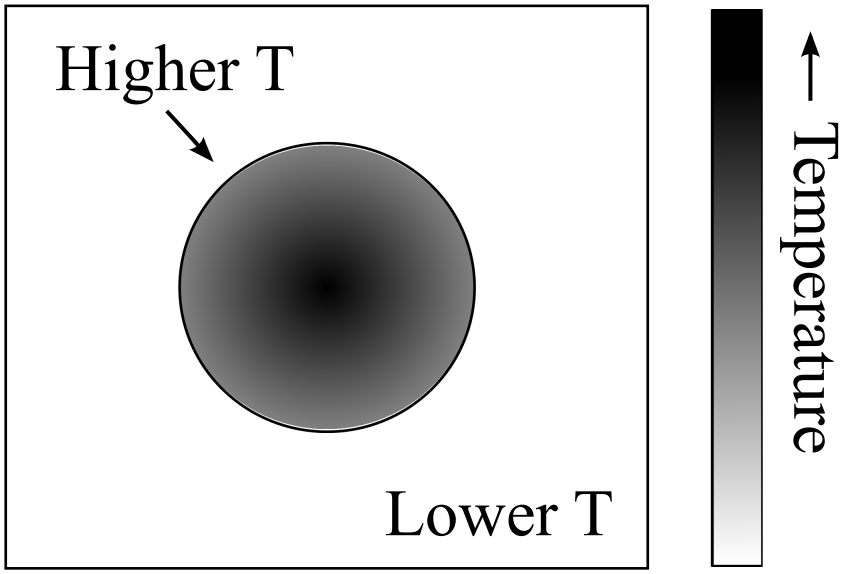

Figure 1.3: The hot-spots indicate the presence of a underlying defect

1.2.2 Lock-In Thermography

Lock-In Thermography [26, 28, 35, 41, 51–55] is based on the application of a periodic thermal energy input to the surface of the object. This technique is particularly effective to detect defects in thick composite structures. When the resulting heat wave encounters a defect, some of it is reflected, causing a phase shift with respect to the input heat wave. The Lock-In Thermography setup is similar to the one used in Pulsed Thermography, except that halogen lamps that are capable of continuous heating are used instead of strobes. In Lock-In Thermography, phase and magnitude images become available through simple FFT operations at every spatial point. One of the main advantages in using Lock-In Thermography is that, the phase image is insensitive to non-uniform heating and local emissivity variations. Typically, slow sinusoidal heating is used, the frequency of which is decided based on the maximum depth that needs to be inspected. The thermal diffusion length, z, is related to the thermal conductivity of the material, k, density, ρ, Lock-In frequency, f, and specific heat conductivity, c, by,

$$z = \sqrt{\frac{k}{\pi f \rho c}} \tag{1.1}$$

Based on Equation 1.1, it is clear that higher Lock-In frequencies will restrict the analysis in a near-surface region, while lower frequencies will allow to probe deeper under the surface.

1.3 Post-Processing in Infrared Thermography

It is very difficult to isolate the defective areas from the raw thermal image sequence as the data is corrupted with noise. Post-processing in Infrared Thermography plays a very important part. Various kinds of signal processing methods are used to eliminate this noise and to enhance the defect signature. Most of the existing methods require user input or intervention, and automation is not usually possible. A brief summary of some of the popular methods is presented.

Almost all the existing post processing methods for Thermographic NDE are based on the basic 1D heat conduction model is given in Equation (1.2). The

model holds well for thin plates and short time.

$$\frac{\partial^2 T}{\partial^2 z} - \frac{1}{\alpha}\frac{\partial T}{\partial t} = 0 \tag{1.2}$$

where T is the temperature, z is the one dimensional through thickness spatial coordinate, t is the time and α is the thermal diffusivity of the test material.

Absolute Thermal Contrast was one of the earliest post processing methods used to enhance the thermal signature of the defective areas [31,45]. A typical cooling curve that is expected across sample Sound and Defective area is represented in Figure 1.4. The rate at which the temperature falls across the Defective area is slower compared to Sound area. This is due to the resistance offered to the flow of heat by the defect. The thermal contrast is mathematically represented using the simple definition, $\Delta T(t) = T_{defective}(t) - T_{sound}(t)$ and a typical trend is shown in Figure 1.5. While the implementation is simple, the method suffers from a couple of disadvantages. The definition of the sound area (area without any defects) requires operator input and the choice affects considerably the results. Secondly, since the method involves differences, the presence of noise in the raw data plays a significant effect on the results.

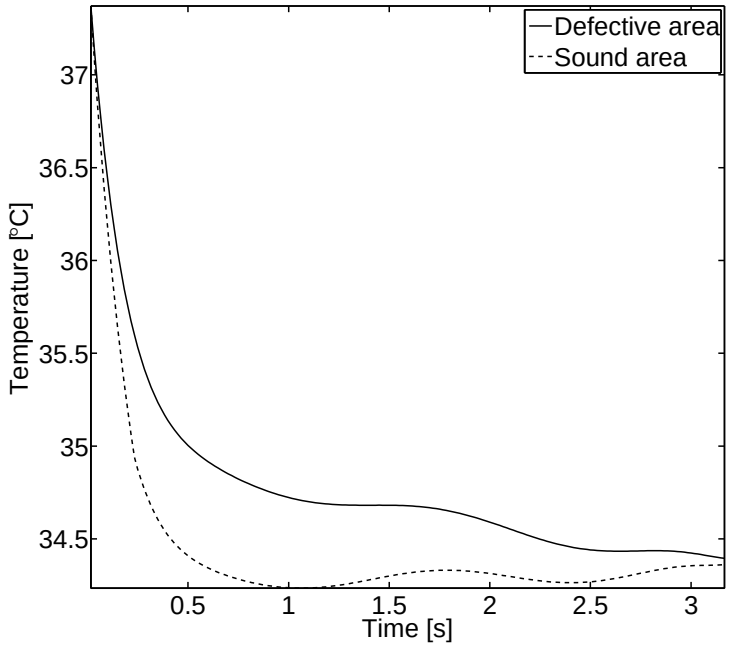

Figure 1.4: Expected cooling profiles at sample Sound and Defective areas

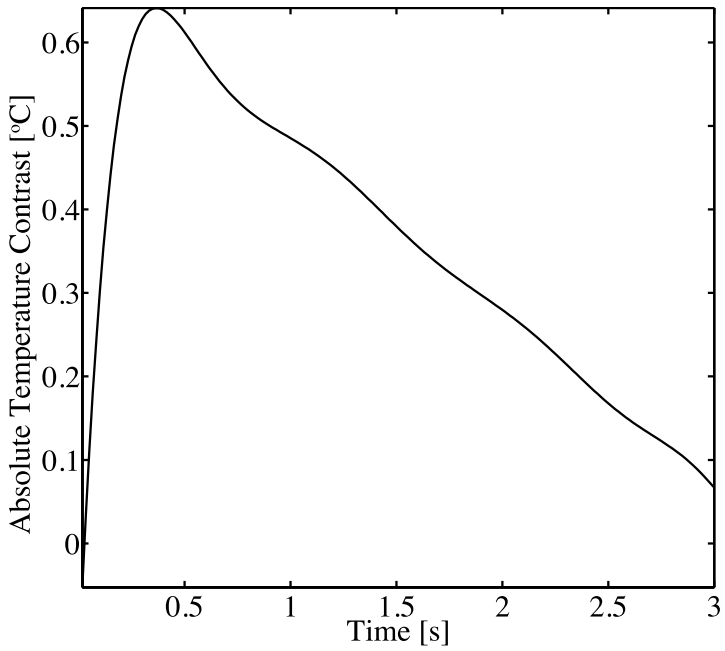

Figure 1.5: Absolute Temperature Contrast based on based on cooling profiles at sample Sound and Defective area

The Differential Absolute Contrast (DAC) is an alternate method that does not require the specification of Sound Area [27]. Instead of looking for an area without any defects, the time instant when the defect first starts showing up at a pixel is treated as the reference time. At each pixel, this reference time is calculated. This requires an iterative approach. The thermal contrast at each pixel is represented as a function of the time instant t as,

$$\delta T = T_{def}(t) - \sqrt{\frac{t'}{t}} T(t') \tag{1.3}$$

where t' is a time instant when there is no indication of the defect yet.

Sun [48] proposed the least-squares fitting method to fit the raw thermal data as shown in Equation (1.4).

$$T(t) \approx A \left[1 + 2 \sum_{n=1}^{\infty} exp\left(-\frac{n^2 \pi^2 \alpha t}{L^2} \right) \right] - st \tag{1.4}$$

The slope s is determined by linear fitting of the experimental data in the time period $\frac{L^2}{2\alpha} < t < \frac{3L^2}{2\alpha}$. Equation (1.4) is valid for the time instants $0 < t < \frac{3L^2}{2\alpha}$. For a

case of defect free sample, s is zero. The approach is robust to non-uniform heating and also more accurate compared to conventional methods as it partly accounts for the three dimensional conduction effects by incorporating the constant slope decay term. Since the method involves curve fitting, the undesirable effects on high frequency temporal noise is minimal. The main disadvantage of the least-squares fitting approach is the need for operator intervention in calculating the slope s at every spatial point in the field.

In Pulsed Phase Thermography [15,18,19,50], the time domain data is converted to the frequency domain using the Fast Fourier transform(FFT) algorithm. The frequency domain data includes both the amplitude and phase information. The phase information is less affected by non-uniform heating, surface geometry and irregularities than the raw thermal data. Different techniques have been proposed to compute the depth of the defect L using the phase component of the raw thermal data. One such definition is shown in Equation (1.5). [19]

$$L = C\sqrt{\frac{\alpha}{\pi f_b}} \tag{1.5}$$

Where, f_b is defined as the "blind frequency" (the frequency in [Hz] at which a defect located at a particular depth shows enough phase contrast to be detected), and C is an experimental constant that usually lies between 1.5 to 2. While this method is pretty robust in handling non-uniform heating and surface irregularities, operator intervention is required in specifying the blind frequency, f_b. Moreover, the constant C varies among different materials, and the presence of high frequency noise in the raw data significantly affects the results.

To address some of the shortcomings of the discussed methods, the Thermosonic Reconstruction method (TSR) was developed by Shepard et al [32]. In this method, the time history at every spatial point is compared to a 1D heat conduction model in the logarithmic domain where deviations from ideal behavior are readily noticeable. This approach also serves as a low-pass filter, which effectively removes the temporal noise in the time sequence. If Q is the input energy and e is the thermal effusivity of the material, the solution to Equation (1.2) at the object surface(z=0) is $T = \frac{Q}{e\sqrt{\pi t}}$ [29, 32, 44, 46, 47]. By taking the logarithm on

both sides, this can be written as,

$$\ln(T) = \ln\left(\frac{Q}{e}\right) - \frac{1}{2}\ln(\pi t) \tag{1.6}$$

From Equation (1.6), it is evident that the temporal temperature variation at a point is separated from the material properties and the input energy. A significant advantage is that no reference point is required in this method. The logarithmic series is now fit using a simple low order polynomial function so as to eliminate the high frequency temporal noise while preserving the underlying thermal response.

$$\ln[(T(t)] = a_0 + a_1[\ln(t)]^1 + \ldots a_5[\ln(t)]^5 \tag{1.7}$$

Based on Equation (1.7), it is clear that the entire time series at a spatial location can be represented using the coefficients $a_1, a_2 \ldots a_5$. Significant data compression is achieved in the process. Once the reconstruction is performed, the original time series can be obtained by performing a simple mathematical operation,

$$T(t) = exp\left[a_0 + a_1[\ln(t)]^1 + \ldots a_5[\ln(t)]^5\right] \tag{1.8}$$

From Equation (1.8), the rate of cooling can be obtained using the first derivative. This enables early detection of the defective areas as 3D conduction effects cause blurring at later time instants. One of the main drawbacks of the method is the aggressive low-pass filtering of the data, which may miss subtle defects. Performance of the algorithm can also significantly vary as the order of polynomial is changed. Figure 1.6 presents the TSR results obtained over three skin-skin delaminations of sizes 2", 1" and 0.5", present in a composite wind turbine blade at a depth of 0.7mm from the surface. A polynomial of order 5 was used.

Principal Component Thermography (PCT) [22, 56–60] is another widely used technique to process raw thermal data. The technique is based on a Singular Value Decomposition (SVD) of the measured thermal data. When the data is subjected to SVD, numerous orthogonal functions are possible. Typically, the first two orthogonal functions capture most of the significant spatial variations from the data. The first mode corresponds to an exponential decay, very similar

to overall heat decay profile measured at the front surface. The second mode, however, corresponds to the contrast signal produced by defects. This leads to a very compact representation of the entire raw data. Figure 1.7 presents the PCT results obtained over three skin-skin delaminations of sizes 2", 1" and 0.5", present in a composite wind turbine blade at a depth of 0.7mm from the surface.

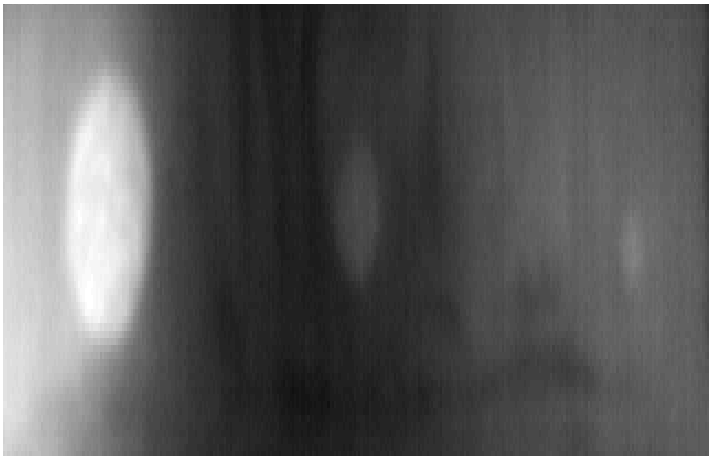

Figure 1.6: TSR applied over an area containing three skin-skin delaminations of sizes 2", 1" and 0.5" present at depth of 0.7mm from the surface in a composite wind turbine blade after a time of 2s has elapsed

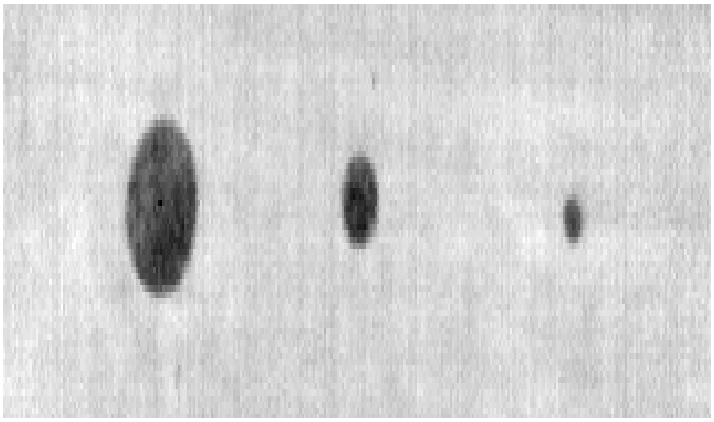

Figure 1.7: PCT applied over an area containing three skin-skin delaminations of sizes 2", 1" and 0.5" present at depth of 0.7mm from the surface in a composite wind turbine blade

1.4 Equipment Used in Infrared Thermography

Infrared Camera: A FLIR^{TM} A320G Infrared camera was used for the Pulsed Thermography and Lock-In Thermography experiments performed in this dissertation. The camera is shown mounted in Figure 1.8. The specifications of the camera are shown in Table 1.1.

Table 1.1: Specifications of the FLIR^{TM} A320G Infrared camera

Detector Type	Focal Plane Array (FPA), uncooled microbolometer
Spectral Range	7.5-13 μm
Resolution	240x320 pixels
Detector Pitch	25 μm
Detector Time Constant	12ms
Lens Material	Germanium
Field of View	$25^\circ \times 19^\circ$
Close Focus Limit	0.4m
Focal Length	18mm
Spatial Resolution	1.36mrad
F-number	1.3
Thermal Sensitivity	50mK
Maximum Image Frequency	60Hz
Focus	Automatic or Manual
Communication Type	Gigabit Ethernet
Supply Voltage	12/24V DC
Operating Temperature	$-15^\circ C - 50^\circ C$
Weight	0.7kg
Dimensions	170mmx70mmx70mm
Housing Material	Aluminum
Base Mounting	2xM4 thread mounting

Figure 1.8: FLIR^{TM} A320G Infrared camera

Lighting Power: A Speedotron^{TM} 4803cx powerpack was used in the Pulsed Thermography experiments to power the Speedotron^{TM} 206VF strobes. The powerpack is capable of emitting a maximum power of 4800Ws at a recycle rate of 4s. The weight of the powerpack is 37pounds and the dimensions are 9"x14"x14" and is shown in Figure 1.9.

Figure 1.9: Speedotron^{TM} 4803cx powerpack

Strobes: A pair of Speedotron^{TM} 206VF strobes as shown in Figure 1.10 were used in the Pulsed Thermography experiments to apply thermal loading on the test specimen's surface. The 206VF light unit couples with the full power outlets on the 4803cx power supply, and emits 4800Ws of power. The 206VF features a plug-in vented flash tube, noiseless fan cooling, switched 250W quartz model lamp to test the coverage area, tube cover and a 11.5" reflector. It also has a focusing reflector mount which can be used to control the coverage angle of the flash from narrow to wide. The strobe body is a uni-body construction utilizing a tough, high glass-fill nylon, and has a detachable stand mount.

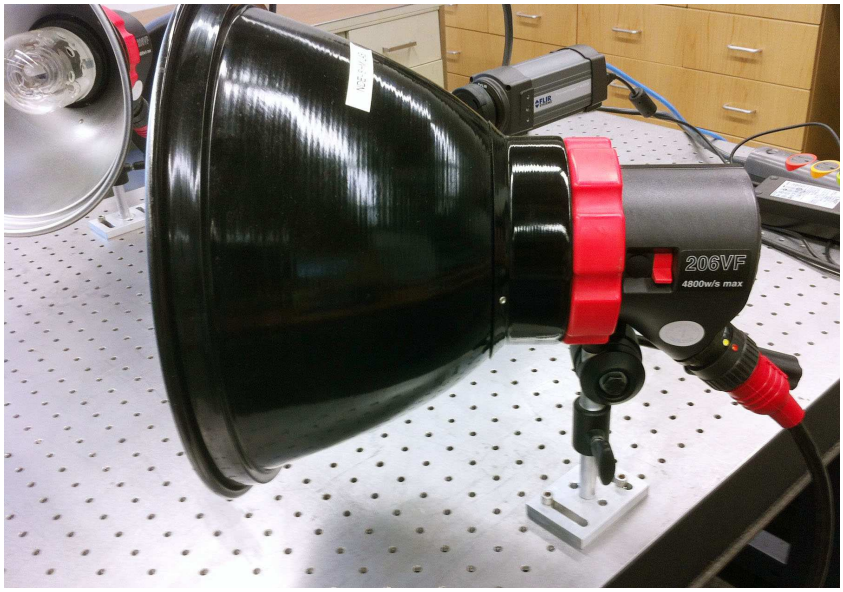

Figure 1.10: Speedotron^{TM} 206VF strobes

Halogen Lamps: A pair of Husky^{TM} halogen lamps was used in the Lock-In Thermography experiments to apply the continuous thermal loading. Each of the lamps were rated at a maximum power of 700W, making the total power output at 1400W. Each lamp contained two halogen bulbs that were rated at 500W and 200W. The halogen lamp setup is shown in Figure 1.11 and are supported on a pair of air-cushioned Manfrotto^{TM} 1052BAC light stands to isolate vibrations. The stands have three sections with a maximum height of 7.75'. They weigh 2.65 pounds and support a maximum weight of 11 pounds.

Figure 1.11: Husky^{TM} Halogen lamps

Function Generator: An Agilent^{TM} 33250A function generator was used in the Lock-In Thermography experiments. The function generator is shown in Figure 1.12 (Image courtesy – www.agilent.com) and was used to generate sinusoidal signals at frequencies ranging from 30mHz-70mHz. The corresponding time periods of the signals were in the range of 14.28s–33.33s. The sinusoids ranged from 0–10V DC and they had a mean voltage level of 5V DC.

Figure 1.12: Agilent^{TM} 33250A function generator

Lighting Dimmer Pack: A Leviton^{TM} DDS6000 dimming system was used to amplify the output of the function generator. The dimming pack weighs 14 pounds and measures at 10"x4"x11", it is shown in Figure 1.13. The dimmer pack is capable of outputting through four channels at 1200W per channel. The maximum total possible output of the system is 2400W. The dimmer contained a 400μs toroidal filtering circuit and a "soft start" option to prolong lamp life. The dimmer pack has the following input options, 128 channel Micro-Plex (3-pin XLR male and female), 0–10V analog input (5-pin DIN) and a DMX512 digital control (5-pin XLR male and female). For the Lock-In experiments, the 0–10V analog input was used since it was easy to interface with the output of the function generator.

Figure 1.13: Leviton^{TM} DDS6000 dimming system

Support System: A Manfrotto^{TM} 055XPROB tripod system was used with a 498RC2 ball-head to support the infrared camera. The setup is shown in Figure 1.14. The support system consists of three legs and is made primarily of Aluminum. It offers solid support to the infrared camera by isolating vibrations. The tripod has a center column that can be quickly and easily swung from vertical to horizontal without any disassembly, permitting use in tight areas. The horizontal column

feature also allows the tripod to reach extremely low positions. The tripod has ergonomic flip-locks, with only 45 of movement. The flip-locks allow for extension of the individual legs. Four leg-angle settings are possible, the minimum leg angle is 25°. The other possible leg angles are 46°, 66° and 88°. The tripod has a bubble level that is included to help level the system. The maximum height of the tripod is 70.3" and the weight of the tripod legs is 5.4 pounds.

The Manfrotto 498RC2 ball-head with quick release plate is constructed of die-cast aluminum. It is rated strong enough to securely support a weight of 18 pounds. It has a repositionable locking lever for 360° panoramic rotation and offers 90° tilt movements, plus a friction control for precise positioning. Infrared camera was attached to the ball head through the mounting plate with 1/4" male threads. The head to tripod attachment has 3/8" female threads. Additionally, the Quick Release has a safety system to prevent an accidental detaching from the head. The height of the ball-head is 4.92" and the weight is 1.34 pounds.

Figure 1.14: The Manfrotto^{TM} tripod system

Computation System and Software: A Lenovo^{TM} T61P laptop was used for the data acquisition and processing. The laptop interfaced with the infrared camera via a CAT6 ethernet cable that attaches to the gigabit ethernet port on the laptop. The laptop had a Intel^{TM} Core i7 Q720 CPU with 4GB of DDR2 RAM along with a 256MB nvidia Quadro FX 570M graphics card. The computer had the FLIR^{TM} ExaminIR software installed. ExaminIR is a thermal measurement, recording, and analysis software for FLIR^{TM} cameras. The ExaminIR software connects directly to the cameras via gigabit ethernet to acquire thermal snapshots or movie files. ExaminIR supports multiple acquisition options, including high-speed burst mode recording to RAM or slower speed data logging to a hard drive. The user can customize recording options. ExaminIR can perform real-time image analysis, with an extensive set of ROI measurement tools including spots, lines, and areas. ExaminIR supports Preset Sequencing and superframing for analysis of scenes with large temperature differences or targets with rapid thermal dynamics. ExaminIR also provides an array of charting and plotting capabilities including line profiles, histograms, and temporal plots. The image and plot data from ExaminIR can be exported graphically as a bitmap or as a .CSV file for reporting and analysis in other software programs like MATLAB^{TM} and Mathematica^{TM}, where further analysis can be performed.

1.5 Summary of Original Contributions

The thesis aims at enhancing the performance of Infrared Thermography NDT through improving contrast for defect detection and improving defect size and depth estimation.

Two types of defect detection methods based on Pulsed Thermography and Lock-In Thermography are presented in this thesis. The first method is based on Pulsed Thermography. A novel two stage signal processing method to detect delaminations and skin-core disbonds in composite plates was presented. The method addressed some of the shortcomings of the classical Infrared Thermography methods. No reference area specification and no user intervention is required.

Since each pixel is treated independently, the effects of non-uniform heating are minimized. In addition, an approach combining Lock-In Thermography, image processing and statistical analysis to detect defects in a wind turbine blade was presented. The approach countered "blind frequency" effects since Lock-In tests were performed at multiple frequencies and the defect detection performance was improved as the Multivariate Outlier Analysis combined in a statistically robust manner the detection performance of the individual Lock-In detectors.

The concept of Virtual Heat Sources in Infrared Thermography was introduced in Infrared Thermography and an analytical model was developed to simulate its effect. Since 1D heat conduction based methods, that are commonly used in literature, were inadequate in modeling the heat flow around defects, a novel 3D heat conduction based defect quantification method to accurately predict the defect depth and size was developed. In particular, a method to model 2D axisymmetric heat diffusion around circular defects in isotropic materials like stainless steel was presented. Further, the model was extended to account for 3D heat conduction around rectangular defects in quasi-isotropic composite materials.

1.6 Outline of the Dissertation

The reminder of the thesis is organized as follows. In chapter 2, the use of Pulsed Thermography to identify defects using a novel two-stage signal reconstruction approach is proposed. The first stage involves low-pass filtering using Wavelets. In the second stage, a Multivariate Outlier Analysis is performed on filtered data using a set of signal features. The results are presented for the case of a composite plate with simulated delaminations, and a composite sandwich plate with skin-core disbonds.

In chapter 3, a NDT technique based on Lock-In thermography is proposed to detect defects present in a composite wind turbine blade. A set of image processing algorithms and Multivariate Outlier Analysis were used in conjunction with the classical Lock-In thermography technique to counter the "blind frequency" effects and to improve the defect contrast. Receiver Operating Characteristic curves

were used to quantify the gains obtained by using Multivariate Outlier Analysis. Experimental results were presented on a set of sixteen defects of various sizes that were incorporated during the construction of the wind turbine blade.

In chapter 4, the problem of determining defect depth and size using Pulsed Thermography is presented. Since, 1D heat conduction based models are generally inadequate in predicting heat flow around defects, a novel approach based on virtual heat sources was proposed to model heat flow around defects accounting for 2D axisymmetric heat conduction. The proposed approach was used to quantitatively determine the defect depth and size. The validity of the model was established using experiments performed on a stainless steel plate specimen with flat bottom holes at different depths.

In chapter 5, the problem of defect depth and size estimation using Pulsed Thermography is extended to quasi-isotropic composite structures. The proposed approach uses the excess temperature profile that is obtained over a defective area with respect to a sound area to estimate the defect dimensions and depth. The modeling process involved coordinate transformations and partial differential equation techniques. The validity of the model and approach is established using experiments performed on a composite panel containing rectangular flat-bottom holes of different sizes, present at different depths.

Finally, in chapter 6, the conclusions and suggestions for future work are presented.

Chapter 2

Defect Detection using Pulsed Thermography

2.1 Abstract

Composites are becoming an integral part of high performance structures. Low weight, high strength and corrosion resistance are some of the main reasons they are favored compared to metals. One of the main beneficiaries of the composite technology is the aerospace industry. Many structural components like fuselage and wings are being made out of composites. Nondestructive detection of defects in composites is important in order to avoid catastrophic events [35, 36, 46, 61–66]. In this chapter, a novel two-stage signal reconstruction approach is proposed to filter and reconstruct raw thermal image sequences to detect defects. The first stage involves low-pass filtering using Wavelets. In the second stage, a Multivariate Outlier Analysis is performed on filtered data using a set of signal features. The proposed approach significantly enhances the defective area contrast against the background. The two-stage approach has some advantages in comparison to the traditionally used methods, including automation in the defect detection process and better defective area isolation through increased contrast. The method does not require a reference area to function. A detailed description of the approach is presented in the subsequent sections. The results will be presented for the case of a composite plate with simulated delaminations, and a composite sandwich plate with skin-core disbonds.

2.2 Experimental Setup and Data Collection

A speedotron^{TM} 4800W power pack was used to trigger two strobes which output 2400W each. In order to have a fairly uniform heating profile on the surface, the two strobes are placed symmetrically as shown in Figure 2.1. The strobes cause approximately, $10°C$ rise in temperature at each point in the frontal surface of the test object.

Experiments were performed on a composite plate with simulated delaminations and a sandwich plate with skin-core disbonds. A brief description of the test specimens is presented here.

Defected composite plate: A composite plate measuring 12" × 12" was fabricated at the UCSD composites laboratory. It was made using T300/5208 fiber and epoxy combination. It consists of 8 layers in the orientation $[0/-45/+45/0]_s$. The thickness of each layer is 0.125mm. At known depths, thin teflon inserts measuring 1" × 1" were inserted to create delaminations. The delaminations were inserted at depths of $0.25mm$, $0.50mm$ and $0.75mm$ from the top surface. Henceforth, the three delaminations will be referred to as top, middle and bottom delaminations respectively. The top delamination is the rightmost, while the bottom delamination is the leftmost in Figure 2.2.

Defected sandwich plate: A sandwich plate containing a honeycomb core and a Carbon Fiber Reinforced Plastic (CFRP) skin was also fabricated. The CFRP skin was made of the same material combination as the previous plate. Again, three thin teflon inserts were inserted between the skin and the core to simulate the skin-core disbonds. The dimensions of the disbonds are 0.5" × 0.5", 1" × 1" and 1" × 1". A schematic of the sandwich plate is shown in Figure 2.3. The cross-section view of the plate is shown in Figure 2.4.

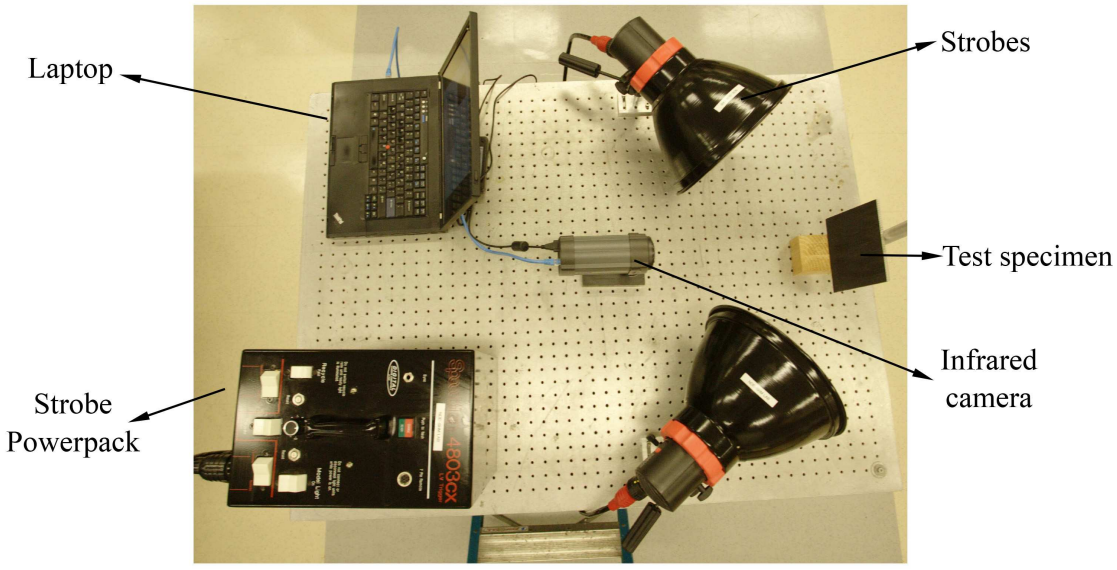

Figure 2.1: Experimental setup

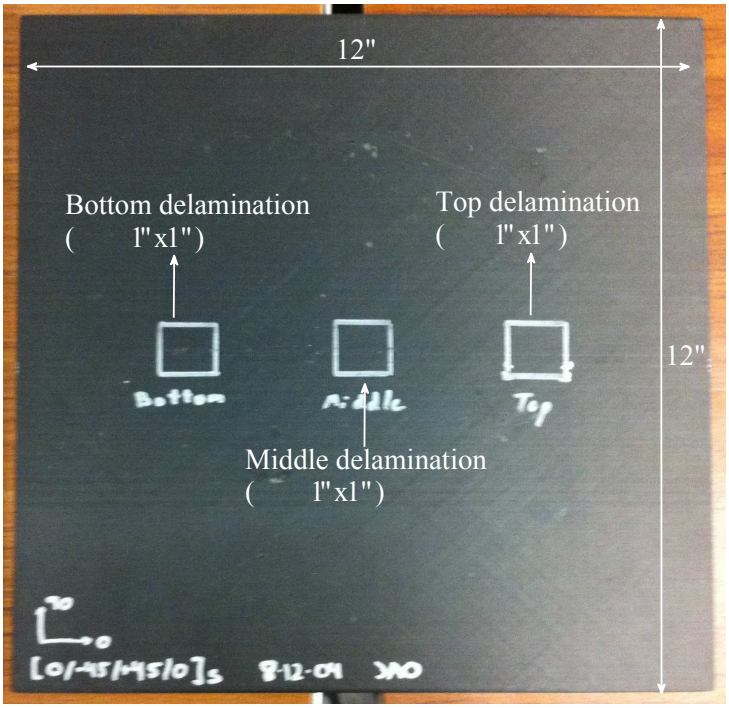

Figure 2.2: Schematic of composite plate with delaminations

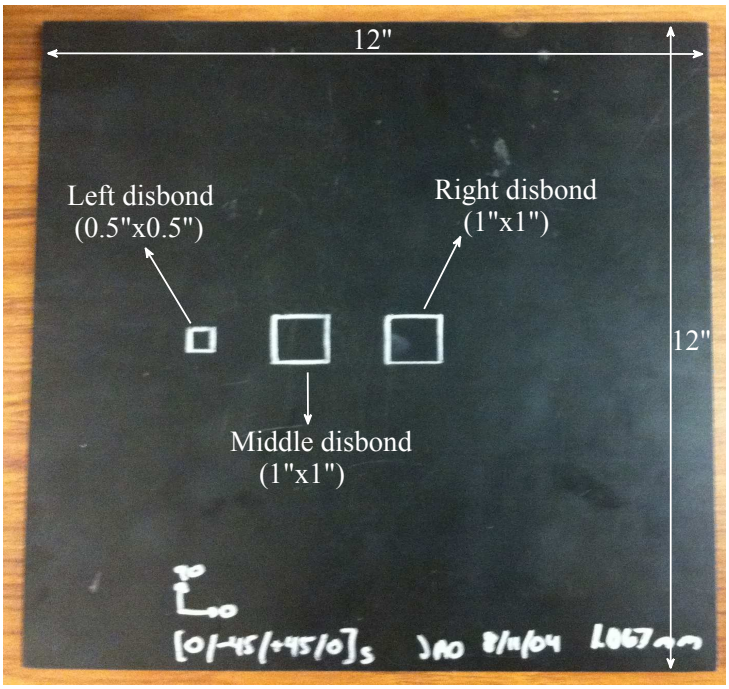

Figure 2.3: Schematic of sandwich plate with skin-core disbonds

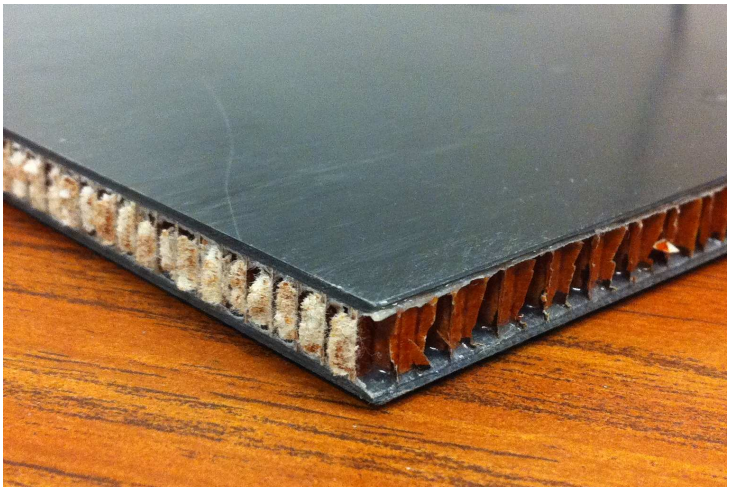

Figure 2.4: Sandwich plate cross-section showing the honeycomb core attached the CFRP skin

2.3 Signal Processing and Results

In this section, the two-stage signal processing algorithm is described. In the first stage, the raw thermal data is filtered using the Wavelet Transform. The filtered data is then subjected to a Multivariate Outlier Analysis using a set of signal features to boost the defective area contrast in the thermal images.

2.3.1 Wavelet Filtering

The basis functions of the Wavelet Transform [50, 67–69] are small waves, called Wavelets which have varying frequency and limited duration [70]. The Wavelet Transform provides both temporal and frequency information. Wavelets provide tremendous flexibility in data analysis and also form the basis of Multiresolution Theory [67, 69]. As the name implies, Multiresolution Theory [67] is used to represent the raw signal at more than one resolution.

In the raw thermal sequences, the low-frequency content is the most important part for damage detection. In Wavelet analysis, the low and high frequency content is often referred to as Approximations and Details. The Approximations are the high-scale, low-frequency components of the signal. The Details are the

low-scale, high-frequency components. As the decomposition level is increased, the Wavelet Transform zooms into the lower frequencies as shown in Figure 2.5. At each level of decomposition, the number of data points is halved. In this study, the thermal signals are decomposed into five levels using the Coiflets Wavelet.

Figure 2.6 shows the cooling curve recorded at a point of the composite plate with delaminations following the flash input. The composite plate is shown in Figure 2.2. It is clear that the temperature falls rapidly from $40.5°C$ to $33.5°C$ within the first $0.5s$. During this stage, a much lower level of decomposition is sufficient to filter the signal as the noise levels are not significant compared to the magnitude of the raw signal. A level 3 of decomposition is used. After $0.5s$, the noise content is significant and hence a more aggressive filter is required to produce clean signal. A level 5 of Wavelet decomposition is used in this time window. When automating, the transition point could be identified by tracking the slope of the temperature variation. To show details clearly, Figure 2.7 presents the wavelet filtering performance in the time window, 1-2s.

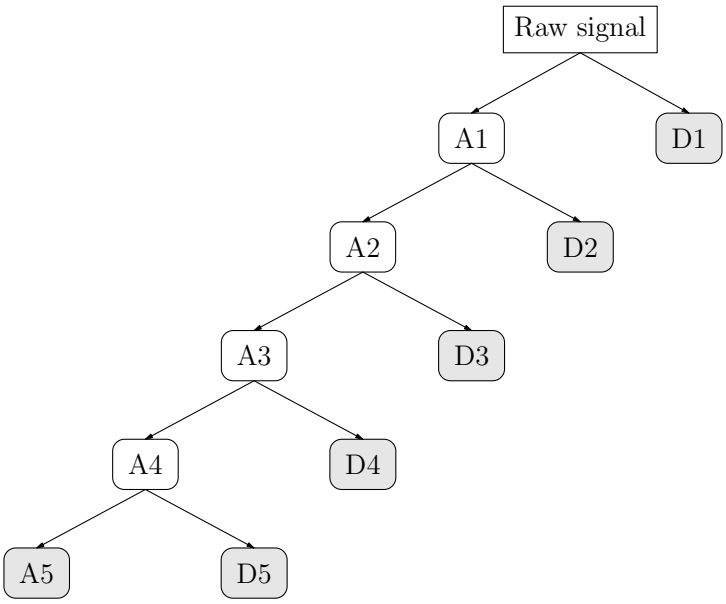

Figure 2.5: Wavelet decomposition

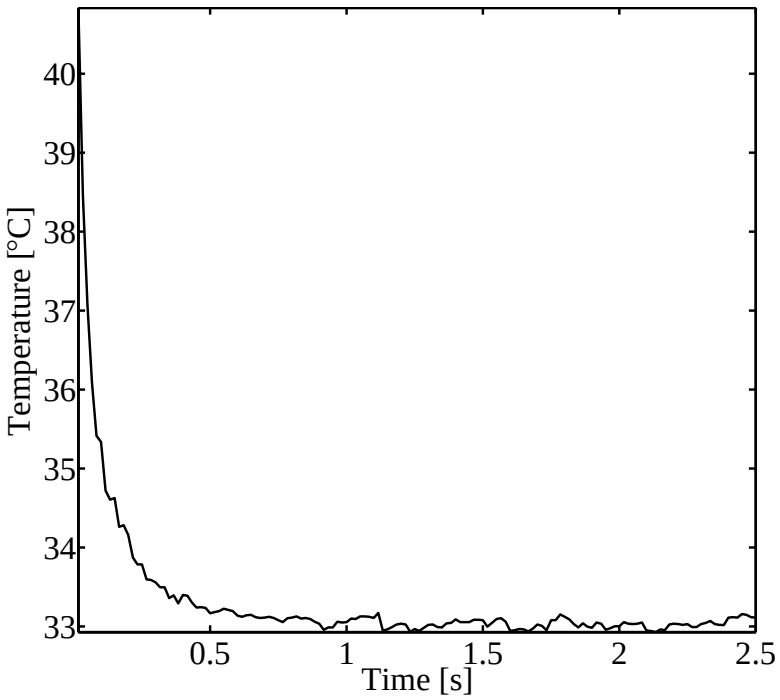

Figure 2.6: Cooling profile at a sample point on the composite plate with delaminations

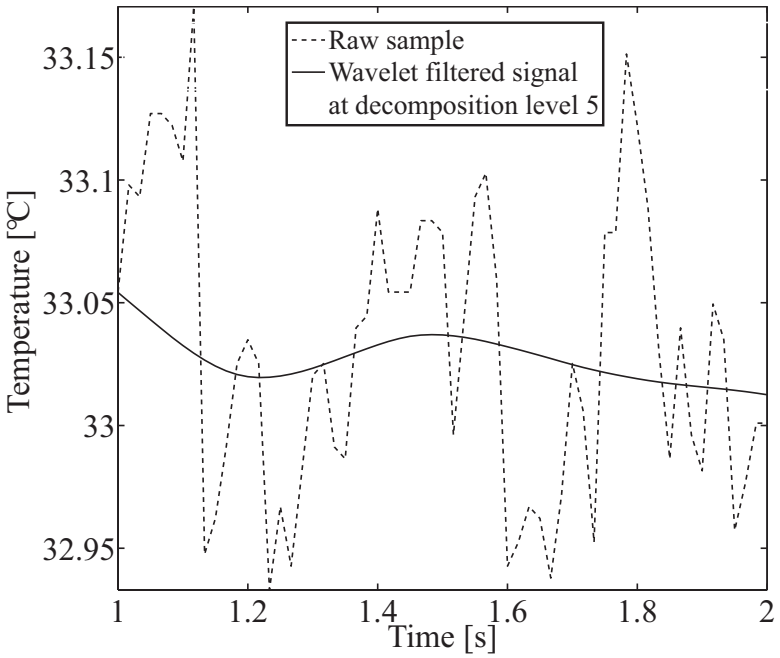

Figure 2.7: Denoising performance comparison of Wavelet filtering - (1-2s)

It is to be noted from Figure 2.7 that the Wavelet filtering approach retains the key signal fluctuations while efficiently filtering the high frequency temporal noise. The Wavelet filtered signal was calculated at the different points of the composite plate and sandwich plate yielding a filtered sequence of frames which was available for further processing.

2.3.2 Multivariate Outlier Analysis

The subsequent analysis is based on Outlier Statistical Processing [68, 71]. An outlier is a datum that appears statistically inconsistent with a set of data, the baseline. The baseline describes the normal condition of the structure under investigation. In the analysis of one-dimensional elements, the detection of outliers is a straightforward process based on the determination of the discordancy between the one-dimensional datum and the baseline. One of the most common discordancy tests is based on the deviation statistics, Z_ζ, defined as

$$Z_\zeta = \frac{x_\zeta - \overline{x}}{\sigma} \tag{2.1}$$

where Z_ζ is the potential outlier, $\overline{x}$ and σ are the mean and the standard deviation of the baseline, respectively. A set of p-dimensional (multivariate) data consists of n observations in p variables. The discordancy test in the multivariate case is expressed by the Mahalanobis Squared Distance, D_ζ, which is a non-negative scalar defined as

$$D_\zeta = (x_\zeta - \overline{x})^T [K]^{-1} (x_\zeta - \overline{x}) \tag{2.2}$$

where x_ζ is the potential outlier vector, $\overline{x}$ is the mean vector of the baseline, $[K]$ is the covariance matrix of the baseline and T represents a transposed matrix. Multivariate Outlier Analysis for the composite plate with delaminations and for the sandwich plate with skin-core disbonds was performed using the following set of features extracted from the Wavelet filtered thermal images.

- Area under the cooling curve
- Root Mean Square of the rate of cooling
- Kurtosis of the rate of cooling

- Goodness of fit of the cooling curve compared to theoretical 1D heat conduction model
- Correlation between the observed cooling curve and the theoretical 1D heat conduction model

Figure 2.8 and Figure 2.9 compare the raw thermal images and the two-stage signal processed data for the composite plate and the sandwich plate respectively. Figure 2.10 and Figure 2.13 show the raw thermal data intensity for the composite plate and the sandwich plate respectively, obtained at 0.5s after flash input. Figure 2.11 and Figure 2.14 show the result of the wavelet filtering on the raw thermal data for the composite plate and the sandwich plate respectively, obtained at 0.5s after flash input. 3D surface representations of the result of the two-stage signal processing are shown in Figure 2.12 and Figure 2.15. From these figures it can be seen that the two-stage signal processing approach brings out the contrast of the defective areas(delaminations and skin-core disbonds) clearly against the background in both the cases.

To better compare the performance of the algorithm, the profile plots of the normalized intensity values are plotted across lines Y1, X1, X2, X3 as shown in Figure 2.8 and Figure 2.9. The results are shown in Figure 2.16 and Figure 2.17 along Y1 for the composite plate and the sandwich plate respectively. The profiles along X1-X2-X3 directions are shown in Figure 2.18 and Figure 2.19. A significant improvement in the signal intensity across the defective areas against the sound area is observed as a result of the two-stage signal processing. Based on results presented, all defects present in the two test specimens are clearly detected following the two-stage signal processing approach.

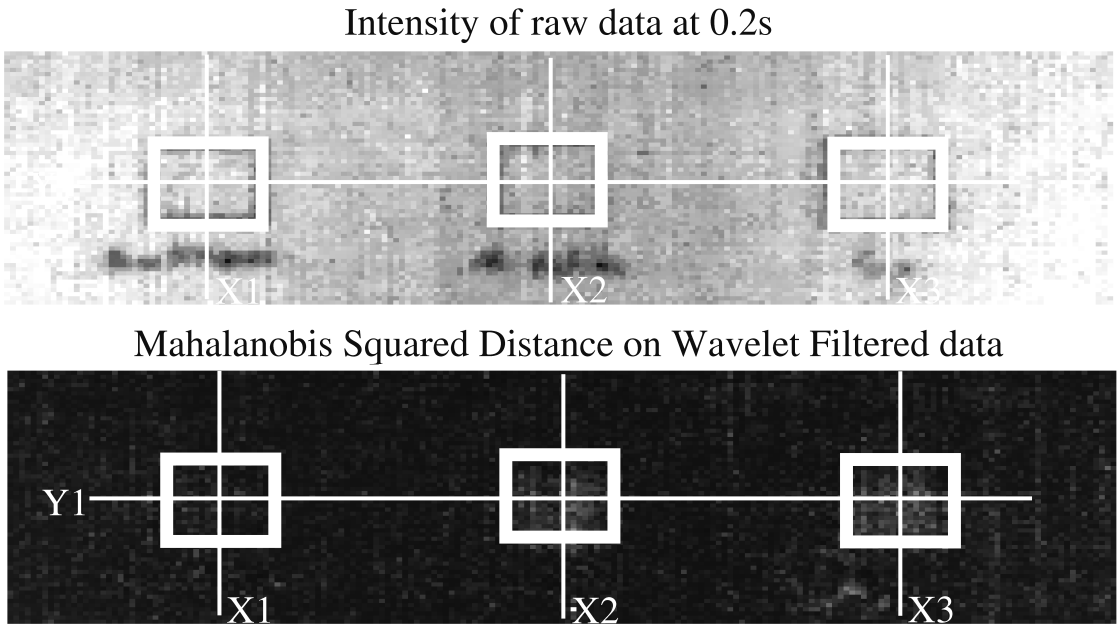

Figure 2.8: Results obtained on composite plate with delaminations

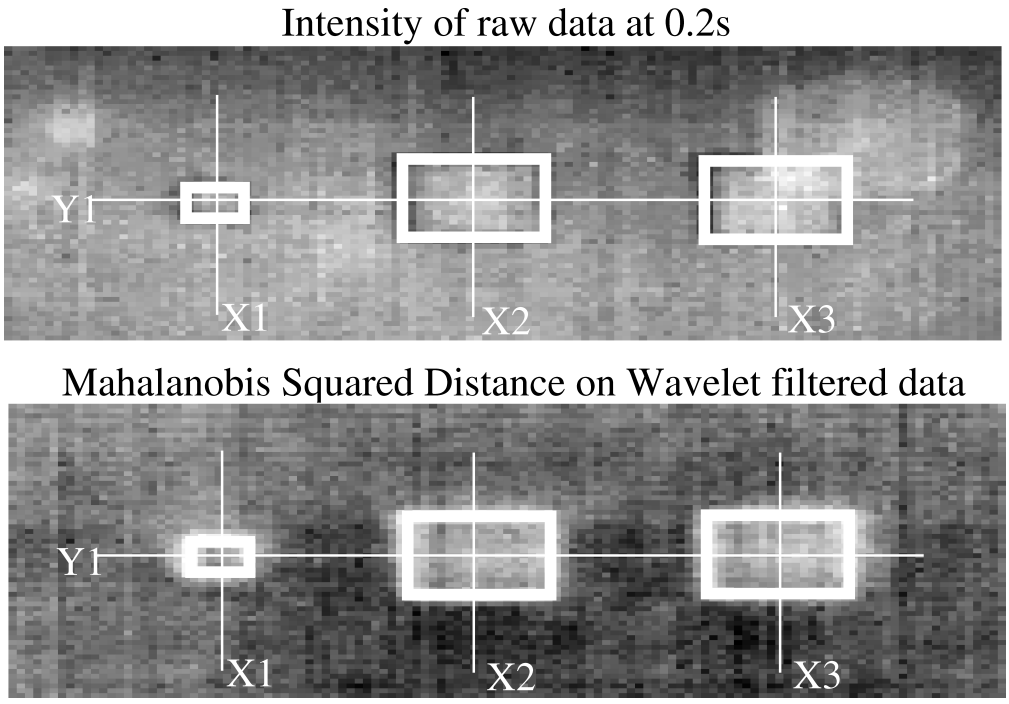

Figure 2.9: Results obtained on sandwich plate with skin-core disbonds

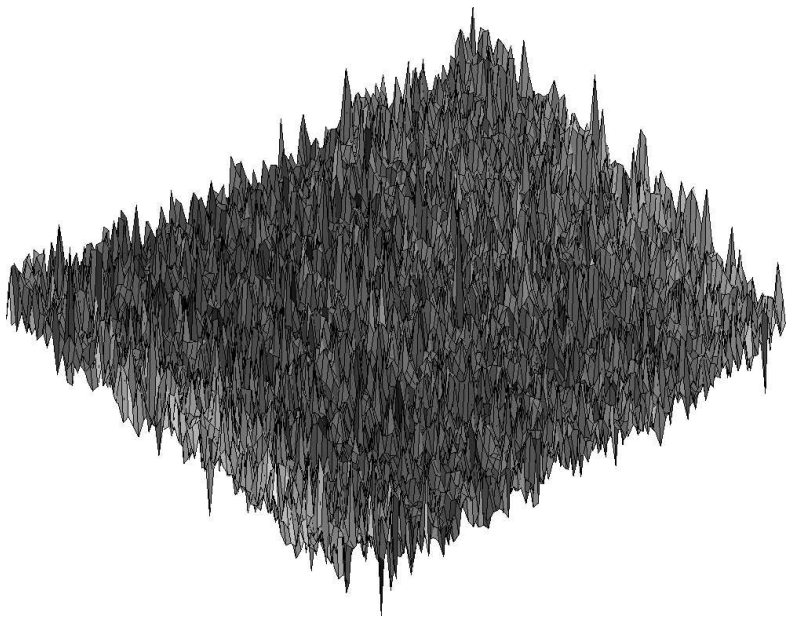

Figure 2.10: 3D surface view of raw thermal data intensity obtained on composite plate with delaminations, 0.5s after flash input

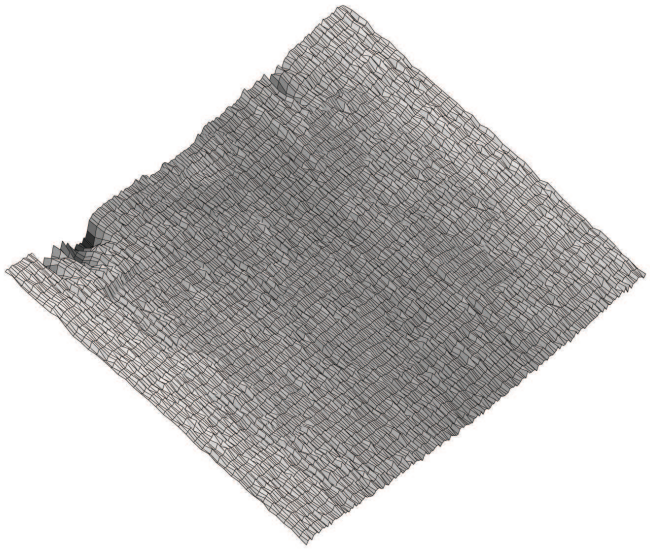

Figure 2.11: 3D surface view of the wavelet filtered data obtained on composite plate with delaminations, 0.5s after flash input

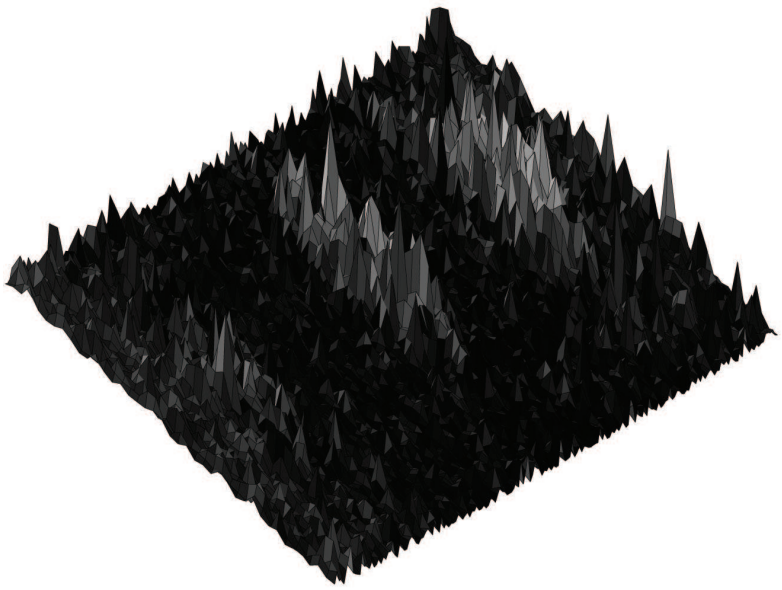

Figure 2.12: 3D surface view of Mahalanobis Squared Distance obtained on composite plate with delaminations

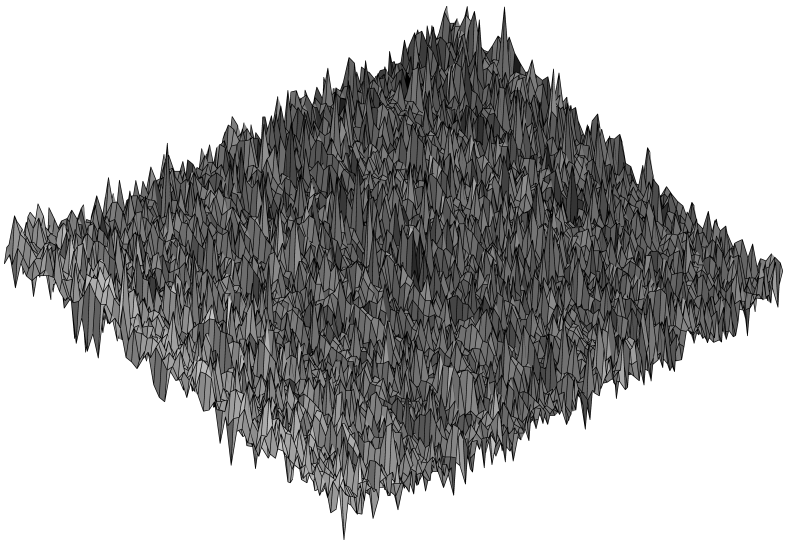

Figure 2.13: 3D surface view of raw thermal data intensity obtained on sandwich plate with skin-core disbonds, 0.5s after flash input

Figure 2.14: 3D surface view of the wavelet filtered data obtained on sandwich plate with disbonds, 0.5s after flash input

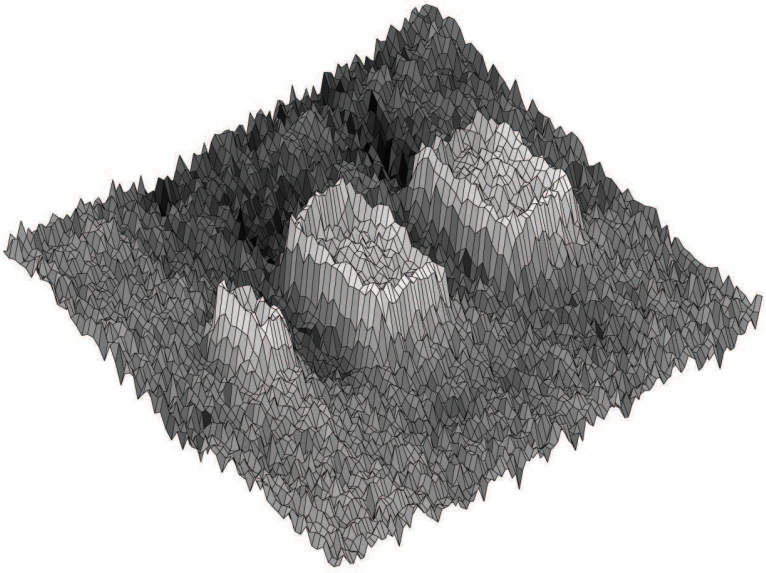

Figure 2.15: 3D surface view of Mahalanobis Squared Distance obtained on sandwich plate with skin-core disbonds

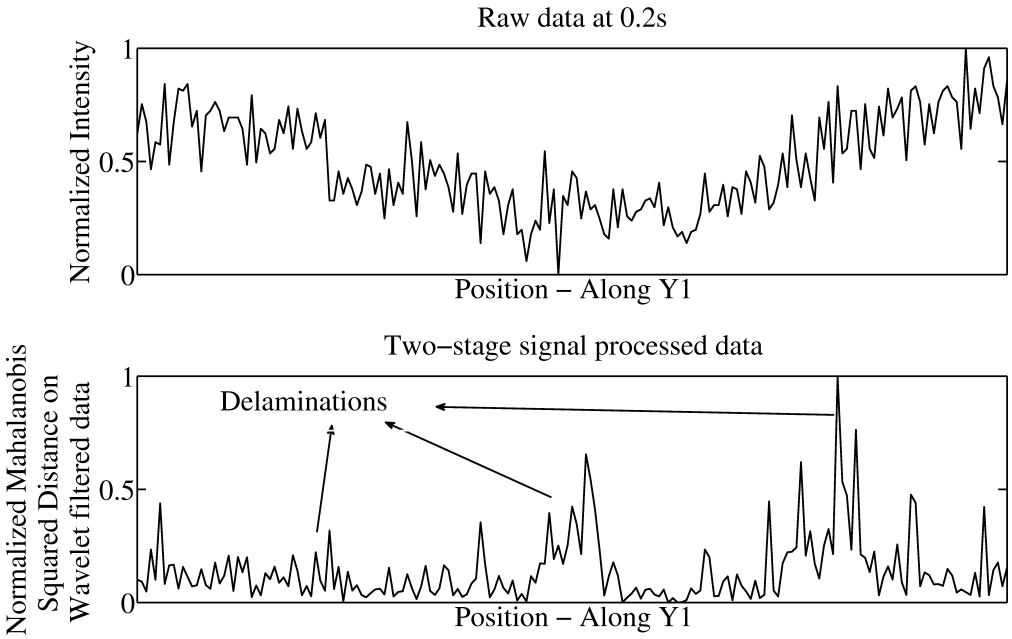

Figure 2.16: Profile plots comparing signals along Y1 for composite plate with delaminations

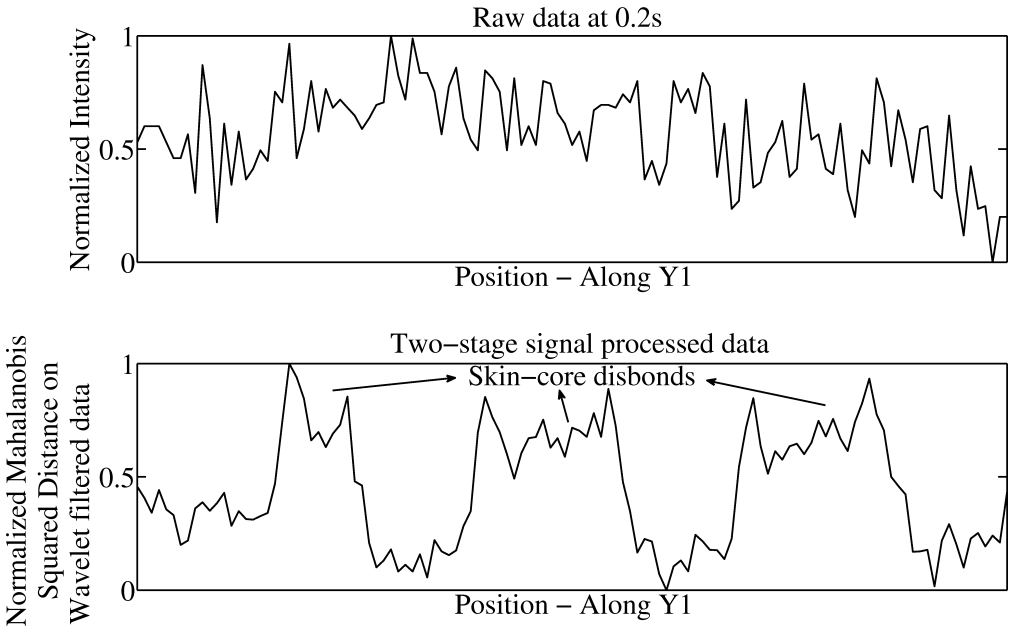

Figure 2.17: Profile plots comparing signals along Y1 for sandwich plate with skin-core disbonds

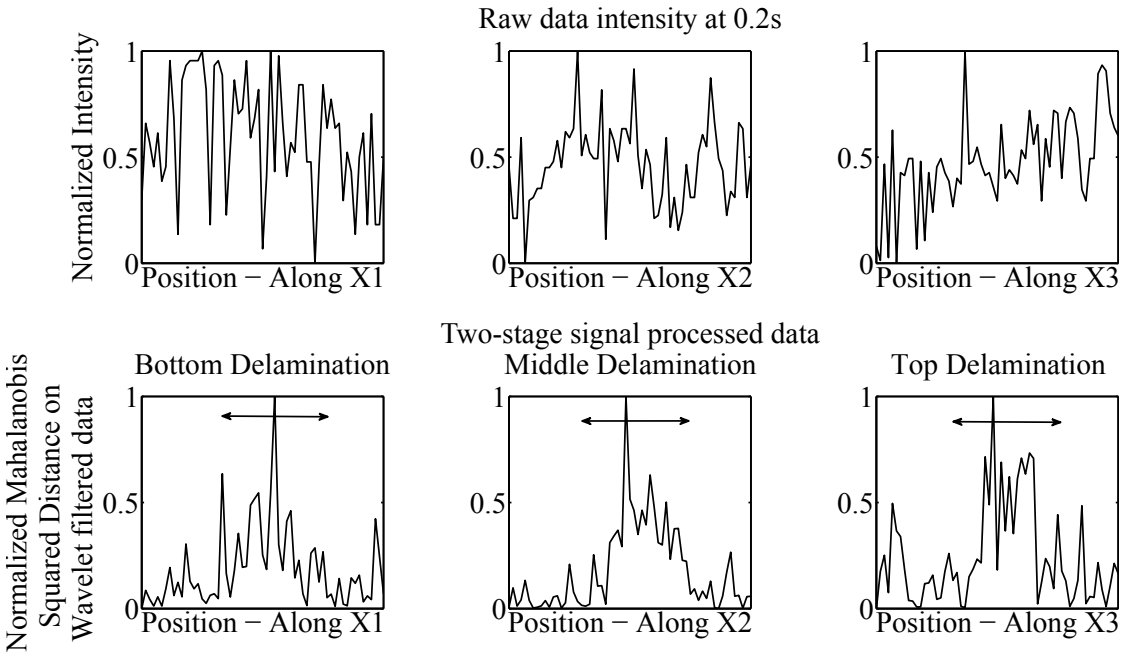

Figure 2.18: Profile plots comparing signals along X1, X2 and X3 for composite plate with delaminations

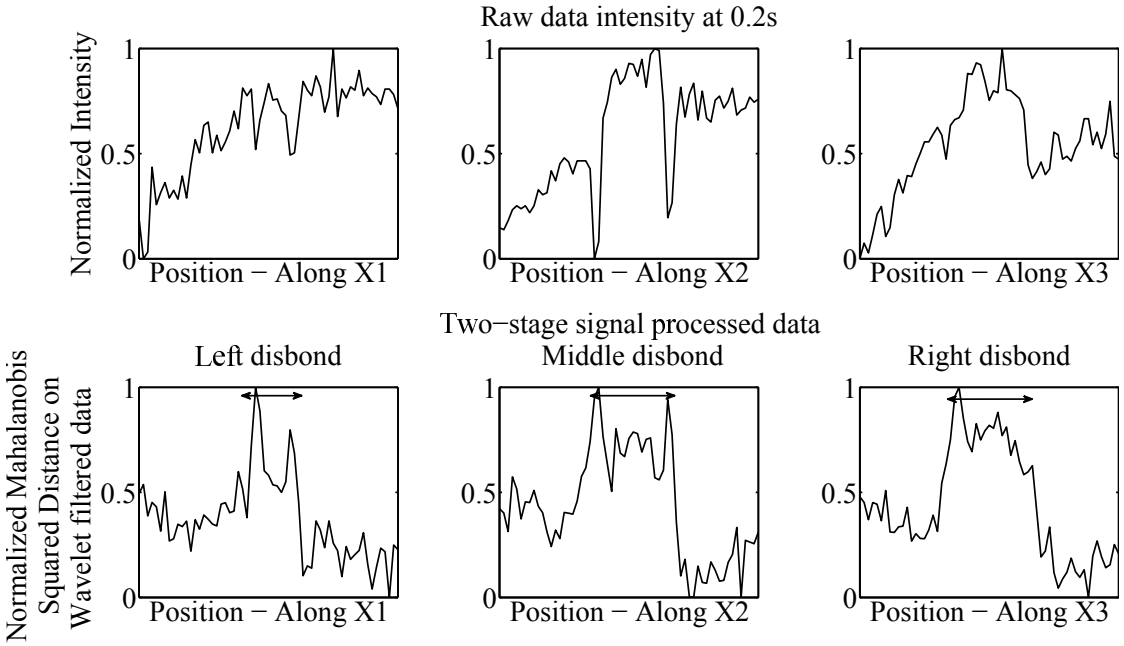

Figure 2.19: Profile plots comparing signals along X1, X2 and X3 for sandwich plate with skin-core disbonds

To further quantify the usefulness of the two-stage signal processing approach, the Signal-to-Noise Ratio (SNR) was computed along linear distances across the defects as,

$$\text{SNR} = \frac{\Sigma I_d}{\Sigma I_s} \tag{2.3}$$

Where ΣI_d is the sum of the normalized Mahalanobis Squared Distance values across a defect and ΣI_s is the sum of the normalized Mahalanobis Squared Distance values across the same length on either side of a defect. The SNR obtained across the three delaminations in the composite plate with delaminations is presented in Table 2.1. The same metrics in the Sandwich plate is shown in Table 2.2. The two-stage signal processing clearly produces a notable SNR improvement for all defects in both the test specimens.

Table 2.1: SNR comparison across the bottom, middle and top delaminations in the composite plate

Position		Top	Middle	Bottom
Y1	Raw data	1.00	0.99	1.01
	Two-stage signal processing	4.53	5.76	2.31
X1	Raw data	X	X	1.01
	Two-stage signal processing	X	X	3.12
X2	Raw data	X	1.02	X
	Two-stage signal processing	X	7.04	X
X3	Raw data	0.99	X	X
	Two-stage signal processing	4.29	X	X

Table 2.2: SNR comparison across the left, middle and right skin-core disbonds in the sandwich plate

Position		Left	Middle	Right
Y1	Raw data	1.01	0.99	1.71
	Two-stage signal processing	1.71	2.39	5.79
X1	Raw data	0.99	X	X
	Two-stage signal processing	1.45	X	X
X2	Raw data	X	1.00	X
	Two-stage signal processing	X	3.19	X
X3	Raw data	X	X	1.60
	Two-stage signal processing	X	X	4.44

For the above results, an inclusive baseline was used in the second stage to compute the Mahalanobis Squared Distance. An inclusive baseline consists of the sound and the defective areas. This is feasible since there is no user intervention that is needed in specifying the sound area and the approach is particularly useful in blind tests when the sample does not have too many defects. However, in some cases, the sound area could be specified and this helps in further improving the contrast since the baseline comprises of the sound area without any defects. Figures 2.20–2.23 compare the effect of inclusive and exclusive baselines on the two-stage processing on the composite plate with delaminations and the sandwich plate with disbonds.

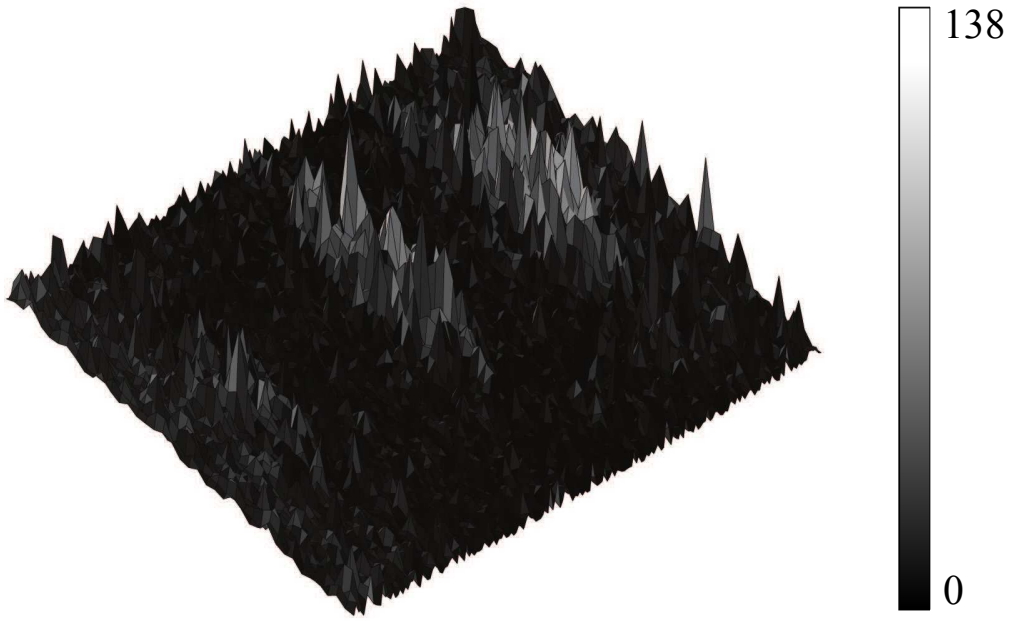

Figure 2.20: 3D surface view of Mahalanobis Squared Distance obtained on composite plate with delaminations with an inclusive baseline

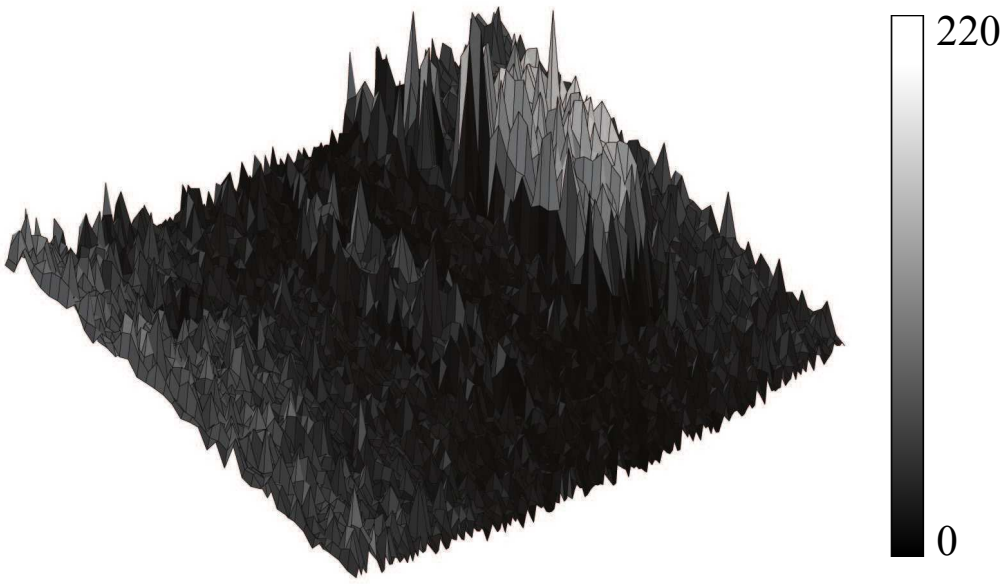

Figure 2.21: 3D surface view of Mahalanobis Squared Distance obtained on composite plate with delaminations with an exclusive baseline

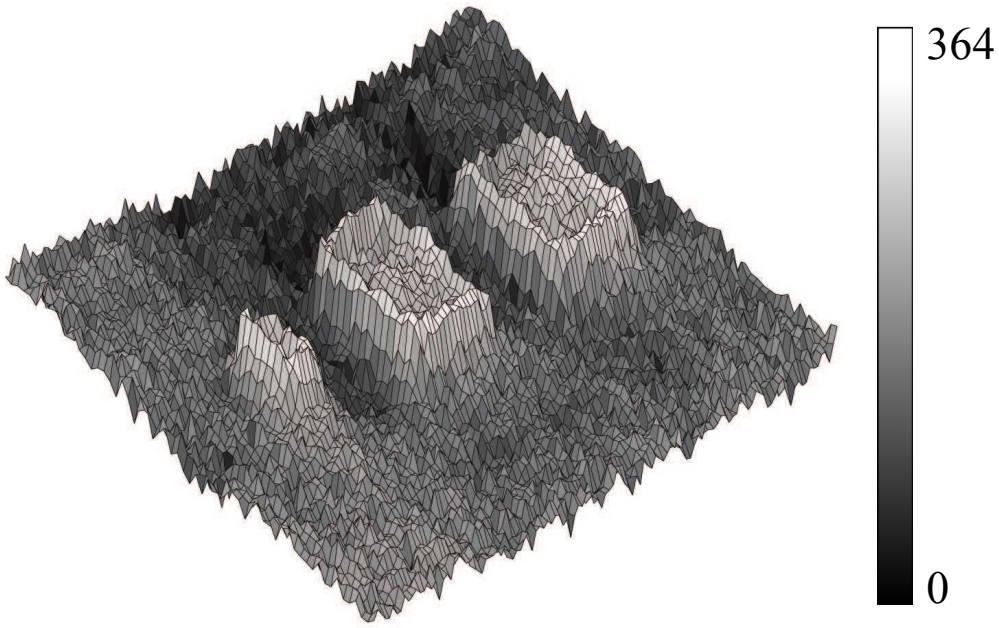

Figure 2.22: 3D surface view of Mahalanobis Squared Distance obtained on sandwich plate with disbonds with an inclusive baseline

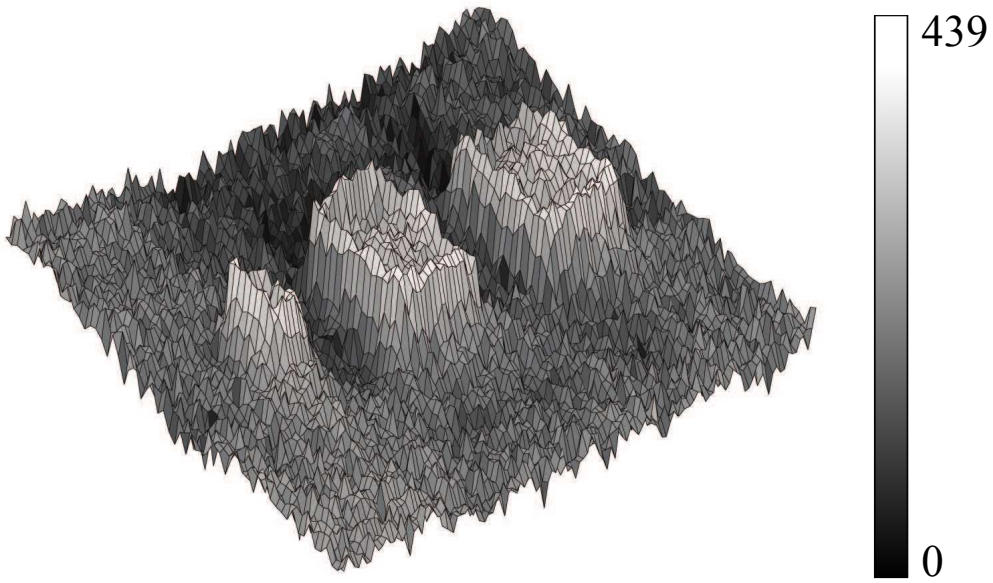

Figure 2.23: 3D surface view of Mahalanobis Squared Distance obtained on sandwich plate with disbonds with an exclusive baseline

2.4 Conclusions

A Wavelet-aided Multivariate Outlier Analysis was proposed for enhancing the contrast of thermographic NDE images. The method is able to function without a reference frame and could be automated. In the first stage, the raw thermal curve at each pixel is filtered using Wavelet processing. In the second stage, Multivariate Outlier Analysis is performed on the Wavelet filtered data using a specific set of signal features. Five features, based on the cooling curve($T(t)$ vs. t) and on the rate of cooling curve($\frac{\partial T}{\partial t}$ vs. t), were chosen and used in the study. The two-stage approach substantially increased the contrast of the defective areas against the sound area. The method was tested successfully on a composite plate with delaminations and on a sandwich plate with skin-core disbonds.

2.5 Acknowledgements

This project was funded by National Science Foundation (Grant # 0729760, Dr. Shih-Chi Liu – Program Manager). This chapter, in part, has been published in Experimental Techniques journal, Manohar, Arun; Lanza di Scalea, Francesco; (2011). The title of the paper is *Wavelet aided Multivariate Outlier Analysis to enhance defect contrast in thermal images.* The dissertation author was the primary investigator and primary author of this paper.

Chapter 3

Defect Detection using Lock-In Thermography

3.1 Abstract

Delaminations are a common type of defect that occurs in composite structures like wind turbine blades. In this chapter, a Nondestructive Testing technique based on Lock-In thermography is proposed to detect skin-skin delaminations and skin-core delaminations present in a 9m CX-100 [72] wind turbine blade. A set of image processing algorithms and Multivariate Outlier Analysis were used in conjunction with the classical Lock-In thermography technique to counter the "blind frequency" effects and to improve the defect contrast. Receiver Operating Characteristic curves were used to quantify the gains obtained by using Multivariate Outlier Analysis. Experiments were performed on a set of sixteen defects of various sizes that were incorporated during the construction of the CX-100 wind turbine blade at different locations and depths.

3.2 Introduction

The U.S. Department of Energy has recently set a target of adding 300GW of wind power over the next 20 years [73]. During this period, a surge in production of wind turbine blades is expected. Defects in wind turbine blades could occur during manufacturing, transportation, installation or while in operation. The Nondestructive Testing (NDT) community is still in the process of developing inspection techniques and standards for composite wind turbine blades [11, 74–88]. The problem of defect detection using infrared thermography has been studied extensively in the literature [21, 32, 45, 47, 48]. The most common implementation is based on Pulsed Thermography which is very well suited for detection of shallow defects. For deeper defects, Lock-In Thermography is generally preferred [26].

Lock-In Thermography [41, 51, 52] is based on the application of a periodic thermal energy input at very low frequency over a test object's surface. One of the main drawbacks of Lock-In Thermography is that "blind frequencies" affect defect detection [51]. To address this shortcoming, the current study proposes performing Lock-In tests at multiple frequencies, and subsequently applying Multivariate Outlier Analysis (MOA) to improve defect contrast and to counter the "blind fre-

quency" effects. Experiments were performed on a set of sixteen defects present in a test wind turbine blade at UCSD's Powell structural laboratories. The known defects created during the fabrication of the test blade were of different sizes and created at different positions and depths within the blade. The effectiveness of the proposed statistically-aided Lock-In Infrared Thermography is demonstrated quantitatively by computing the Receiver Operating Characteristic of the defect detection technique.

3.3 The CX-100 Wind Turbine Blade

Experiments were performed on defects present in a 9m wind turbine blade. The 9m test blade was built using the CX-100 design developed by TPI Composites and Sandia National Laboratory [72]. The blade is cantilevered at the UCSD Powell labs as shown in Figure 3.1. The blade contains materials and construction techniques similar to those used for todays typical turbine blade with lengths in the 40 meter range [81]. Several defects were added to the low-pressure side of the blade during the manufacturing stage. The types of embedded defects include skin-skin delaminations, skin-core delaminations, out-of-plane waviness, in-plane fiber waviness, shear web-to-skin disbonds and trailing edge adhesive disbonds [81]. In all, forty-five individual defects were embedded in the blade during the manufacturing process by using methods developed by both TPI Composites and Sandia National Laboratory for simulating actual defect characteristics.

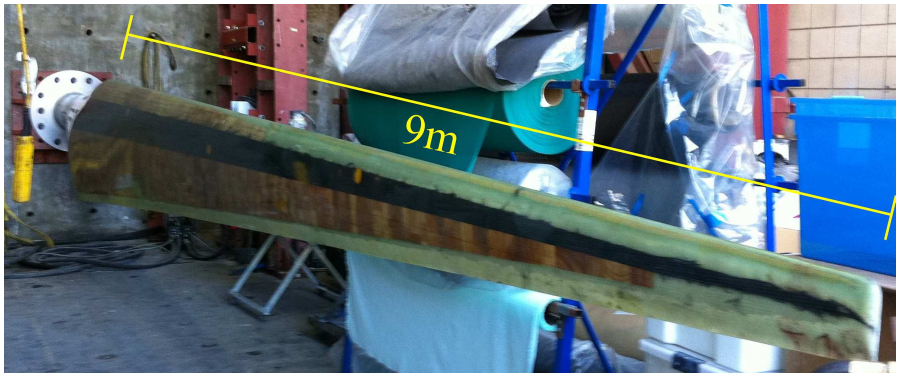

Figure 3.1: The CX-100 blade cantilevered at the UCSD Powell Labs

In this study, skin-skin delaminations and skin-core delaminations were considered. The skin-skin delamination defects are delaminations within the plies of the laminate, while the skin-core delamination defects are delaminations between the fiber glass skin and the core. The implementation of these defects in the structure was accomplished by placing specially designed pillow inserts between the layers during the layup process. The inserts were developed at the Sandia National Laboratory. The thickness of the inserts used in the blade was measured at 0.25 mm. The diameters of the inserts used were 12.7mm, 25.4mm and 50.8mm. The defects were mostly implemented at locations in sets of 3, one of each size, and separated by 15cm. In a few locations, only the two larger sizes were used. In all, sixteen skin-skin delaminations and skin-core delaminations were considered. The details of the defects considered are shown in Table 3.1 and the schematic is presented in Figure 3.2.

Table 3.1: Defects considered in the experiment

Defect Type	Defect Parameters				
	Index	x (cm)	y (cm)	Diameter (mm)	Depth (mm)
skin-skin delamination	1	135	12	50.8	0.7
	2	150	12	25.4	0.7
	3	165	12	12.7	0.7
	4	315	15	50.8	1.3
	5	330	15	25.4	1.3
	6	345	15	12.7	1.3
	7	520	4	50.8	1.3
	8	535	4	25.4	1.3
	9	685	7	25.4	1.3
	10	700	7	50.8	1.3
	11	715	7	25.4	1.3
skin-core delamination	12	485	-15	50.8	1.3
	13	500	-15	25.4	1.3
	14	515	-15	12.7	1.3
	15	595	-12	50.8	1.3
	16	610	-12	25.4	1.3

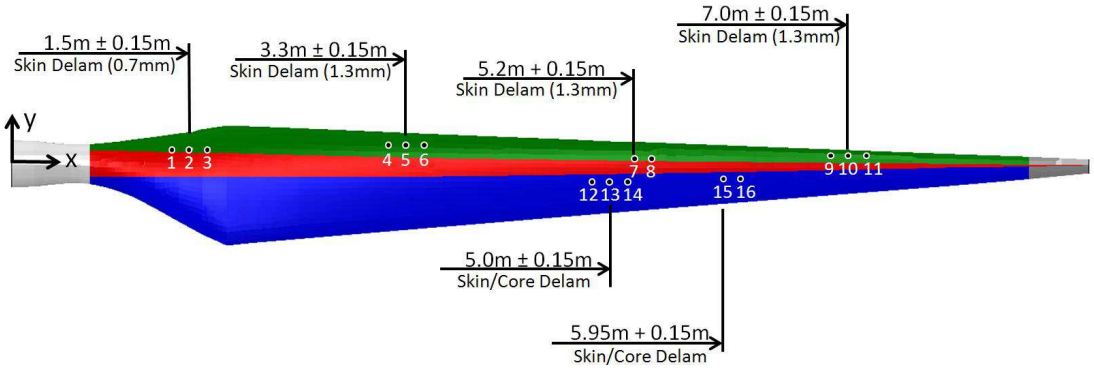

Figure 3.2: Schematic of the skin-skin delaminations and skin-core delaminations present in the CX-100 wind turbine blade

3.4 Defect Detection Approach

The unfinished surface of the wind turbine blade was very reflective and some of the sub-surface defects were visible to the naked eye. The areas to be inspected by Infrared Thermography were prepared by a thin coat of black, water-soluble paint to hide the defects. Moreover, the paint layer improved the heat absorption at the surface and minimized the reflection of other heat sources present in the vicinity of the test area. For optimal detection of defects using the Lock-In technique, it is well established that the depth of the defect must be less than the thermal diffusion length [41]. The thermal diffusion length, z, is related to the thermal conductivity of the material, k, density, ρ, Lock-In frequency, f, and specific heat conductivity, c, by,

$$z = \sqrt{\frac{k}{\pi f \rho c}} \tag{3.1}$$

However, at some frequencies, commonly referred to as "blind frequencies" in the Lock-In Thermography literature, the defects are undetected even though the thermal diffusion length is greater than the defect depth. Thus, the ability to detect defects within the object depends on the Lock-In frequency used. For a single-layer material, Equation 3.1 can be used to compute the thermal diffusion length. However, the test specimen that was used in the presented study is a wind turbine

blade which has layers of different materials whose properties and thickness are different. The calculation of the thermal diffusion length is not a straight-forward task. For the presented study, numerous experiments were performed at different Lock-In frequencies in order to determine the sensitive working range. Lock-In frequencies in the range of 30mHz–70mHz yielded the best results and were chosen for the experiments.

3.4.1 Lock-In Thermography

Lock-In Thermography is based on the application of a periodic thermal energy input to the surface of the object. When the resulting heat wave encounters a defect, some of it is reflected, causing a phase shift with respect to the input heat wave.

The Lock-In Thermography setup that was used in the present study is shown in Figure 3.3. The main components are the function generator, lighting dimmer pack, halogen lamps, IR camera and laptop. The function generator was used to generate the sinusoidal wave at a particular frequency and amplitude. The output of the function generator was fed into the lighting dimmer pack that amplified the power of the signal and delivered to the halogen lamps. The lamps heated the blade surface, that was imaged by the IR camera connected to the laptop for subsequent analysis.

The IR camera used was a FLIR^{TM} A320G camera with a maximum frame rate of 60Hz. The detector is a focal plane array uncooled microbolometer with a spectral range of 7.5–13 μm, a resolution of 240x320 pixels, and Thermal Sensitivity of 50mK.

For the Lock-In heating, five different frequencies ranging from 30mHz to 70mHz were used at each test location as shown in Table 3.2. A pair of halogen lamps that were rated at 1400W maximum total power was used to heat the test areas over three Lock-In time-periods. The temperature profile that was obtained at the surface can be compared to a sinusoid plus a constant temperature slope that is a consequence of the multiple heating cycles. A typical temperature profile at a sample location on the blade's surface is shown in Figure 3.4 when three heating

cycles were used at a Lock-In frequency of 50mHz. At every location, linear fitting is performed to determine the temperature slope and the slope is removed from the raw data. The resulting temperature-time distribution that is obtained after the temperature slope removal is shown in Figure 3.5.

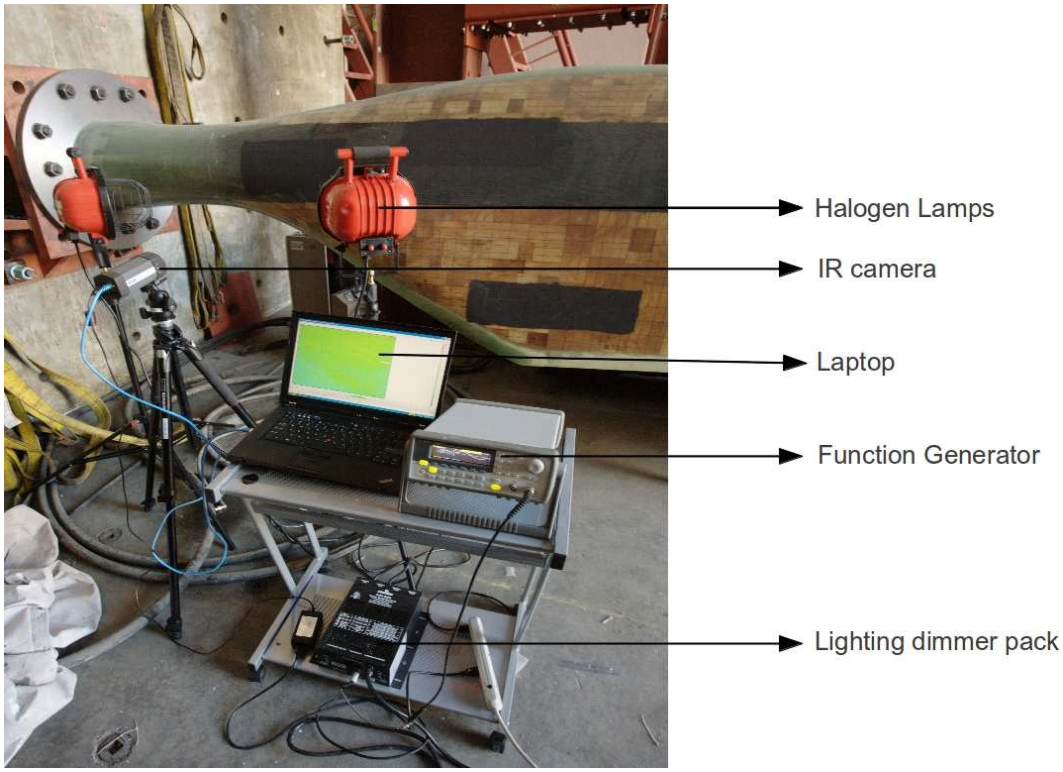

Figure 3.3: Experimental setup used in Lock-In Thermography test of the blade

Table 3.2: Details of Lock-In experiment

Lock-In Frequency [mHz]	Time Period [s]	Acquisition Time [s]
30	33.30	100
40	25.00	75
50	20.00	60
60	16.67	50
70	14.28	42.85

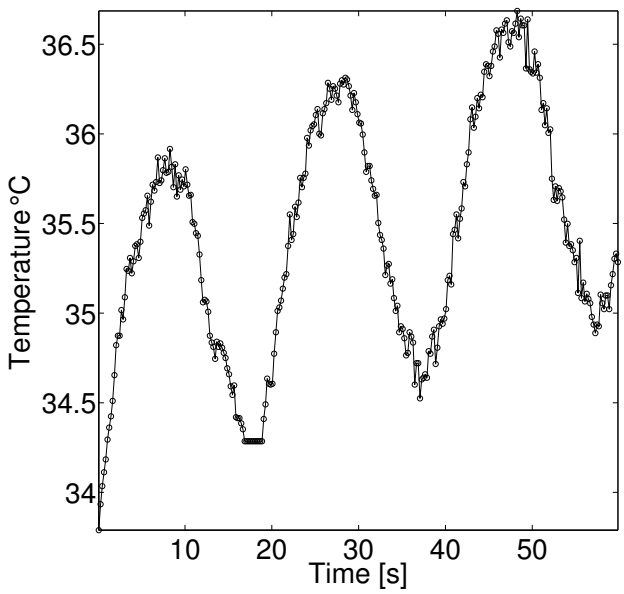

Figure 3.4: Temperature-Time history measured at a point on the surface of the blade for three heating cycles at a 50mHz Lock-In frequency - Before temperature slope removal

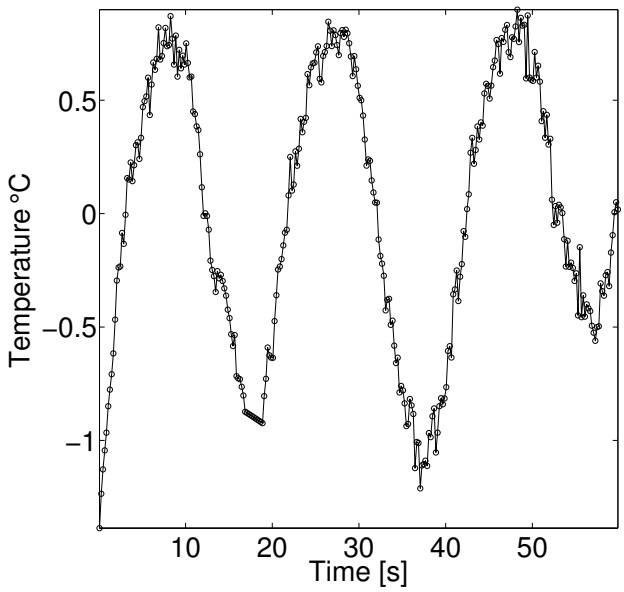

Figure 3.5: Temperature-Time history measured at a point on the surface of the blade for three heating cycles at a 50mHz Lock-In frequency - After temperature slope removal

Fourier Transforms are then used to calculate the amplitude and phase at the Lock-In frequency at each spatial location. The phase and amplitude values are then combined at the different spatial locations to form the phase and amplitude images. The phase image is less susceptible to non-uniform heating and surface irregularities when compared to the amplitude image [41, 53], and it was used for subsequent processing. The phase and amplitude images that were obtained over an area containing a 5.08cm diameter skin-skin delamination at a depth of 1.3mm from the blade surface are shown in Figure 3.6 and 3.7, respectively.

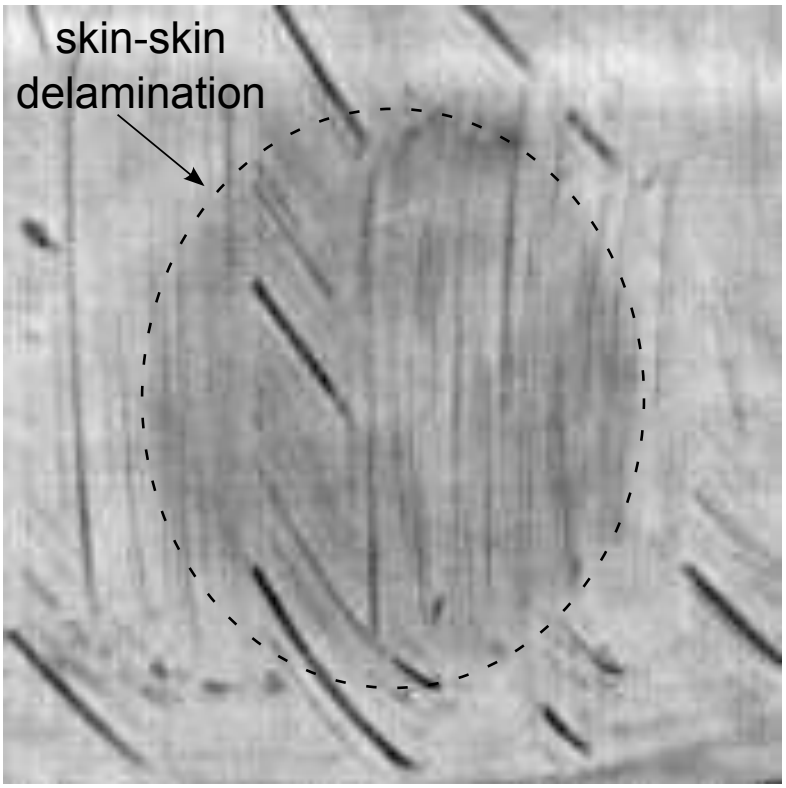

Figure 3.6: Phase image obtained from Lock-In heating at a 50mHz frequency over an area containing a 50.8mm diameter skin-skin delamination at a depth of 1.3mm from the blade surface

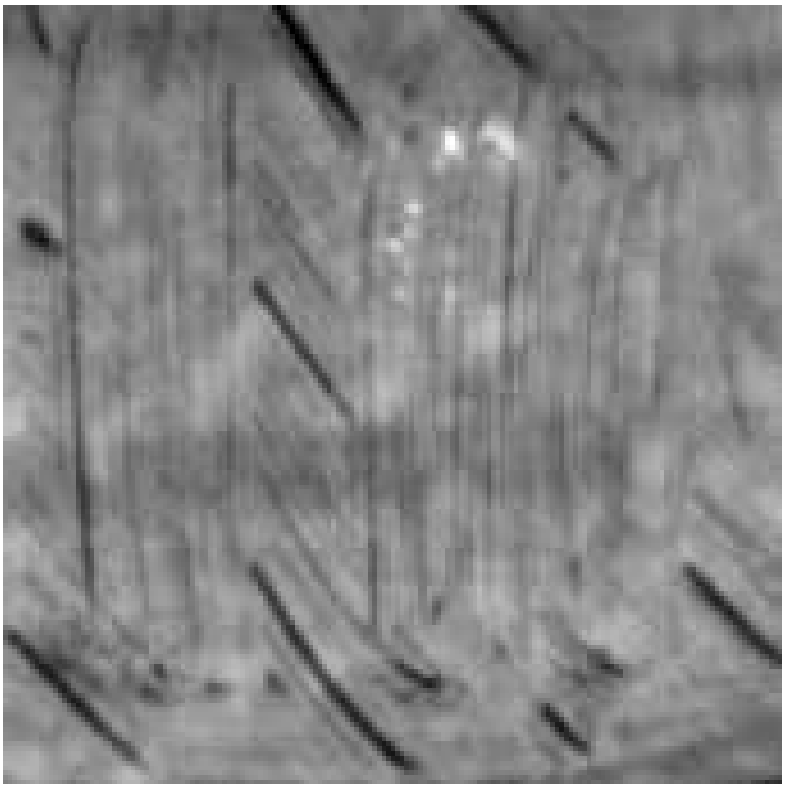

Figure 3.7: Amplitude images obtained from Lock-In heating at a 50mHz frequency over an area containing a 50.8mm diameter skin-skin delamination at a depth of 1.3mm from the blade surface

3.4.2 Image Enhancement

Figure 3.6 shows the presence of the 50.8mm diameter skin-skin delamination at a depth of 1.3mm from the blade surface. While the defect is visible, further contrast gains can be obtained through the use of image processing algorithms. Figure 3.8 shows the distribution of image intensity in the phase image in histogram form. The intensity values are linearly scaled between 0–1 using the maximum and minimum intensity values present in the image. Thresholding is performed at an intensity value to yield a binary image. All spatial locations whose intensity is greater than the threshold value are represented by a white pixel, while all spatial locations whose intensity is lower than the threshold value are represented by a black pixel. Simple morphological operations are then performed on

the thresholded binary image using MATLAB^{TM}. The holes are filled in the binary image, followed by removal of isolated pixels (white pixel surrounded by eight black pixels). Figure 3.9 shows the binary image that is obtained when the phase image is thresholded at a value of 0.7 and after the application of the morphological operations. The different connected components are identified and labeled as shown in Figure 3.10. The area of the different connected components is calculated, and the connected components whose area is less than 5% of the image area are discarded. The final result is shown in Figure 3.11. This final result yields maximum contrast of the defect, and is also now suitable for the quantitative evaluation of the defect detection performance via computation of the Receiver Operating Characteristic curves.

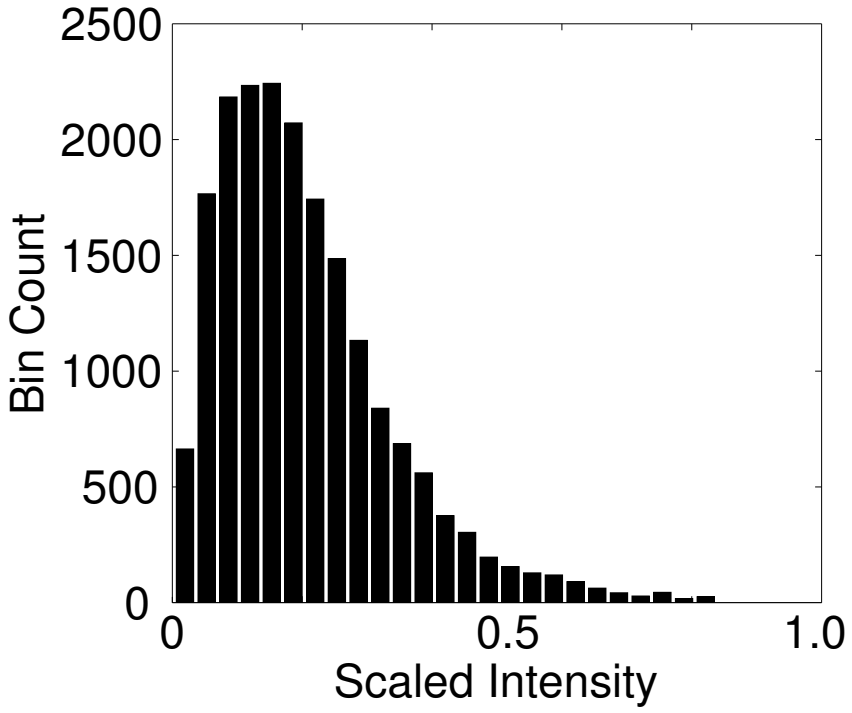

Figure 3.8: Sequence of image processing steps performed on a phase image obtained over an area containing a 50.8mm diameter skin-skin delamination at a depth of 1.3mm from the blade surface. Histogram of the intensity distribution in the phase image. Intensity values are linearly scaled between 0–1

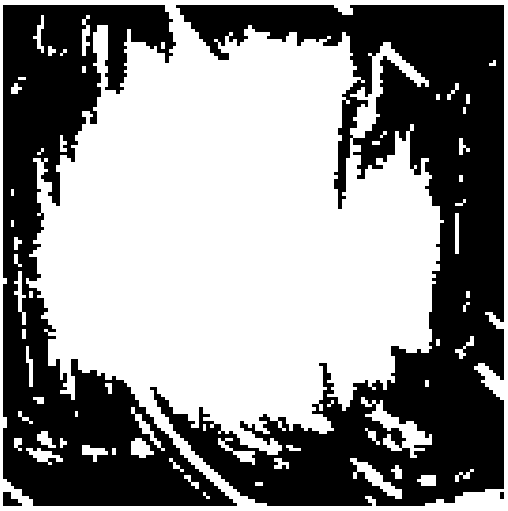

Figure 3.9: Sequence of image processing steps performed on a phase image obtained over an area containing a 50.8mm diameter skin-skin delamination at a depth of 1.3mm from the blade surface. Binary image that is obtained by thresholding the scaled intensity value at 0.7, followed by application of morphological operations

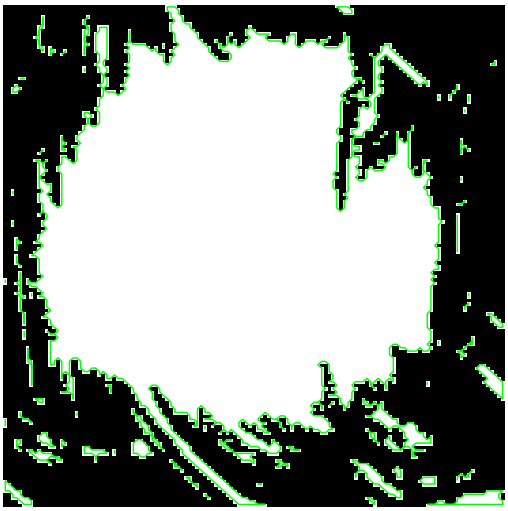

Figure 3.10: Sequence of image processing steps performed on a phase image obtained over an area containing a 50.8mm diameter skin-skin delamination at a depth of 1.3mm from the blade surface. Boundaries of the different connected components

Figure 3.11: Sequence of image processing steps performed on a phase image obtained over an area containing a 50.8mm diameter skin-skin delamination at a depth of 1.3mm from the blade surface. Result of morphological image processing on the phase image shown in Figure3.6

3.4.3 Multivariate Outlier Analysis

Since "blind frequencies" affect defect detection in Lock-In Thermography, five different Lock-In frequencies in the range 30mHz–70mHz were used at each defect location to ensure that at least one of the frequencies provides effective detection. Multivariate Outlier Analysis [71] is an efficient way of combining the spatially registered Lock-In data that are obtained at a defect location at different Lock-In frequencies. An outlier is a datum that appears statistically inconsistent with the baseline. The baseline describes the normal condition of the data set under investigation. The discordancy test in the multivariate case is expressed by the Mahalanobis Squared Distance, D_ζ, which is a non-negative scalar defined as

$$D_\zeta = (x_\zeta - \overline{x})^T [K]^{-1} (x_\zeta - \overline{x}) \tag{3.2}$$

where x_ζ is the potential outlier vector, $\overline{x}$ is the mean vector of the baseline, $[K]$ is the covariance matrix of the baseline, and T represents a transposed matrix. In this study, the data is five dimensional, corresponding to the five different Lock-In frequencies used. Figure 3.12 compares the phase images obtained using Lock-In heating at 30mHz, 50mHz, and 70mHz, respectively. Notice that the phase images

corresponding to Lock-In heating at 30mHz and 50mHz clearly show the presence of defect. Lock-In heating at 70mHz is much less effective. Apart from helping counter the "blind frequency" effects, the use of Multivariate Outlier Analysis helps improving the Signal-to-Noise Ratio of the defective areas by statistically "adding" the contrast performance of multiple Lock-In frequencies.

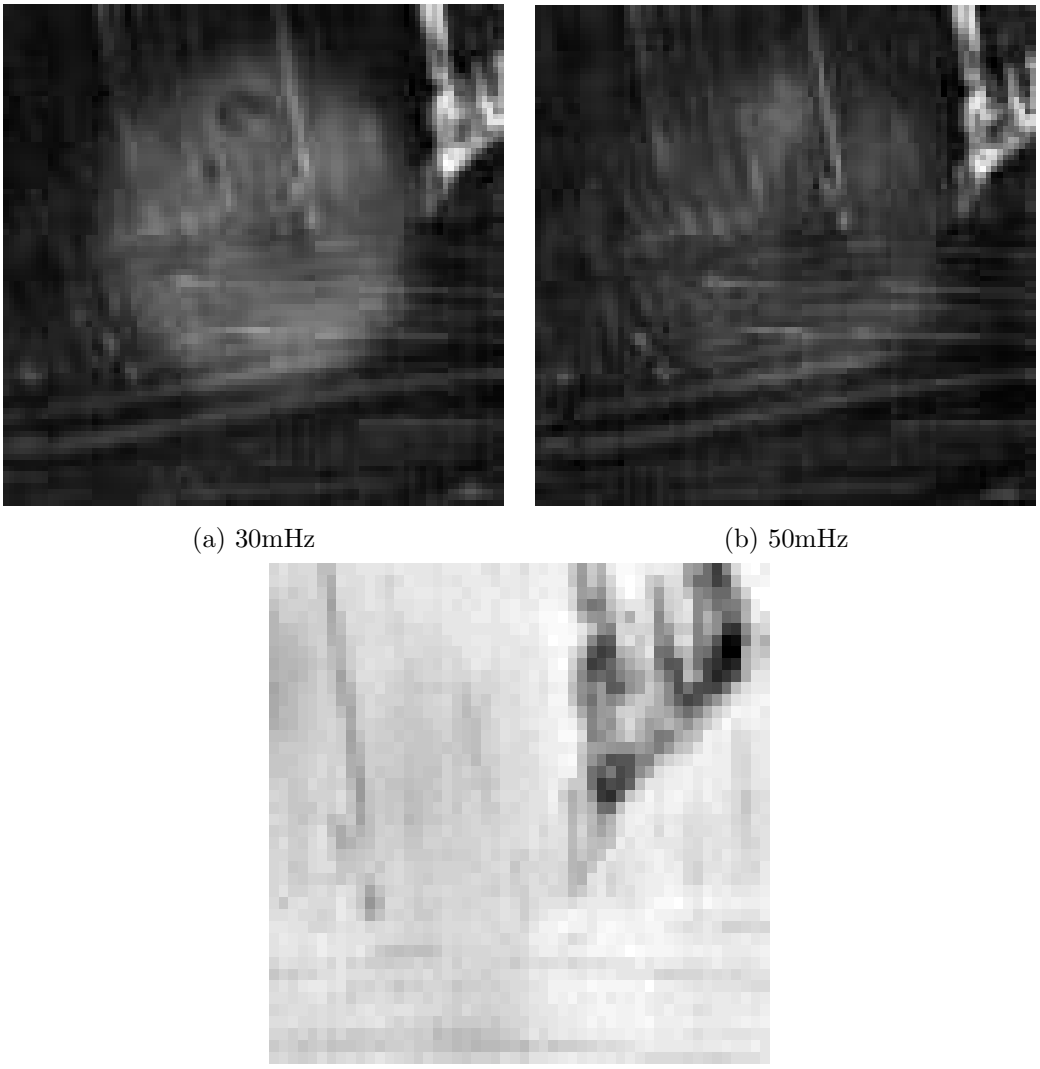

(a) 30mHz

(b) 50mHz

(c) 70mHz

Figure 3.12: Comparison of different Lock-In frequencies at a location containing a 2.54cm diameter skin-skin delamination at a depth of 1.3mm from the blade surface. The phase images were obtained by Lock-In heating over three heating cycles at 30mHz, 50mHz and 70mHz frequency.

3.4.4 Receiver Operating Characteristic Curves

Receiver Operating Characteristic (ROC) curves are a quantitative indicator of performance when comparing different detectors [89]. For each detector and the chosen detection threshold value, the True Positive Rate (TPR) and the False Positive Rate (FPR) can be calculated since the actual locations of the defects in the blade and their sizes are known. For certain applications, a high TPR is desired, while other applications demand a low FPR. The choice of threshold value is ultimately based on the application requirements. In this study, the performance across different thresholds is studied over the sixteen blade defects that are considered as shown in Table 3.1. The thresholds are varied between 0.1–0.9 in steps of 0.05. Figure 3.13 compares the performance of the different detectors against the Multivariate Outlier Analysis detector at a location containing a 5.08cm diameter skin-skin delamination at a depth of 1.3mm from the blade surface. The line connecting the coordinates (0,0)–(1,1) is the "random guess" line. An ideal detector should have TPR of 1 with a FPR of 0 at all thresholds. The best detector is the one that has an ROC curve furthest away from the "random guess" line towards the top left corner of the ROC space.

To quantify the performance of the various detectors considered, the Area Under Curve (AUC) is computed for each of the different detectors using the trapezoidal interpolation. The results are tabulated in Table 3.3 for all the sixteen defects considered. Based on the AUC values in Table 3.3, it can be concluded that in 51 of the 80 total cases, the use of Multivariate Outlier Analysis yields higher AUC over Lock-In heating at any of the individual frequencies. The mean gain in AUC that is obtained by using the Multivariate Outlier Analysis, compared to the 30mHz, 40mHz, 50mHz, 60mHz and 70mHz Lock-In frequencies is 0.96%, 1.73%, 1.79%, 9.36%, and 14.73%, respectively. The overall gain in AUC obtained by Multivariate Outlier Analysis is 5.61% over the individual detectors averaged over the sixteen defects.

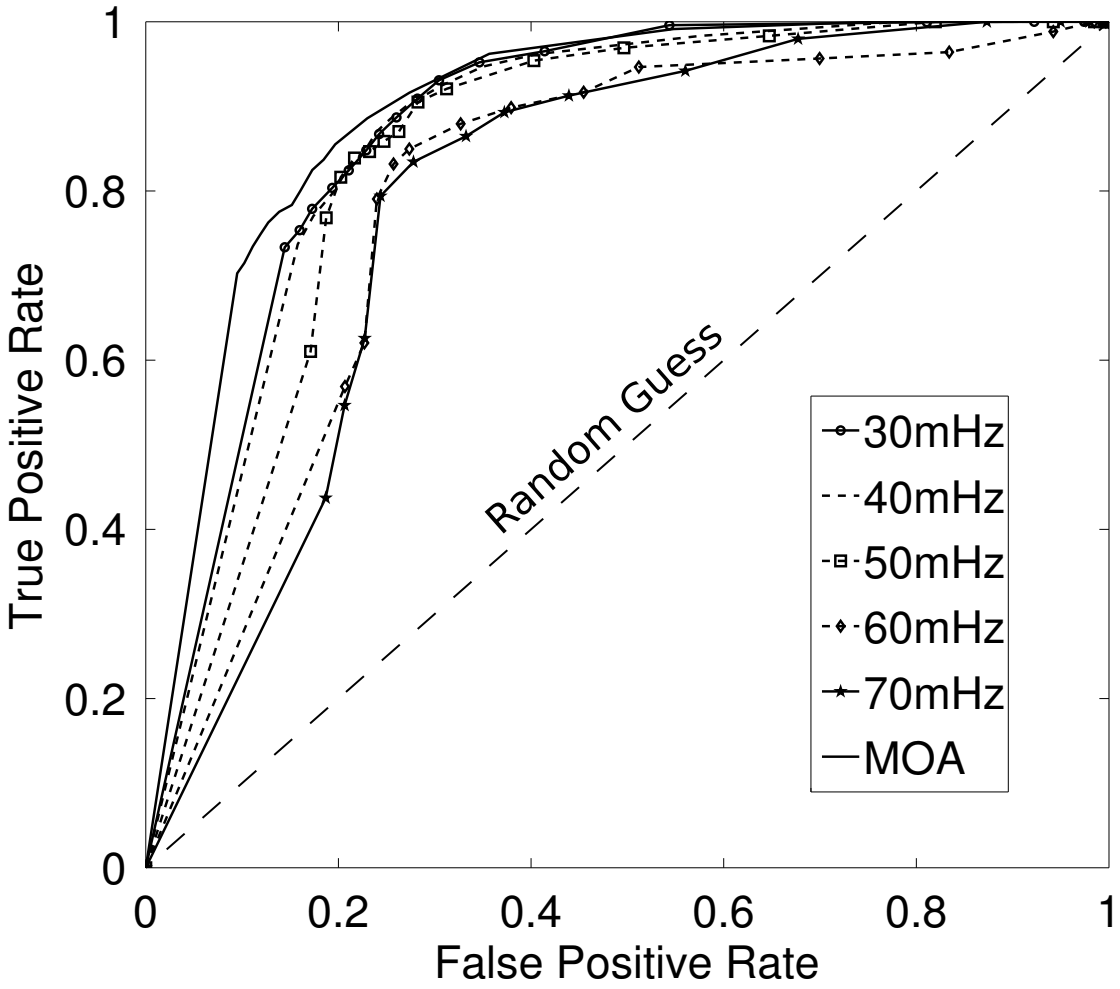

Figure 3.13: Receiver Operating Characteristic curves comparing the performance of five different Lock-In frequencies and the Multivariate Outlier Analysis for different thresholds. The phase images were obtained over an area containing a 5.08cm diameter skin-skin delamination at a depth of 1.3mm from the blade surface.

Table 3.3: Comparison of AUC of the different detectors at the locations of the various defects

Defect Index	Lock-In frequency					M.O.A.
	30mHz	40mHz	50mHz	60mHz	70mHz	
1	0.9961	0.9969	0.9957	0.9968	0.9951	0.9818
2	0.9679	0.9824	0.9877	0.9826	0.9895	0.9874
3	0.9339	0.9501	0.9547	0.9572	0.9589	0.9628
4	0.9015	0.8661	0.8664	0.7870	0.8683	0.8950
5	0.9278	0.9227	0.8927	0.8758	0.6913	0.9244
6	0.9187	0.9082	0.9033	0.8562	0.8287	0.8675
7	0.9434	0.9334	0.7006	0.9164	0.8976	0.9536
8	0.8687	0.8593	0.8374	0.7847	0.7808	0.8907
9	0.8919	0.8868	0.8770	0.4020	0.4018	0.8947
10	0.8541	0.8098	0.8708	0.8352	0.7399	0.8477
11	0.9050	0.9156	0.9029	0.9074	0.6501	0.9226
12	0.9679	0.7901	0.9619	0.9516	0.8505	0.9557
13	0.8398	0.8847	0.9059	0.8637	0.9291	0.8438
14	0.8180	0.9001	0.9171	0.9193	0.8817	0.9280
15	0.8449	0.8290	0.8852	0.8830	0.9027	0.8079
16	0.8286	0.8755	0.8927	0.9088	0.8877	0.8692

3.5 Conclusions

A novel approach combining Lock-In Infrared Thermography, image processing and statistical analysis was proposed to address the problem of defect detection on composite wind turbine blades. Sixteen defects (skin-skin delaminations and skin-core delaminations) ranging in size between 12.7mm–50.8mm, were considered for this study. The depth of the defects were in the range of 0.7mm–1.3mm from the blade surface. Since "blind frequencies" affect defect detection, Lock-In tests were performed at multiple (five) different frequencies at each defect location, to ensure that any defect could be detected by at least one of the Lock-In frequencies. Multivariate Outlier Analysis was then performed on the spatially registered multi-frequency Lock-In data to combine in a statistically robust manner, the defect detection performance of the multiple Lock-In frequencies. Prior to the application of Multivariate Outlier Analysis, image processing algorithms

including binarization and morphological operations were performed on the raw Lock-In thermal phase images. The defect detection performance of the single Lock-In frequencies, and the combined MOA, for various detection thresholds, was quantified via Receiver Operating Characteristic (ROC) curves. The ROC's plot the True Positive Rate (TPR) vs. the False Positive Rate (FPR) computed for the known sixteen test defects. The ROC results demonstrate that the approach of sweeping multiple Lock-In frequencies and combining the phase image results via MOA provides the nest overall defect detection performance compared to any single Lock-In frequency. This result is important in Infrared Thermographic detection of defects in composite structures, where Lock-In schemes are necessary to ensure enough penetration. The effectiveness of the MOA applied to Lock-In thermal phase images derives from (1) the statistical addition of defect contrast yielded by multiple Lock-In frequencies, and (2) the mitigation of the "blind frequency" problem affecting conventional Lock-In Thermography because several Lock-In frequencies are applied at each of the defective areas.

The detection of defects using Lock-In thermography is a slow process. A bulk of the time is spent in the data acquisition process. This could be a concern for deeper defects, since very low Lock-In frequencies are needed to achieve the required thermal diffusion length, especially when five different Lock-In frequencies are used at each location. In a typical carbon fiber composite material, to achieve a thermal diffusion length of about 1", a 1mHz Lock-In frequency needs to be used. The time period is 1000s, corresponding to and acquisition time as long as 3000s. Hence, there is a trade-off between depth of defects targeted and inspection time.

3.6 Acknowledgements

The authors would like to thank the National Science Foundation (Grant #1028365, Dr. George Maracas – Program Manager) and the von Liebig center at the University of California, San Diego. The authors would like to thank Dr. Michael Todd and Dr. Mohan Trivedi for their valuable inputs. Special thanks are extended to Jeffery Tippman, graduate student at UCSD NDE-SHM Lab, and

Mark Rumsey and Dennis Roach of Sandia National Laboratories for advice on the design and defect lay-out of the CX-100 test blade. This chapter, in part, has been submitted for publication in the Structural Health Monitoring journal, Manohar, Arun; Lanza di Scalea, Francesco; (2012). The title of this paper is *Detection of Defects in Wind Turbine Composite Blades using Statistically-Enhanced Lock-In Thermography.* The dissertation author was the primary investigator and primary author of this paper.

Chapter 4

Defect Depth and Size Estimation in Isotropic Materials

4.1 Abstract

The determination of defect depth and size using Pulsed Infrared Thermography is a critical problem. The problem of defect depth estimation has been previously studied using 1D heat conduction models. Unfortunately, 1D heat conduction based models are generally inadequate in predicting heat flow around defects. In this study, a novel approach based on virtual heat sources is proposed to model heat flow around defects accounting for 2D axisymmetric heat conduction. The proposed approach is used to quantitatively determine the defect depth and size. The validity of the model is established using experiments performed on a stainless steel plate specimen with flat bottom holes at different depths.

4.2 Introduction

In the domain of NDT, two problems are of importance. The primary problem is to localize the defect, the secondary problem deals with the estimation of defect depth and size [48, 90]. The problem of defect detection by Infrared Thermography has been studied extensively in the literature. [10, 21, 32, 45, 47, 48]

For the estimation of defect depth, some methods have been proposed based on Pulsed Thermography [48, 91]. Ringermacher's method deals with two cases of heat flow interacting with the flaw. The first is the case of a thin flaw so that heat flows through the flaw (through-heat flaw), and the second case deals with thick flaws where the heat flows around the flaw (lateral-heat flaw). For the case of a through-heat flaw, the stored thermal images are used to determine each pixel's contrast by subtracting the mean pixel intensity for that image (point in time) from the individual pixel's intensity at that point in time. The contrast is then plotted versus time for each pixel. Ringermacher states that the time instant that corresponds to the peak contrast (t_{peak}) is related to the defect depth at that location using the following equation,

$$\text{depth} = \sqrt{\frac{\alpha \times t_{peak}}{3}} \tag{4.1}$$

where α is the thermal diffusivity of the material. In the case of a lateral-heat flaw,

the rate of heat flow is faster around the flaw than through the flaw. This results in the contrast peak not being evident in the pixel contrast plot. A time derivative of the contrast curve is taken in order to determine the derivative contrast peak. The defect depth can then be determined from the peak time using the following equation,

$$\text{depth} = 0.524\pi\sqrt{\alpha \times t_{peak}} \tag{4.2}$$

In the present study, Ringermacher's method was tested experimentally on a 6.24mm thick stainless steel plate containing flat-bottom holes at different depths. The flat-bottom holes are 7.5mm radius each and the depths of the different defects are 0.39mm, 0.92mm, 1.94mm, 2.92mm, 3.94mm, 4.95mm from the surface. A detailed description of the stainless steel plate specimen is presented in the subsequent sections. The flat-bottom holes are ideally supposed to serve as lateral-heat flaws, but the contrast that is obtained indicates that there is considerable through-heat diffusion near the flaws. The result of this experiment is shown in Figure 4.1. Further, from equations 4.1 and 4.2, it can be seen that the defect depth is supposed to be proportional to the square root of the time instant at which the peak contrast occurs. Based on contrast peaks obtained across each defect, it can be seen from Figure 4.2 that this is not the observed case.

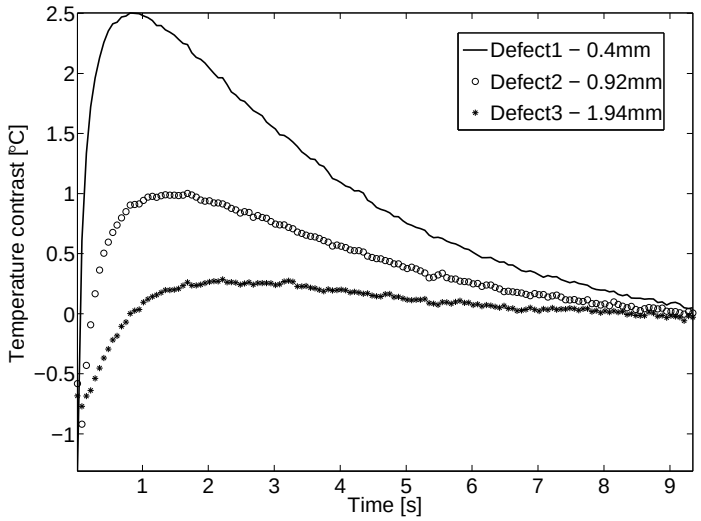

Figure 4.1: Temperature contrast that was obtained experimentally using Ringermacher's method on a steel plate with flat-bottom holes at different depths

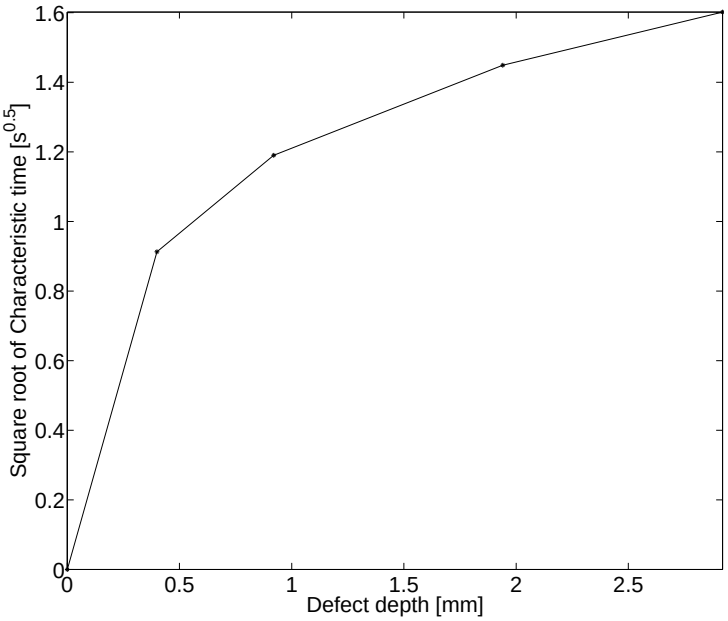

Figure 4.2: Defect depth is not proportional to square root of the characteristic time in the stainless steel plate experiment

Sun [48] proposed the least-squares fitting method to fit the raw thermal data as shown in Equation (1.4). The method is based on Parker's [92] 1D heat conduction solution.

$$T(t) \approx A\left[1 + 2\sum_{n=1}^{\infty} exp\left(-\frac{n^2\pi^2\alpha t}{L^2}\right)\right] - st \tag{4.3}$$

Where L is the thickness of the specimen, A and s are fitting constants. s is determined by linear fitting of the experimental data in the time period $\frac{L^2}{2\alpha} < t < \frac{3L^2}{2\alpha}$. Equation (1.4) is valid for the time instants $0 < t < \frac{3L^2}{2\alpha}$. For a case of defect free sample, s is zero. Since the method involves curve fitting, the undesirable effects of high frequency temporal noise is minimal. The slope s is dependent on the defect gap thickness and the distance of the point to the defect edge. At each spatial point, the depth is computed by fitting the above function with the experimentally obtained data by employing least-squares fitting and Newton iteration techniques. Sun's approach is built on an 1D heat diffusion framework. However, the author mentions that the approach is more accurate compared to conventional methods as it partly accounts for the 3D conduction effects by incorporating the constant

slope decay term.

The basis of most 1D heat conduction based methods comes from Parker's solution [92]. The temperature at any location, z', within a thermally insulated solid at time t is given by,

$$T(z',t) = T_0 \left[\frac{1 + 2\sum_{n=1}^{\infty} \cos\left(\frac{n\pi z'}{L}\right) exp\left(\frac{-n^2\pi^2\alpha t}{L^2}\right)}{3} \right] \tag{4.4}$$

Where T_0 is the initial temperature at the front surface that is caused by a heat pulse on a specimen of thickness L, and Thermal Diffusivity α. Note that z' is the distance from the front surface. Due to absorption of heat at the surface, an instantaneous temperature rise is observed at the surface, which gradually decreases as heat is conducted to the interior.

In Figure 4.3, the experimentally obtained cooling curve over a 1.94mm deep defect present in the stainless steel plate specimen and the 1D cooling curve based on Equation 4.4 are compared. To facilitate easier comparison of the two cooling curves, the results must be presented on the same scale. The maximum and the minimum temperature of each cooling curve is identified and the temperature profiles are linearly scaled using those values between 0-1. For the experiments, the stainless steel specimen was pulse heated with symmetrically placed heat strobes that emit 2400w each. It is clear that the experimental and theoretical cooling curve based on 1D heat conduction do not agree. A likely reason is that heat flow around defects is not 1D.

The limitations of the existing depth estimation methods in Infrared Thermography are evident. An alternative method based on the use of virtual heat sources is proposed in this chapter. The fundamental basis of the method is a 2D axisymmetric heat conduction model. In the subsequent sections, a closed-form analytical solution to the 2D axisymmetric heat conduction problem using appropriate boundary conditions is derived to model the virtual heat source. The results of the model are compared with the experiments that were performed on the stainless steel specimen with flat-bottom holes at different depths. The model is able to accurately estimate the size and depth of the defects considered.

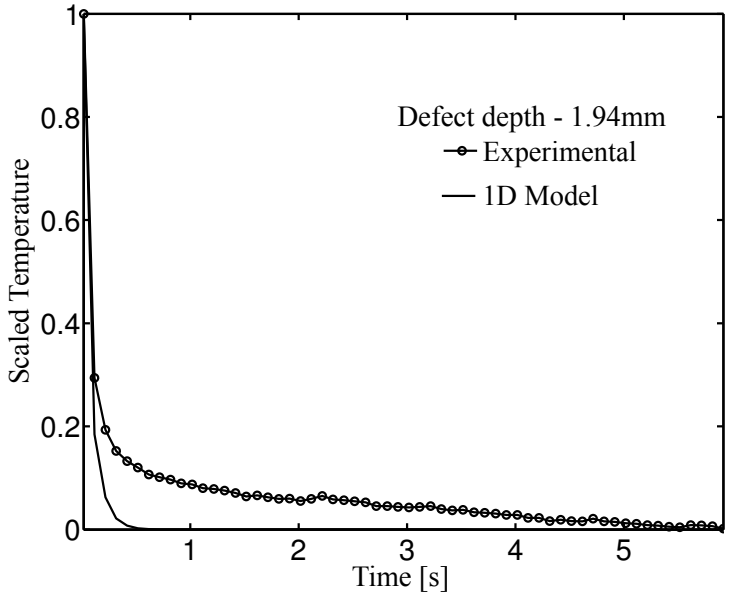

Figure 4.3: Comparison of experimental and 1D theoretical transient heat conduction reference for a 1.94mm deep flat-bottom hole in the stainless steel specimen

4.3 Proposed Heat Diffusion Model for Internal Defects

Consider a cylindrical specimen of radius R and depth L containing a flat-bottom hole at depth d and radius a as shown in Figure 4.4. When a temperature loading in the form of a heat pulse is applied over the surface, slower rate of cooling is observed at an area directly above the defect since the flat-bottom hole resists the flow of heat. The slower rate of cooling can be accounted for by using a virtual heat source that is present at a depth d and radius a. The resulting rate of cooling at the surface, $z = d$ is the sum of two components,

1. 1D heat diffusion that is caused in an object without any defects

2. presence of a virtual heat source at $z = 0$ that causes a slower rate of cooling on the surface, $z = d$

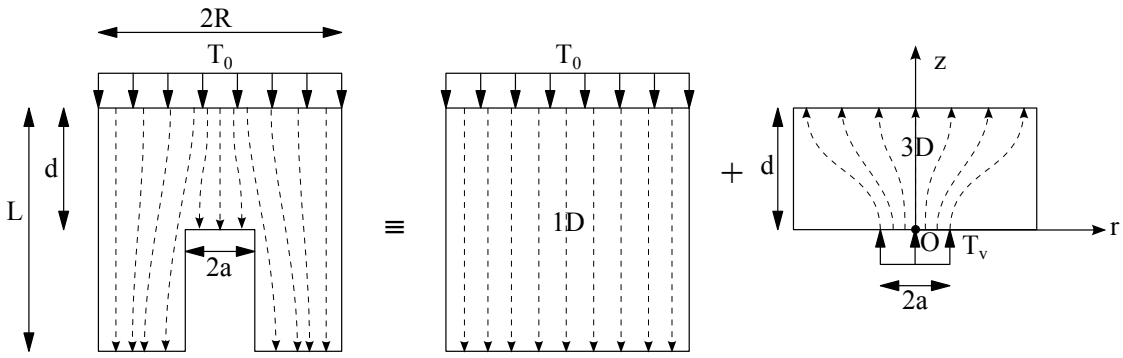

Figure 4.4: Proposed heat diffusion model to account for 2D axisymmetric heat flow around internal defects

Equation 4.4 is the solution to the first effect (1D heat diffusion that is caused in an object without any defects). By letting $T_0 = 1°C$, $L = 6.24mm$ and setting $z' = 0$ in Equation 4.4, Figure 4.5 represents the 1D cooling curve that is obtained at the surface of a defectless specimen of cross-sectional radius R and depth L.

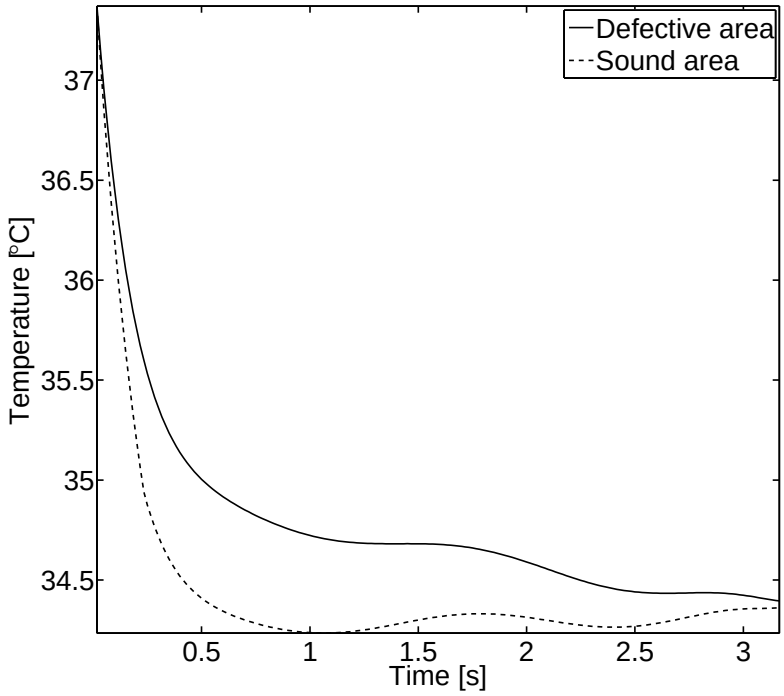

Figure 4.5: Cooling curve obtained at the surface over a defectless area using 1D heat diffusion model

The temperature-time history at a depth d is obtained by setting of $z' = d$ in Equation 4.4. Figure 4.6 shows the temperature-time history at depths corresponding to 0.39mm, 0.92mm, 1.94mm and 2.92mm from the heated surface. In order to present the details clearly, Figure 4.6b shows a zoomed-in section in the narrow time window 0-0.3s. As expected, Figure 4.6 shows that as the depth increases, the temperature amplitude decreases and the time-stamp at which the maxima occurs increases. The location of temperature maxima increases with depth as more time is required to effect a change at that depth.

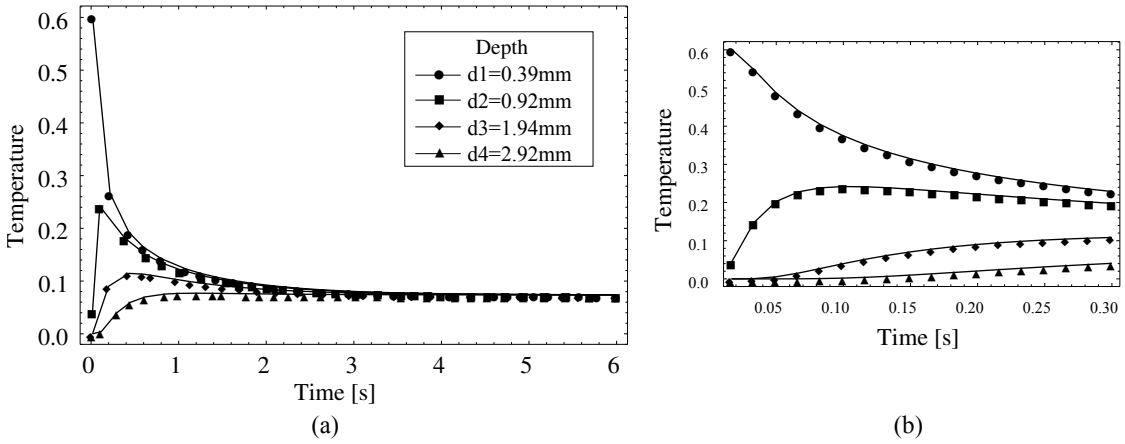

Figure 4.6: (a) Temperature-Time history obtained using the proposed heat diffusion model at four different depths from the surface in a defectless stainless steel specimen (b) Temperature-Time history in the time window 0-0.3s

Next, the effect of the virtual heat source is modeled. The virtual heat source is denoted by T_v and it's units are in degrees Centigrade. Corresponding to a defect at a depth d from the top surface, the authors define T_v as the maximum temperature that is obtained at $z = 0$ when a temperature loading is applied at the surface, $z = d$. The temperature loading is caused by a heat pulse that causes the temperature of the front surface to rise instantaneously to T_0. The coordinate system is defined with respect to origin, O, as shown in Figure 4.4. Mathematically,

$$T_v = \text{Max}\left\{ T_0 \left[\frac{1 + 2\sum_{n=1}^{\infty} \cos\left(\frac{n\pi d}{L}\right) exp\left(\frac{-n^2\pi^2\alpha t}{L^2}\right)}{3} \right] \right\} \tag{4.5}$$

From Figure 4.6, corresponding to defects at depths 0.39mm, 0.92mm, 1.94mm and 2.92mm, T_v can be computed as 0.6, 0.24, 0.11 and 0.07, respectively.

The heat conduction problem has to be solved in a cylindrical region with radial symmetry. This condition implies the assumption of defects with circular cross-section that are oriented parallel to the specimen's surface. The governing heat conduction equation in the cylindrical coordinates where r is the radial coordinate and z the depth coordinate is given by Carslaw et al. [93]

$$\frac{\partial^2 T}{\partial z^2} + \frac{1}{r}\frac{\partial}{\partial r}\left(r\frac{\partial T}{\partial r}\right) = \frac{1}{\alpha}\frac{\partial T}{\partial t} \tag{4.6}$$

The equation has to be solved in the region $0 \leq r \leq R$ and $0 \leq z \leq d$ (see Figure 4.4), with insulated ends at $r = R$, $z = 0$ and $z = d$, subject to initial temperature, T_v, on the surface $z = 0$ in the range $0 \leq r \leq a$. The nature of boundary conditions permits the separation of Equation 4.6 into two separate problems in the radial and depth direction [93]. The solutions are therefore obtained in the radial and depth dimension separately before merging them [94].

Let $T_1(r, t)$ be the solution of the radial part, therefore,

$$\frac{1}{r}\frac{\partial}{\partial r}\left(r\frac{\partial T_1}{\partial r}\right) = \frac{1}{\alpha}\frac{\partial T_1}{\partial t} \tag{4.7}$$

in the region $0 \leq r \leq R$, with initial condition and boundary conditions,

$$\begin{aligned} &T_1 = T_v && 0 \leq r \leq a, && t = 0 \\ &T_1 \text{ is bounded} && r = 0, && t > 0 \\ &\frac{\partial T_1}{\partial r} = 0 && r = R, && t > 0 \end{aligned} \tag{4.8}$$

Similarly, let $T_2(z, t)$ be the solution of the depth part, therefore,

$$\frac{\partial^2 T_2}{\partial z^2} = \frac{1}{\alpha}\frac{\partial T_2}{\partial t} \tag{4.9}$$

in the region $0 \leq z \leq d$ with initial condition and boundary conditions,

$$\begin{aligned} &T_2 = 1 && z = 0, && t = 0 \\ &T_2 = 0 && 0 < z \leq d, && t = 0 \\ &\frac{\partial T_2}{\partial z} = 0 && z = 0, && t > 0 \\ &\frac{\partial T_2}{\partial z} = 0 && z = d, && t > 0 \end{aligned} \tag{4.10}$$

$T = T_1(r,t)T_2(z,t)$ is the solution of equation 4.6 in the region $0 \leq r \leq R$ and $0 \leq z \leq d$ with initial conditions $T = T_v$ at the surface $z = 0$ for $0 \leq r \leq a$ and boundary conditions for T_1 and T_2 given in Equations 4.8 and 4.10.

Equations 4.7 and 4.9 are solved separately. At first the radial part of the solution is addressed by solving Equation 4.7 using boundary and initial conditions given in Equation 4.8.

Let $T_1(r,t) = k_1(r)k_2(t)$. Then from equation 4.7,

$$k_2\frac{\partial^2 k_1}{\partial r^2} + k_2\frac{1}{r}\frac{\partial k_1}{\partial r} = k_1\frac{1}{\alpha}\frac{\partial k_2}{\partial t} \tag{4.11}$$

The above equation can be written as,

$$\frac{1}{k_1}\left[\frac{\partial^2 k_1}{\partial r^2} + \frac{1}{r}\frac{\partial k_1}{\partial r}\right] = \frac{1}{k_2}\frac{1}{\alpha}\frac{\partial k_2}{\partial t} \tag{4.12}$$

By letting both sides of the equation equal to the constant, $-\mu^2$, we have

$$\frac{\partial^2 k_1}{\partial r^2} + \frac{1}{r}\frac{\partial k_1}{\partial r} + k_1\mu^2 = 0 \tag{4.13}$$

and

$$\frac{\partial k_2}{\partial t} + k_2\alpha\mu^2 = 0 \tag{4.14}$$

Solving by standard methods yields, $k_2(t) = c_1 e^{-t\alpha\mu^2}$ and $k_1(r) = c_2 J_0(r\mu) + c_3 Y_0(r\mu)$. J_0 is the Bessel's function of the first kind with order 0 and Y_0 is the Bessel's function of the second kind with order 0. c_1, c_2, c_3 and μ are constants that need to determined based on the prescribed initial and boundary conditions in the radial direction. It should be noted that Y_0, the Bessel's function of the second kind at order 0, is unbounded at $r = 0$. For boundedness of the solution, $c_3 = 0$. No flux condition at $r = R$ implies, $\dfrac{\partial T}{\partial r} = 0$, and hence $\dfrac{\partial k_1}{\partial r} = 0$. This implies $-\mu c_2 J_1(r\mu) = 0$ as $\dfrac{\partial J_0(\mu r)}{\partial r} = -\mu J_1(\mu r)$. For non-trivial solutions, $J_1(\mu R) = 0$. Using standard tables for roots of Bessel functions, the roots of the function are 3.83, 7.01, 10.17 .... Thus, $T_1(r,t)$ can be written as the product of $k_1(r)$ and $k_2(t)$.

$$T_1(r,t) = c_1 c_2 e^{-\mu^2\alpha t} J_0(\mu r) \tag{4.15}$$

where $\mu \in \left\{\frac{3.83}{R}, \frac{7.01}{R}, \frac{10.17}{R} \ldots\right\}$. By letting $c_1 c_2 = A$, a constant, and by using principle of superposition of the solutions, we have,

$$T_1(r,t) = \sum_{n=1}^{\infty} A_n e^{-\mu_n^2 \alpha t} J_0(\mu_n r) \tag{4.16}$$

A_n are a series of multiplicative constants that need to determined by using the initial conditions and properties of Bessel's functions. At $t = 0$,

$$\sum_{n=1}^{\infty} A_n J_0(\mu_n r) = \begin{cases} T_v & 0 \leq r \leq a \\ 0 & a < r \leq R \end{cases} \tag{4.17}$$

If μ_n and μ_m are roots of $J_0'(\mu R) = 0$, it follows that [93],

$$\begin{aligned} &\int_0^R r J_0(\mu_n r) J_0(\mu_m r)\, dr = 0 \qquad\qquad \forall m \neq n, \\ &\int_0^R r \left\{J_0(\mu_n r)\right\}^2 dr = \frac{R^2}{2} \left\{J_0(\mu_n R)\right\}^2 \end{aligned} \tag{4.18}$$

Multiplying both sides of Equation 4.17 by $r J_0(\mu_n r)\, dr$ and integrating between the limits 0 to R, we have,

$$A_n \int_0^R \left\{J_0(\mu_n r)\right\}^2 r\, dr = \int_0^a T_v J_0(\mu_n r) r\, dr \tag{4.19}$$

On further simplifying using Equation 4.18,

$$A_n = \frac{2T_v}{R^2 J_0^2(\mu_n R)} \int_0^a J_0(\mu_n r) r\, dr \tag{4.20}$$

The radial part of the solution can be written as,

$$T_1(r,t) = \sum_{n=1}^{\infty} \frac{2T_v}{R^2 J_0^2(\mu_n R)} \left(\int_0^a J_0(\mu_n r) r\, dr \right) e^{-\mu_n^2 \alpha t} J_0(\mu_n r) \tag{4.21}$$

where $\mu_n \in \left\{\frac{3.83}{R}, \frac{7.01}{R}, \frac{10.17}{R} \ldots\right\}$. For solution completeness, a constant first term analogous to the Fourier series has to be added to the expansion [93]. The constant first term would be $\frac{2}{R^2} \int_0^R \zeta f(\zeta)\, d\zeta$ which reduces to $\frac{2}{R^2} \int_0^a \zeta T_v\, d\zeta$ for the given set of boundary and initial conditions. Thus, the constant first term equals $T_v \frac{a^2}{R^2}$. The radial part of the solution with the added constant term can be finally written as,

$$T_1(r,t) = T_v \left[\frac{a^2}{R^2} + 2 \sum_{n=1}^{\infty} \frac{\int_0^a J_0(\mu_n r) r\, dr}{R^2 J_0^2(\mu_n R)} e^{-\mu_n^2 \alpha t} J_0(\mu_n r) \right] \tag{4.22}$$

Equation 4.9 is now solved to determine $T_2(z,t)$ using boundary and initial conditions given in Equations 4.10. By letting $T_2(z,t) = k_3(z)k_4(t)$. Equation 4.9 simplifies to,

$$k_4 \frac{\partial^2 k_3}{\partial z^2} = k_3 \frac{1}{\alpha} \frac{\partial k_4}{\partial t} \tag{4.23}$$

By letting both sides of the equation equal to the constant, $-\lambda^2$, and rearranging, we have,

$$\frac{\partial^2 k_3}{\partial z^2} + k_3 \lambda^2 = 0 \tag{4.24}$$

and

$$\frac{\partial k_4}{\partial t} + \alpha k_4 \lambda^2 = 0 \tag{4.25}$$

Solving Equations 4.24 and 4.25 yields, $k_3(z) = c_5 \cos(\lambda z) + c_6 \sin(\lambda z)$ and $k_4(t) = c_4 e^{-t\alpha\lambda^2}$ and by using the boundary conditions in the z direction, we have $\dfrac{\partial k_3}{\partial z} = 0$ at $z = 0$ and $z = d$.

$$\frac{\partial k_3}{\partial z} = \lambda \left(-c_5 \sin(\lambda z) + c_6 \cos(\lambda z)\right) \tag{4.26}$$

$\dfrac{\partial k_3}{\partial z} = 0$ at $z = 0$ implies $c_6 = 0$, and $\dfrac{\partial k_3}{\partial z} = 0$ at $z = d$ implies $-c_5 \lambda \sin(\lambda d) = 0$. For non-trivial solutions, $\sin(\lambda d) = 0$ which implies, $\lambda = \dfrac{m\pi}{d}$ for $m = 1, 2, 3, \ldots$. Thus,

$$k_3(z) = c_5 \cos\left(\frac{m\pi z}{d}\right), \qquad m = 1, 2, 3, \ldots \tag{4.27}$$

The resulting solution of the partial differential equation in the z direction is a product of $k_3(z)$ and $k_4(t)$,

$$T_2(z,t) = B \cos\left(\frac{m\pi z}{d}\right) e^{-\left(\frac{m\pi}{d}\right)^2 \alpha t}, \qquad m = 1, 2, 3, \ldots \tag{4.28}$$

where $B = c_4 c_5$ is an arbitrary multiplicative constant. By principle of superimposition, the above equation can be written as

$$T_2(z,t) = \sum_{m=0}^{\infty} B_m \cos\left(\frac{m\pi z}{d}\right) e^{-\left(\frac{m\pi}{d}\right)^2 \alpha t} \tag{4.29}$$

The series of constants, B_m will be determined using the initial condition in the z direction.

$$\sum_{n=0}^{\infty} B_n \cos\left(\frac{n\pi z}{d}\right) = \begin{cases} 1 & z = 0 \\ 0 & 0 < z \leq d \end{cases} \tag{4.30}$$

By using,

$$\int_0^d \cos\frac{k_1\pi z}{d}\cos\frac{k_2\pi z}{d}\,dz = \begin{cases} 0 & k_1 \neq k_2 \\ \frac{d}{2} & k_1 = k_2 \neq 0 \\ d & k_1 = k_2 = 0 \end{cases} \tag{4.31}$$

Thus, $B_0 = 1$ and $B_m = 2$ for all $m \geq 1$. The solution in the z direction can be written as,

$$T_2(z,t) = 1 + 2\sum_{m=1}^{\infty}\cos\left(\frac{m\pi z}{d}\right)e^{-\left(\frac{m\pi}{d}\right)^2\alpha t} \tag{4.32}$$

The overall heat conduction solution is obtained as a product of $T_1(r,t)$ and $T_2(z,t)$ and can be written as,

$$\begin{aligned} T(r,z,t) =& T_v\left[1 + 2\sum_{m=1}^{\infty}\cos\left(\frac{m\pi z}{d}\right)e^{-\left(\frac{m\pi}{d}\right)^2\alpha t}\right] \\ &\times\left[\frac{a^2}{R^2} + 2\sum_{n=1}^{\infty}\frac{\int_0^a J_0(\mu_n r)r\,dr}{R^2J_0^2(\mu_n R)}e^{-\mu_n^2\alpha t}J_0(\mu_n r)\right] \end{aligned} \tag{4.33}$$

where $\mu_n \in \left\{\frac{3.83}{R}, \frac{7.01}{R}, \frac{10.17}{R}\ldots\right\}$. Equation 4.33 represents the 2D axisymmetric solution of the virtual heat source internal to the object. Heat conduction happens both in the radial as well as the depth direction.

The effect of the virtual heat source at the center-point of surface above the defect can be calculated by letting $z = d$, $r = 0$ in Equation 4.33 and by using the appropriate T_v corresponding to the defect. Equation 4.33 reduces to,

$$T_{vsrc} = T_v\left[1 + 2\sum_{m=1}^{\infty}\cos(m\pi)\,e^{-\left(\frac{m\pi}{d}\right)^2\alpha t}\right]\times\left[\frac{a^2}{R^2} + 2\sum_{n=1}^{\infty}\frac{\int_0^a J_0(\mu_n r)r\,dr}{R^2J_0^2(\mu_n R)}e^{-\mu_n^2\alpha t}\right] \tag{4.34}$$

where $\mu_n \in \left\{\frac{3.83}{R}, \frac{7.01}{R}, \frac{10.17}{R}\ldots\right\}$. For the stainless steel experimental specimen discussed in the next section, $a = 7.5$mm, $R = 20$mm, $\alpha = 4.05 * 10^{-6}\mathrm{m^2s^{-1}}$. Corresponding to the shallowest defect, $d = 0.39$mm and $T_v = 0.6$. 50 terms were used in the summation in the radial and depth directions. Figure 4.7 shows the surface temperature-time history that is obtained from the model, corresponding to virtual heat sources present at different depths. It is evident that the effect of the virtual heat sources on the surface decreases with the defect depth.

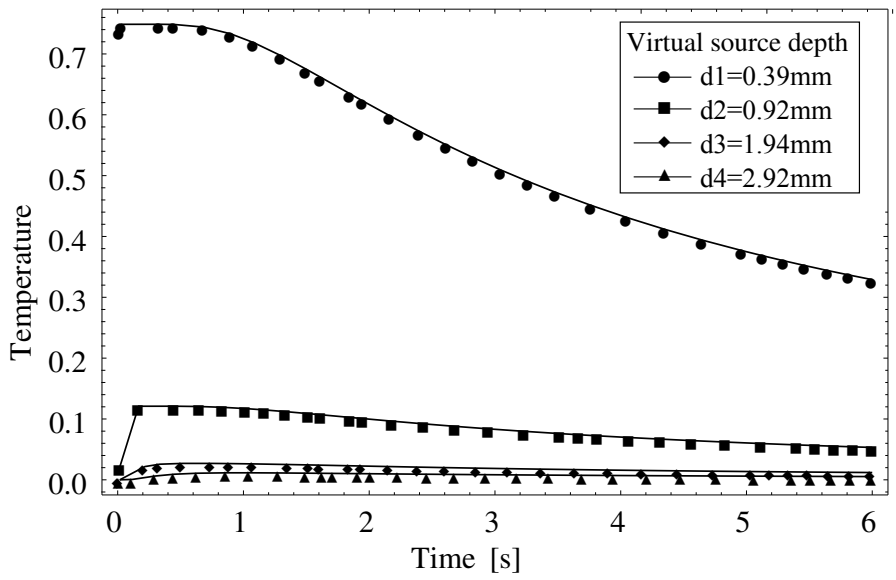

Figure 4.7: Comparison of the effect of virtual heat sources at the surface, caused by the presence of defects at different depths, from the proposed heat diffusion model

The resulting cooling profile at the surface of a defective sample is obtained as the sum of 1D heat diffusion that is caused in an object without any defects and the effect of a virtual heat source at $z = 0$. Mathematically, it is represented as the sum of Equation 4.4 and Equation 4.34.

$$\begin{aligned} T =& T_0 \left[\frac{1 + 2\sum_{n=1}^{\infty} \cos\left(\frac{n\pi d}{L}\right) exp\left(\frac{-n^2\pi^2\alpha t}{L^2}\right)}{3} \right] + \\ & T_v \left[1 + 2\sum_{m=1}^{\infty} \cos(m\pi)\, e^{-\left(\frac{m\pi}{d}\right)^2 \alpha t} \right] \left[\frac{a^2}{R^2} + 2\sum_{n=1}^{\infty} \frac{\int_0^a J_0(\mu_n r) r\, dr}{R^2 J_0^2(\mu_n R)} e^{-\mu_n^2 \alpha t} \right] \end{aligned} \tag{4.35}$$

From Equation 4.35, given the surface temperature loading T_0, defect depth d, defect radius a, depth of the test specimen L, Thermal Diffusivity α, the model can predict the cooling curve at the surface. T_v is calculated using Equation 4.5. Figure 4.8 compares the model-predicted cooling curve that is obtained on the surface of the stainless steel specimen containing flat-bottom holes at depths 0.39mm, 0.92mm, 1.94mm and 2.92mm from the surface. For easier comparison of the cooling curves, the individual cooling curves are linearly scaled between 0-1.

It is important to also point out that the proposed heat diffusion model can not only account for the different depths, but it can also account for different defect sizes as long as the defect cross-section is circular and the defect orientation is parallel to the specimen's surface (circular flat-bottom holes and circular cracks). In fact, for defects of different size at the same depth, the model can predict the cooling curve at the surface by altering the value of parameter a in Equation 4.35. A larger defect corresponds to a larger virtual heat source, while a small defect corresponds to a smaller virtual heat source. Figure 4.9 compares the cooling curve that is obtained for two defects at depth 1mm, whose radii are 5mm and 15mm respectively. The 15mm radius defect produces a slower cooling rate at the surface than the 5mm radius defect. This can be attributed to the intuitive fact that larger defects offer more resistance to the flow of heat more than smaller defects.

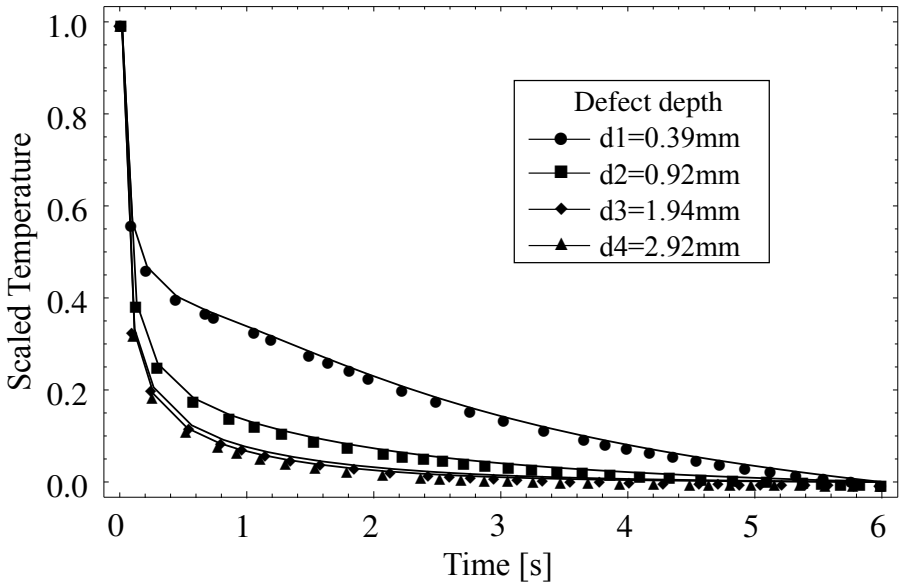

Figure 4.8: Predicted cooling curves over defective areas of the stainless steel specimen containing flat-bottom holes at depths of 0.39mm, 0.92mm, 1.92mm and 2.94mm using the proposed model

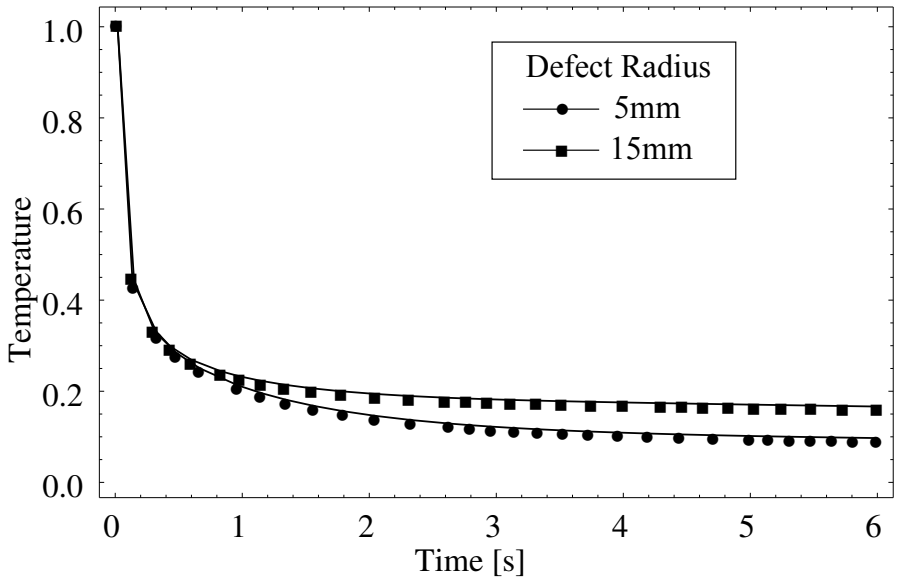

Figure 4.9: Comparison of defects of different sizes at the same depth in stainless steel using the proposed heat diffusion model

4.4 Experimental Tests

4.4.1 Experimental Setup and Data Collection

The experimental setup used for the Pulsed Thermography experiments is shown in Figure 4.10. A Speedotron^{TM} 4800W power pack was used to trigger two strobes which output 2400W each with a flash duration of 1/300s. In order to have a fairly uniform heating profile on the surface, the two strobes were placed symmetrically with respect to the test specimen. The strobes cause an instantaneous temperature increase, followed by cooling due to diffusion of heat into the interior.

The cooling trend is captured by the FLIR^{TM} A320G Infrared camera which acquires data at 60Hz. The detector is a focal plane array uncooled microbolometer with a spectral range of $7.5 - 13\mu m$ and the resolution is 240x320 pixels. The detector pitch is $25\mu m$ and the detector time constant is $12ms$. The Thermal Sensitivity of the camera is 50mK. The focal length of the lens is $18mm$ and the f-number is 1.3 with a spatial resolution of 1.3 mrad. The 16 bit data is transferred

to a laptop via ethernet where it is further processed.

Experiments were performed on a 6.24mm thick 304-stainless steel plate sample with six flat-bottom holes at known depths as shown in Figure 4.11. The flat-bottom holes are 7.5mm radius each at the following depths: 0.39mm, 0.92mm, 1.94mm, 2.92mm, 3.94mm and 4.95mm from the surface. The front surface of the stainless steel specimen was coated with black paint to maximize heat absorption. The front and back surfaces of the stainless steel plate are assumed to be insulated in the proposed heat diffusion model. In reality, there is a very small convective heat loss to the surroundings.

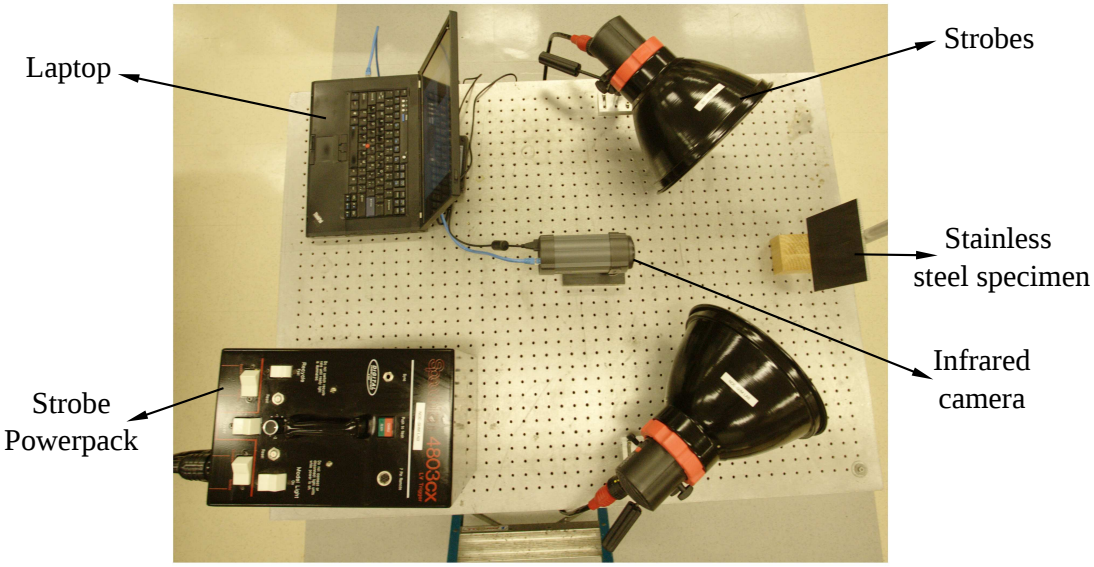

Figure 4.10: Pulsed Thermography experimental setup

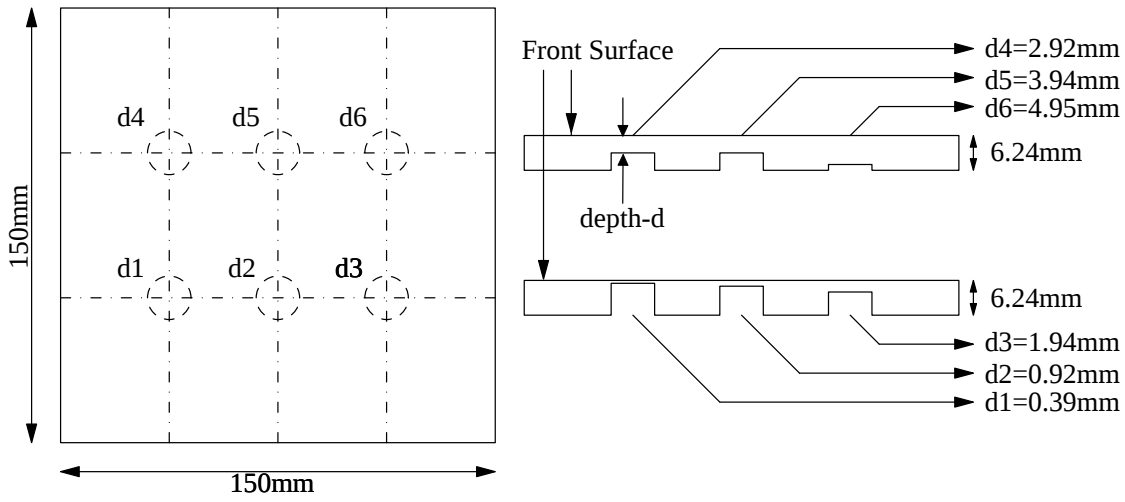

Figure 4.11: Schematic of defects in Stainless Steel plate test specimen

4.4.2 Experimental Results

The model-predicted cooling curves and the experimental results obtained on the stainless steel specimen are compared in this section. The model-predicted cooling curve and the experimentally obtained cooling curve above a defectless area are shown in Figure 4.12. The model-predicted cooling curves are compared with experiments at the surface of locations containing flat-bottom defects at depths 0.39mm, 0.92mm, 1.92mm and 2.92mm in Figures 4.13-4.16. In all cases, there is an excellent agreement between the model and the experiments. The flat-bottom defects present at 3.94mm and 4.95mm depth from the surface could not be detected as they were found to be too deep to be detected by the Pulsed Thermography setup utilized in the tests. The Infrared camera used in the tests had a Thermal Sensitivity of about 50mK which is quite low compared to the more costly Infrared cameras that are typically used in Pulsed Thermography NDE, which have a Thermal Sensitivity of about 18mK.

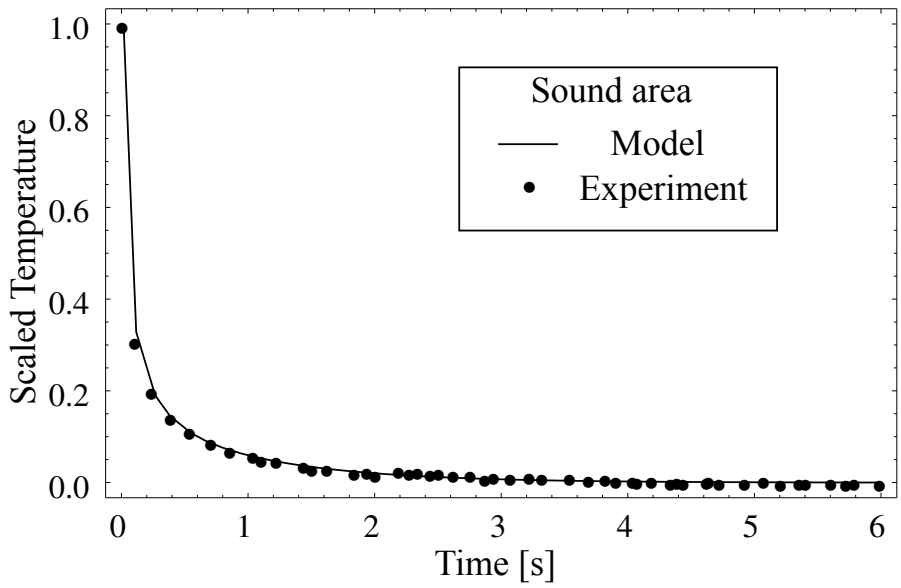

Figure 4.12: Comparison of experimental and model-predicted cooling curves at a sound area

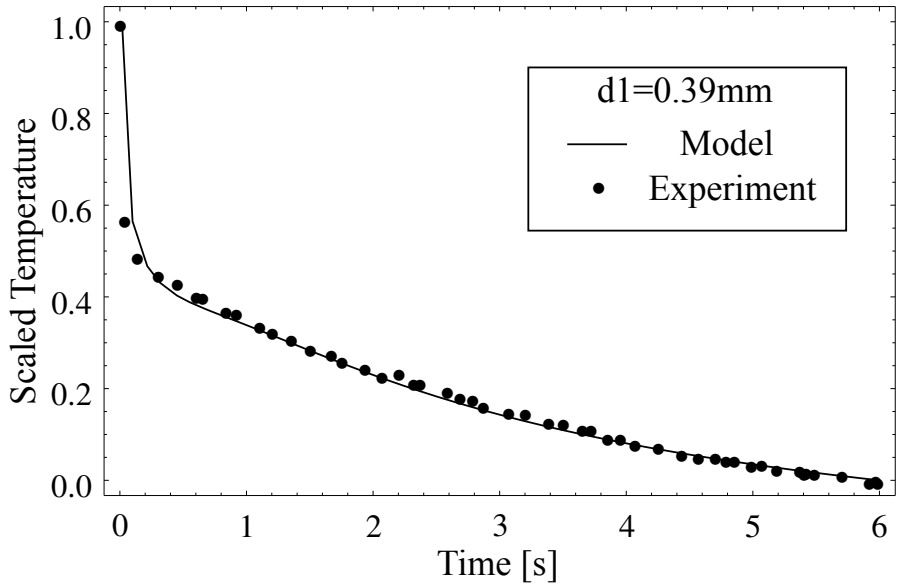

Figure 4.13: Comparison of experimental and model-predicted cooling curves for different defect present in the stainless steel specimen at depth of 0.39mm from the surface

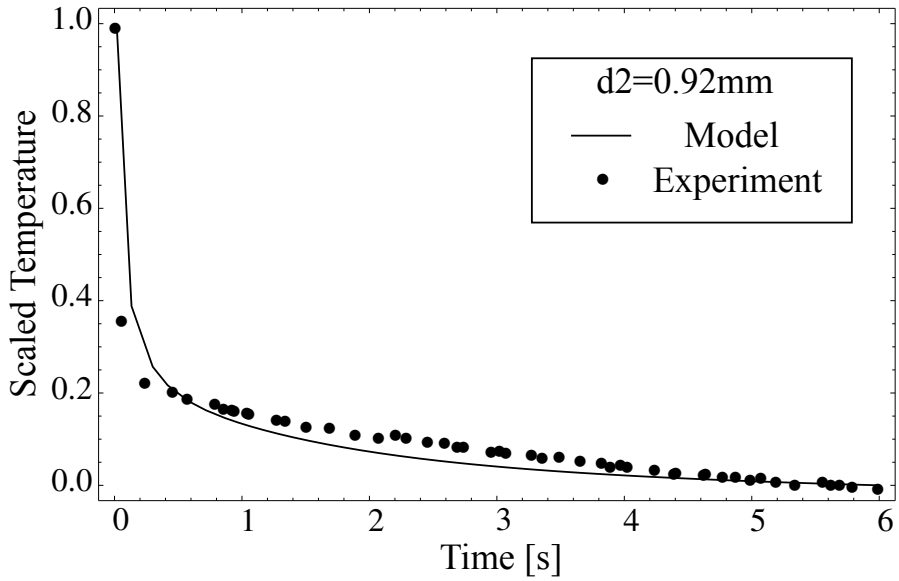

Figure 4.14: Comparison of experimental and model-predicted cooling curves for different defect present in the stainless steel specimen at depth of 0.92mm from the surface

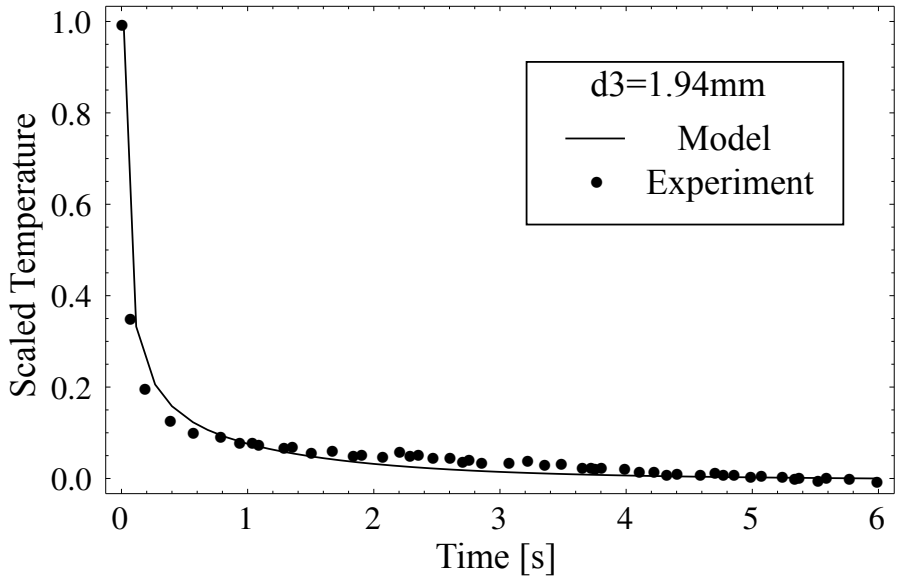

Figure 4.15: Comparison of experimental and model-predicted cooling curves for different defect present in the stainless steel specimen at depth of 1.94mm from the surface

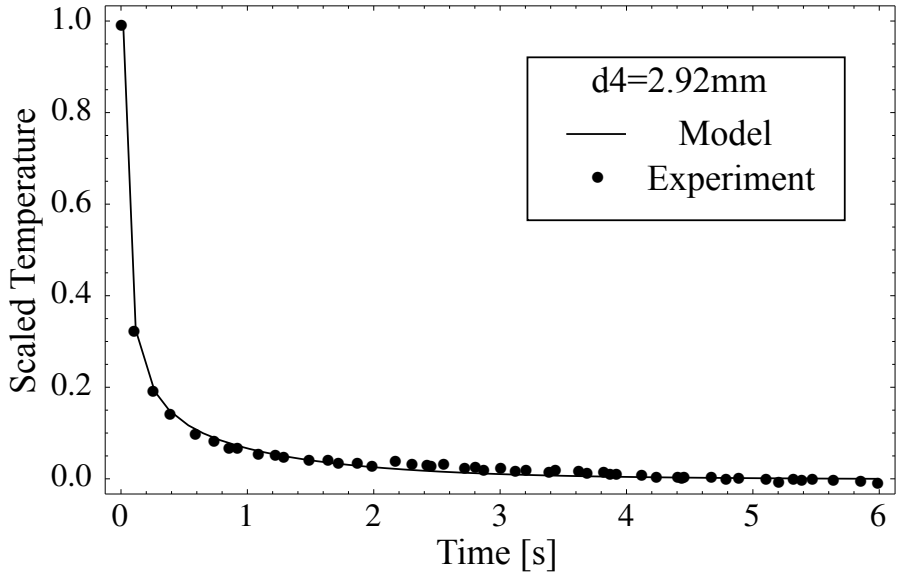

Figure 4.16: Comparison of experimental and model-predicted cooling curves for different defect present in the stainless steel specimen at depth of 2.92mm from the surface

4.5 Conclusions

Defect depth and size estimation in Pulsed Infrared Thermography is usually based on 1D heat conduction models. However, 1D heat conduction based models are generally inadequate in predicting the heat flow around defects. A novel method based on virtual heat sources was proposed to account for the 2D axisymmetric heat diffusion around defects and accurately predict the defect depth and size using Pulsed Infrared Thermography. The model predictions of surface temperature cooling trends were compared to experimental results obtained on a stainless steel plate specimen with flat-bottom holes drilled at different depths. The match was found to be quite satisfactory, validating the model. In the modeling process, perfectly insulated boundary conditions were assumed, whereas, in reality there is a small convective heat loss to the surroundings which could cause minor errors in the predicted cooling curves. Due to the low Thermal Sensitivity of the Infrared camera that was used, the two deepest defects could not be detected in the experiments. The model uses values of defect depth and defect

size independently, and it can therefore be parameterized to predict both of these quantities.

4.6 Acknowledgements

The authors would like to thank the National Science Foundation (Grant #1028365, Dr. George Maracas – Program Manager) and the von Liebig center at the University of California, San Diego for funding the project through a Department of Energy fellowship. This chapter, in part, has been published in the Experimental Mechanics journal, Manohar, Arun; Lanza di Scalea, Francesco; (2012). The title of this paper is *Determination of Defect Depth and Size using Virtual Heat Sources in Pulsed Infrared Thermography.* The dissertation author was the primary investigator and primary author of this paper.

Chapter 5

Defect Depth and Size Estimation in Quasi-Isotropic Materials

5.1 Abstract

In this chapter, a novel approach based on 3D heat conduction is proposed to estimate the defect depth and size in quasi-isotropic composite structures. The proposed approach uses the excess temperature profile that is obtained over a defective area with respect to a sound area to estimate the defect dimensions and depth. The modeling process involved extensive coordinate transformations to reduce the anisotropic heat conduction problem to the isotropic domain, followed by separation of variables to solve the partial differential equation. The validity of the model and approach is established using Pulsed Thermography experiments performed on a composite panel containing rectangular flat-bottom holes of different sizes, present at different depths.

5.2 Introduction

Composites are becoming an integral part of high performance structures in the aerospace and wind energy industry. Accurate and efficient NDT methods are needed to monitor the state of health of these structures [36, 40, 61, 61, 62, 62–64, 80, 82–85, 95]. Most of the existing methods on defect size and depth estimation in Infrared Thermography NDT are based on the assumption of 1D heat diffusion, the solution of which is based on the study by Parker et al. [92]. In most cases of extended defects, the heat flow interaction with defects is more than one dimensional as shown in Figure 5.1a, especially in the case of composites with different thermal properties in different directions. It was discussed earlier how simple 1D heat diffusion based models are unable to predict accurately the heat diffusion around defects, hence the estimation of defect size and depth is not accurate.

When a pulse of thermal energy is deposited on the surface of an object, heat flows to the interior of the object, thereby, cooling the surface. When the heat flow encounters a defect, heat flows around it. The presence of the defect hampers heat flow to the interior, causing a build up of heat directly above the defective area. However, in a sound area (an area without any underlying defect), heat flows quicker due to the absence of any resistance. For the two points, 1 and

2, considered in Figure 5.1a, Figure 5.1b shows the temperature profile with time.

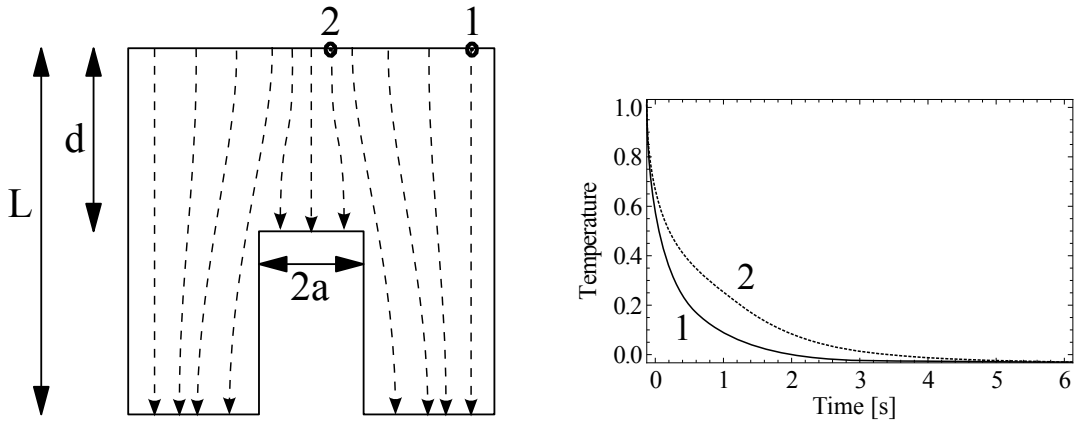

(a) Heat flow around a defect

(b) Comparison of cooling at points over the defective area and a sound area

Figure 5.1: The rate of cooling at a point above the defective area is slower due to the resistance offered to the flow of heat by the presence of the defect

Based on the cooling curve obtained over a defective area with respect to the sound area, which will be referred to by "excess temperature", and denoted by T_e, the authors propose to determine the defect size and depth. Figure 5.2 shows a typical excess temperature variation with time obtained over a defective area with respect to the sound area. The excess temperature is caused by the presence of the defect which resists the flow of heat, which is modeled using virtual heat sources. The concept of virtual heat sources was introduced by the author of this dissertation in a previous work [20]. The previous study discussed in the chapter 4 of this dissertation involved studies on homogeneous and isotropic materials like stainless steel that contained 2D axisymmetric defects like flat-bottom holes. In this chapter, the concept is extended to quasi-isotropic composites containing rectangular defects. In the subsequent sections, the heat flow interaction with defects is modeled and a closed-form analytical solution is derived to represent the excess temperature. The results of the model were compared with Pulsed Thermography experiments that were performed on a quasi-isotropic composite panel containing rectangular flat-bottom defects. Specifically, the test specimen that was fabricated was 6mm thick and contained nine rectangular, flat-bottom defects

of different sizes, present at different depths from the surface. The experimental results obtained validated the model.

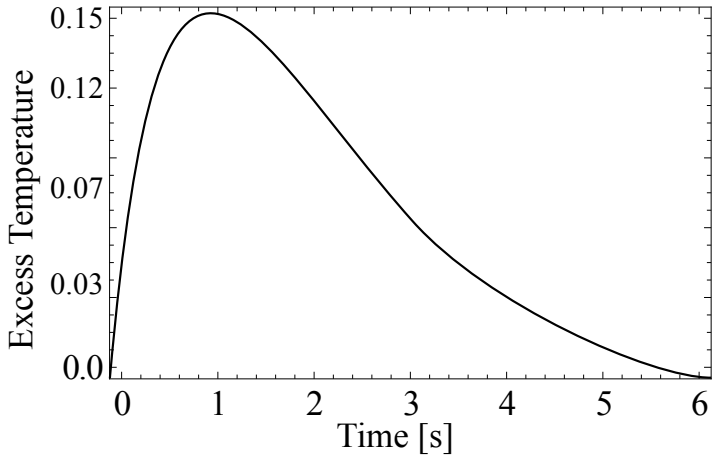

Figure 5.2: The excess temperature that builds up over a defective area with time with reference to the sound area

5.3 Modeling Heat Flow in Composites

Figure 5.3 depicts the based idea of the modeling process. The excess temperature that is obtained over a surface containing an underlying defect can be modeled using the virtual heat source introduced in chapter 4. The virtual heat source is present at a depth d from the surface and it has the same dimensions as the underlying flaw.

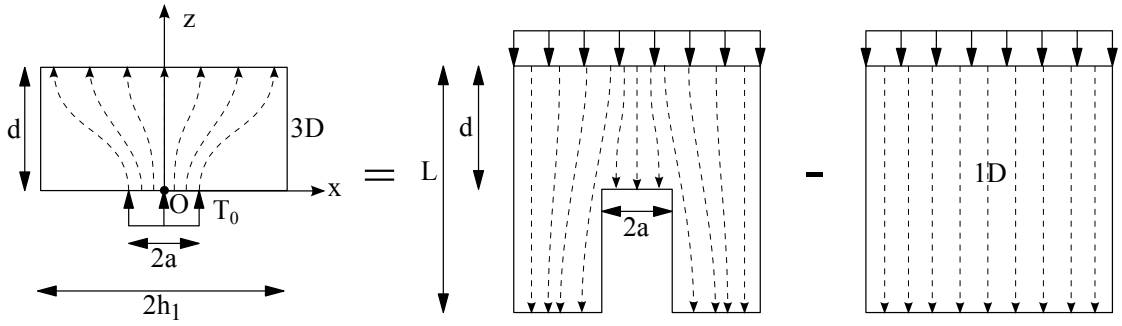

Figure 5.3: Modeling the presence of the defect in composite structures

The governing equation of the flow of heat in a composite plate with density

ρ, specific heat capacity c is given by,

$$\rho c \frac{\partial T}{\partial t} = K_p \left(\frac{\partial^2 T}{\partial x^2} + \frac{\partial^2 T}{\partial y^2} \right) + K_z \frac{\partial^2 T}{\partial z^2} \tag{5.1}$$

Since we are assuming a quasi-isotropic material here, the thermal conductivity is the same along all directions in the x-y plane. The x-y-z coordinate system is defined with respect to origin, O, as shown in Figure 5.4. K_p refers to the longitudinal thermal conductivity in the $x-y$ plane and K_z refers to the transverse thermal conductivity in the z direction. The boundary conditions correspond to the case of insulated surfaces at $x = \pm h_1$, $y = \pm h_2$ $z = 0$ and $z = d$. At $t = 0$, the surface $z = 0$, $-a \leq x \leq a$, $-b \leq y \leq b$ is subjected to a heat pulse of magnitude T_0. It is assumed that the heat is absorbed over a very thin layer of material whose thickness is δ. The set of boundary and initial conditions is shown in Equation 5.2.

$$\begin{array}{lll}
\frac{\partial T}{\partial x} = 0 & x = \pm h_1, & t > 0 \\
\frac{\partial T}{\partial y} = 0 & y = \pm h_2, & t > 0 \\
\frac{\partial T}{\partial z} = 0 & z = 0 \text{ and } z = d & t > 0 \\
T = T_0 & 0 \leq z \leq \delta, -a \leq x \leq a, -b \leq y \leq b, & t = 0 \\
T = 0 & \delta < z \leq d, -a \leq x \leq a, -b \leq y \leq b, & t = 0
\end{array} \tag{5.2}$$

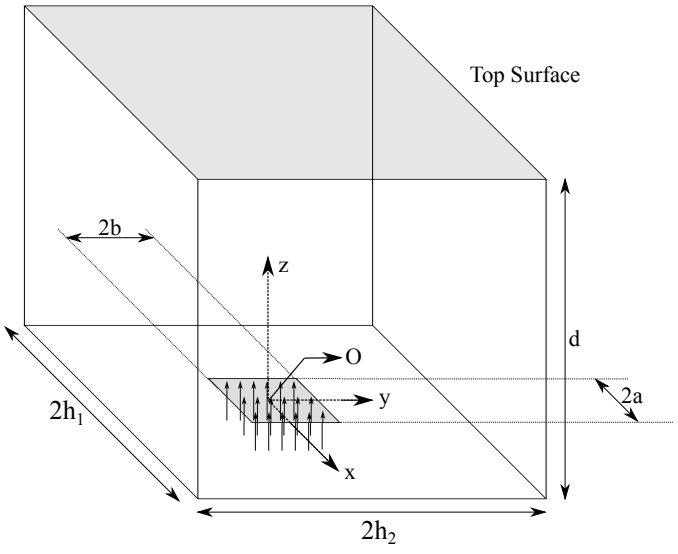

Figure 5.4: Virtual Source heating model

Equation 5.1 depicts the heat conduction equation in a quasi-isotropic material, which is difficult to solve analytically. Carslaw et al. [93] suggest the following coordinate transformation that will reduce the problem to an isotropic domain. By letting, $X = x\left(\frac{K}{K_p}\right)^{\frac{1}{2}}$, $Y = y\left(\frac{K}{K_p}\right)^{\frac{1}{2}}$ and $Z = z\left(\frac{K}{K_z}\right)^{\frac{1}{2}}$, Equation 5.1 transforms to,

$$\rho c\frac{\partial T}{\partial t} = K\left(\frac{\partial^2 T}{\partial X^2} + \frac{\partial^2 T}{\partial Y^2} + \frac{\partial^2 T}{\partial Z^2}\right) \tag{5.3}$$

The boundary conditions in Equation 5.2 transform to,

$$\begin{aligned} &\tfrac{\partial T}{\partial X} = 0, && X = \pm h_1\left(\tfrac{K}{K_p}\right)^{\frac{1}{2}} \\ &\tfrac{\partial T}{\partial Y} = 0, && Y = \pm h_2\left(\tfrac{K}{K_p}\right)^{\frac{1}{2}} \\ &\tfrac{\partial T}{\partial Z} = 0, && Z = 0 \text{ and } Z = d\left(\tfrac{K}{K_z}\right)^{\frac{1}{2}} \end{aligned} \tag{5.4}$$

In the region, $-a\left(\frac{K}{K_p}\right)^{\frac{1}{2}} \leq X \leq a\left(\frac{K}{K_p}\right)^{\frac{1}{2}}, -b\left(\frac{K}{K_p}\right)^{\frac{1}{2}} \leq Y \leq b\left(\frac{K}{K_p}\right)^{\frac{1}{2}}$, the initial conditions in Equation 5.2 transform to,

$$\begin{aligned} &T = T_0 && 0 \leq Z \leq \delta\left(\tfrac{K}{K_z}\right)^{\frac{1}{2}} \\ &T = 0 && \delta\left(\tfrac{K}{K_z}\right)^{\frac{1}{2}} < Z \leq d\left(\tfrac{K}{K_z}\right)^{\frac{1}{2}} \end{aligned} \tag{5.5}$$

An infinitesimal element's volume must be the same in the $x-y-z$ and $X-Y-Z$ coordinate systems [96]. Thus, $dx\,dy\,dz = dX\,dY\,dZ$. From the above set of transformations, $dX = dx\left(\frac{K}{K_p}\right)^{\frac{1}{2}}$, $dY = dy\left(\frac{K}{K_p}\right)^{\frac{1}{2}}$ and $dZ = dz\left(\frac{K}{K_z}\right)^{\frac{1}{2}}$ and hence $K = \left(K_p^2 K_z\right)^{\frac{1}{3}}$. By letting $\alpha = \frac{K}{\rho c}$, Equation 5.3 can be written as,

$$\frac{1}{\alpha}\frac{\partial T}{\partial t} = \left(\frac{\partial^2 T}{\partial X^2} + \frac{\partial^2 T}{\partial Y^2} + \frac{\partial^2 T}{\partial Z^2}\right) \tag{5.6}$$

Equation 5.6 can be solved analytically [94] with the transformed set of boundary and initial conditions. The nature of boundary and initial conditions permit the separation of the problem into three separate problems in the X, Y and Z directions [93]. Let T_X be the solution of $\frac{1}{\alpha}\frac{\partial T_X}{\partial t} = \frac{\partial^2 T_X}{\partial X^2}$. Similarly, let T_Y and T_Z be the solutions of $\frac{1}{\alpha}\frac{\partial T_Y}{\partial t} = \frac{\partial^2 T_Y}{\partial Y^2}$ and $\frac{1}{\alpha}\frac{\partial T_Z}{\partial t} = \frac{\partial^2 T_Z}{\partial Z^2}$ respectively. The final solution for Equation 5.6 with the set of boundary and initial conditions shown in Equation 5.4 is obtained as a product of T_X, T_Y and T_Z.

In the X direction, the partial differential equation to be solved and the set of boundary and initial conditions is,

$$\begin{aligned}
&\tfrac{1}{\alpha}\tfrac{\partial T_X}{\partial t} = \tfrac{\partial^2 T_X}{\partial X^2} \\
&\tfrac{\partial T_X}{\partial X} = 0 \qquad && X = \pm h_1 \left(\tfrac{K_z}{K_p}\right)^{\frac{1}{6}}, && t > 0 \\
&T_X = 1 \qquad && -a\left(\tfrac{K_z}{K_p}\right)^{\frac{1}{6}} \leq X \leq a\left(\tfrac{K_z}{K_p}\right)^{\frac{1}{6}}, && t = 0
\end{aligned} \tag{5.7}$$

By letting $\beta = \left(\tfrac{K_z}{K_p}\right)^{\frac{1}{6}}$, Equations 5.7 simplifies to,

$$\begin{aligned}
&\tfrac{1}{\alpha}\tfrac{\partial T_X}{\partial t} = \tfrac{\partial^2 T_X}{\partial X^2} \\
&\tfrac{\partial T_X}{\partial X} = 0 \qquad && X = \pm h_1\beta, && t > 0 \\
&T_X = 1 \qquad && -a\beta \leq X \leq a\beta, && t = 0
\end{aligned} \tag{5.8}$$

Similarly, the set of equations in the Y direction is given by,

$$\begin{aligned}
&\tfrac{1}{\alpha}\tfrac{\partial T_Y}{\partial t} = \tfrac{\partial^2 T_Y}{\partial Y^2} \\
&\tfrac{\partial T_Y}{\partial Y} = 0 \qquad && Y = \pm h_2\beta, && t > 0 \\
&T_Y = 1 \qquad && -b\beta \leq Y \leq b\beta, && t = 0
\end{aligned} \tag{5.9}$$

In the Z direction,

$$\begin{aligned}
&\tfrac{1}{\alpha}\tfrac{\partial T_Z}{\partial t} = \tfrac{\partial^2 T_Z}{\partial Z^2} \\
&\tfrac{\partial T_Z}{\partial Z} = 0 \qquad && Z = 0 \text{ and } Z = \tfrac{d}{\beta^2}, && t > 0 \\
&T_Z = T_0 \qquad && 0 \leq Z \leq \tfrac{\delta}{\beta^2}, && t = 0 \\
&T_Z = 0 \qquad && \tfrac{\delta}{\beta^2} < Z \leq \tfrac{d}{\beta^2}, && t = 0
\end{aligned} \tag{5.10}$$

The most general solution for the partial differential equation in the X direction is,

$$T_X = \left(c_1 \sin(\lambda_1 X) + c_2 \cos(\lambda_1 X)\right) e^{-t\alpha\lambda_1^2} \tag{5.11}$$

where c_1, c_2 and λ_1 are general constants that need to determined using the prescribed boundary and initial conditions. The partial derivative in the X direction is given by,

$$\frac{\partial T_X}{\partial X} = \left(c_1\lambda_1 \cos(\lambda_1 X) - c_2\lambda_1 \sin(\lambda_1 X)\right) e^{-t\alpha\lambda_1^2} \tag{5.12}$$

Using boundary conditions from Equation 5.8, we have,

$$\begin{aligned}
c_1\lambda_1 \cos(\lambda_1 h_1\beta) + c_2\lambda_1 \sin(\lambda_1 h_1\beta) = 0 \\
c_1\lambda_1 \cos(\lambda_1 h_1\beta) - c_2\lambda_1 \sin(\lambda_1 h_1\beta) = 0
\end{aligned} \tag{5.13}$$

The set of equations implies that either $c_1 = 0$ or $c_2 = 0$ and for non-trivial solutions, $c_2\lambda_1 \sin(\lambda_1 h_1 \beta) = 0$ or $c_1\lambda_1 \cos(\lambda_1 h_1 \beta) = 0$, respectively. In this study, $c_1 = 0$ is picked. For non-trivial solutions, $\sin(\lambda_1 h_1 \beta) = 0$. This implies $\lambda_1 = \frac{n\pi}{h_1\beta}$, where n is any integer. The most general solution is, $T_X = c_2 \cos\left(\frac{n\pi X}{h_1\beta}\right) e^{-t\alpha\left(\frac{n\pi}{h_1\beta}\right)^2}$. By using principle of superposition of the solutions, we have,

$$T_X = \sum_{n=0}^{\infty} c_n \cos\left(\frac{n\pi X}{h_1\beta}\right) e^{-t\alpha\left(\frac{n\pi}{h_1\beta}\right)^2} \tag{5.14}$$

c_n are a series of multiplicative constants that need to determined by using the initial conditions and by using the orthogonality property of cosines. At $t = 0$, $T_X = 1$ for $-a\beta \leq X \leq a\beta$.

$$\sum_{n=0}^{\infty} c_n \cos\left(\frac{n\pi X}{h_1\beta}\right) = 1 \qquad -a\beta \leq X \leq a\beta \tag{5.15}$$

By using orthogonality property of cosines,

$$\int_{-h_1\beta}^{h_1\beta} \cos\frac{n_1\pi X}{h_1\beta} \cos\frac{n_2\pi X}{h_1\beta}\, dX = \begin{cases} 0 & n_1 \neq n_2 \\ h_1\beta & n_1 = n_2 \neq 0 \\ 2h_1\beta & n_1 = n_2 = 0 \end{cases} \tag{5.16}$$

Thus, $c_0 = \frac{a}{h_1}$ and $c_n = \frac{1}{h_1\beta}\int_{-a\beta}^{a\beta} \cos\left(\frac{n\pi X}{h_1\beta}\right) dX$. This implies $c_n = \frac{2}{n\pi}\sin\left(\frac{n\pi a}{h_1}\right)$ for all $n \neq 0$. The general solution in the X direction can be written as,

$$T_X = \frac{a}{h_1} + \sum_{n=1}^{\infty} \frac{2}{n\pi} \sin\left(\frac{n\pi a}{h_1}\right) \cos\left(\frac{n\pi X}{h_1\beta}\right) e^{-t\alpha\left(\frac{n\pi}{h_1\beta}\right)^2} \tag{5.17}$$

Since the governing equation, boundary conditions and the initial conditions in the Y direction are similar to the X direction, the general solution in the Y direction can be written as

$$T_Y = \frac{b}{h_2} + \sum_{m=1}^{\infty} \frac{2}{m\pi} \sin\left(\frac{m\pi b}{h_2}\right) \cos\left(\frac{m\pi Y}{h_2\beta}\right) e^{-t\alpha\left(\frac{m\pi}{h_2\beta}\right)^2} \tag{5.18}$$

In the Z direction, the most general solution is,

$$T_Z = \left(c_3 \sin(\lambda_3 Z) + c_4 \cos(\lambda_3 Z)\right) e^{-t\alpha\lambda_3^2} \tag{5.19}$$

where c_3, c_4 and λ_3 are general constants that need to determined using the prescribed boundary and initial conditions. The partial derivative in the Z direction is given by,

$$\frac{\partial T_Z}{\partial Z} = \left(c_3\lambda_3\cos(\lambda_3 Z) - c_4\lambda_3\sin(\lambda_3 Z)\right)e^{-t\alpha\lambda_3^2} \tag{5.20}$$

Using boundary conditions from Equation 5.10, we have, $\frac{\partial T_Z}{\partial Z} = 0$ at $Z = 0$ implies $c_3\lambda_3\cos(\lambda_3 Z) = 0$ and hence $c_3 = 0$. $\frac{\partial T_Z}{\partial Z} = 0$ at $Z = \frac{d}{\beta^2}$ implies $c_4\lambda_3\sin(\frac{d\lambda_3}{\beta^2}) = 0$. For non-trivial solutions, $\frac{d\lambda_3}{\beta^2} = k\pi$ which implies $\lambda_3 = \frac{k\pi\beta^2}{d}$ for any integer k. Thus, $T_Z = c_4\cos\left(\frac{k\pi\beta^2 Z}{d}\right)e^{-t\alpha\left(\frac{k\pi\beta^2}{d}\right)^2}$. By using principle of superposition of the solutions, we have,

$$T_Z = \sum_{k=0}^{\infty} c_k\cos\left(\frac{k\pi\beta^2 Z}{d}\right)e^{-t\alpha\left(\frac{k\pi\beta^2}{d}\right)^2} \tag{5.21}$$

c_k are a series of multiplicative constants that need to determined by using the initial conditions and by using the orthogonality property of cosines. At $t = 0$,

$$\sum_{k=0}^{\infty} c_k\cos\left(\frac{k\pi\beta^2 Z}{d}\right) = \begin{cases} T_0 & 0 \le Z \le \frac{\delta}{\beta^2} \\ 0 & \frac{\delta}{\beta^2} < Z \le \frac{d}{\beta^2} \end{cases} \tag{5.22}$$

By using orthogonality property of cosines,

$$\int_0^{\frac{d}{\beta^2}} \cos\frac{k_1\pi\beta^2 Z}{d}\cos\frac{k_2\pi\beta^2 Z}{d}\,dZ = \begin{cases} 0 & k_1 \neq k_2 \\ \frac{d}{2\beta^2} & k_1 = k_2 \neq 0 \\ \frac{d}{\beta^2} & k_1 = k_2 = 0 \end{cases} \tag{5.23}$$

Thus, $c_0 = \frac{\delta T_0}{d}$ and $c_k = \frac{2T_0}{k\pi}\sin(\frac{k\pi\delta}{d})$ for all $k \neq 0$. The general solution in the Z direction can be written as,

$$T_Z = T_0\frac{\delta}{d}\left(1 + \sum_{k=1}^{\infty} 2\frac{\sin(\frac{k\pi\delta}{d})}{\frac{k\pi\delta}{d}}\cos\left(\frac{k\pi\beta^2 Z}{d}\right)e^{-t\alpha\left(\frac{k\pi\beta^2}{d}\right)^2}\right) \tag{5.24}$$

Since the heat absorption length, δ is assumed to be very small, $\frac{\sin(\frac{k\pi\delta}{d})}{\frac{k\pi\delta}{d}} \to 1$. Thus 5.24 reduces to,

$$T_Z = T_0\frac{\delta}{d}\left(1 + \sum_{k=1}^{\infty} 2\cos\left(\frac{k\pi\beta^2 Z}{d}\right)e^{-t\alpha\left(\frac{k\pi\beta^2}{d}\right)^2}\right) \tag{5.25}$$

The overall effect of the virtual source, T is obtained as the product of T_X, T_Y and T_Z which are obtained from Equations 5.17, 5.18 and 5.25. Thus,

$$\begin{aligned} T = \; & \tfrac{ab}{h_1 h_2 d}\delta T_0(1+\textstyle\sum_{n=1}^{\infty}\tfrac{2h_1}{n\pi a}\sin\left(\tfrac{n\pi a}{h_1}\right)\cos\left(\tfrac{n\pi X}{h_1\beta}\right)e^{-t\alpha\left(\frac{n\pi}{h_1\beta}\right)^2})\times \\ & (1+\textstyle\sum_{m=1}^{\infty}\tfrac{2h_2}{m\pi b}\sin\left(\tfrac{m\pi b}{h_2}\right)\cos\left(\tfrac{m\pi Y}{h_2\beta}\right)e^{-t\alpha\left(\frac{m\pi}{h_2\beta}\right)^2})\times \\ & (1+\textstyle\sum_{k=1}^{\infty}2\cos\left(\tfrac{k\pi\beta^2 Z}{d}\right)e^{-t\alpha\left(\frac{k\pi\beta^2}{d}\right)^2}) \end{aligned} \tag{5.26}$$

where δ and T_0 are scaling factors and can be factored out by assuming that T_0 is unity and δ is a constant absorption thickness. Of particular interest is the effect of virtual source at a point on the surface, directly above the defective area, which is the excess temperature, T_e. By letting, $X = 0, Y = 0, Z = \frac{d}{\beta^2}$,

$$\begin{aligned} T_e = \; & \tfrac{ab}{h_1 h_2 d}\delta T_0(1+\textstyle\sum_{n=1}^{\infty}\tfrac{2h_1}{n\pi a}\sin\left(\tfrac{n\pi a}{h_1}\right)e^{-t\alpha\left(\frac{n\pi}{h_1\beta}\right)^2})\times \\ & (1+\textstyle\sum_{m=1}^{\infty}\tfrac{2h_2}{m\pi b}\sin\left(\tfrac{m\pi b}{h_2}\right)e^{-t\alpha\left(\frac{m\pi}{h_2\beta}\right)^2})\times \\ & (1+\textstyle\sum_{k=1}^{\infty}2(-1)^k e^{-t\alpha\left(\frac{k\pi\beta^2}{d}\right)^2}) \end{aligned} \tag{5.27}$$

Equation 5.27 represents the excess temperature on the surface of the test specimen caused by the presence of an underlying defect. The defect is present at a depth d from the surface and the defect area is $2a \times 2b$. Thus, given the dimensions and the thermal properties of the test specimen, using the excess temperature, the dimensions and the depth of the defect can be estimated using Equation 5.27

The thermal and mechanical properties of the CFRP (Carbon Fiber Reinforced Plastic) plate tested experimentally are taken from literature [65, 96]. The longitudinal Thermal Conductivity of the plate, K_p is 48 $W/m.K$. The transverse Thermal Conductivity of the plate, K_z is 0.3 $W/m.K$. The density of CFRP material, ρ is 2000 Kg/m^3 and the Specific Heat Conductivity, C is 1000 $J/Kg.K$. Since, $\beta = \left(\frac{K_z}{K_p}\right)^{\frac{1}{6}}$, using values of K_z and K_p, the value of β was calculated as 0.43. Since $\alpha = \frac{\left(K_p^2 K_z\right)^{\frac{1}{3}}}{\rho c}$, the value of α was calculated as $0.44 \times 10^{-5} m^2/s$.

Using Equation 5.27, the excess temperature is calculated and presented in Figures 5.5 and 5.6. Figure 5.5 compares the excess temperature that was obtained over regions containing defects of three different size at the same depth. The dimensions of the defects modeled were 12mmx12mm, 25mmx25mm and 37mmx37mm,

respectively. All the three defects were present at a depth of 3mm from the surface. Note that the excess temperature corresponding to the larger defect has higher magnitude overall. This is due to the fact that the larger defect offers more resistance to the flow of heat than a smaller defect. Figure 5.6 compares the excess temperature that was obtained over regions containing defects of the same size, but present at different depths from the top surface. The dimensions of the defects were 25mmx25mm and were present at depths 2mm, 3mm and 4mm from the surface, respectively. The shallowest defect has the most excess temperature when compared to the deeper defects due to the fact that it offers the most resistance to the flow of heat when compared to the other defects.

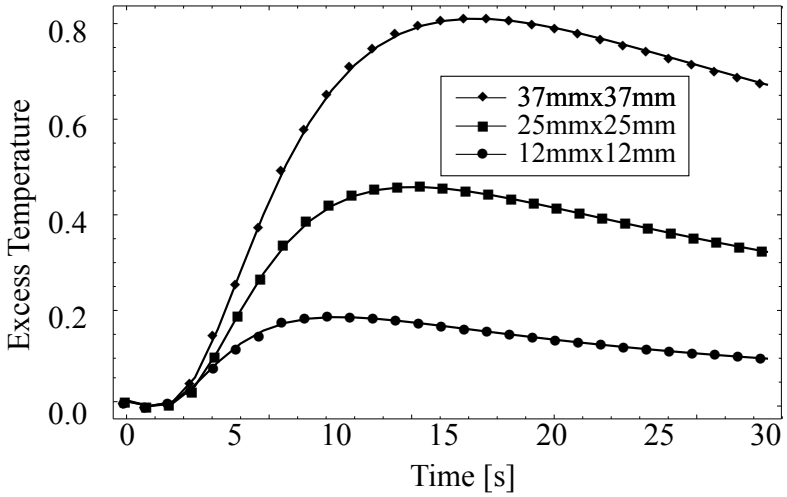

Figure 5.5: Comparison of excess temperature that was obtained at the surface of locations containing rectangular flat-bottom defects of size 12mmx12mm, 25mmx25mm and 37mmx37mm at a depth of 3mm from the surface

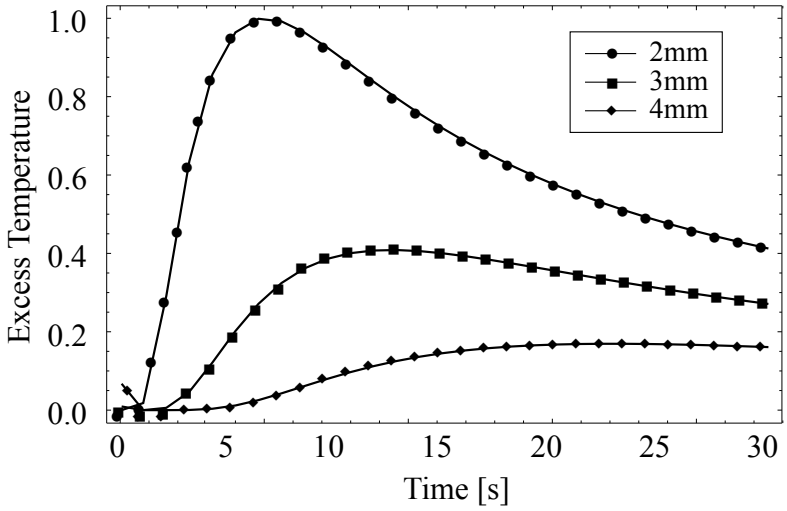

Figure 5.6: Comparison of excess temperature that was obtained at the surface of locations containing rectangular flat-bottom defects at depths 2mm, 3mm and 4mm from the surface. All the three defects were 25mmx25mm

5.4 Experimental Setup and Results

The experimental setup used for the Pulsed Thermography experiments is shown in Figure 5.7. A Speedotron^{TM} 4800W power pack was used to trigger two strobes which output 2400W each with a flash duration of 1/300s. In order to have a fairly uniform heating profile on the surface, the two strobes were placed symmetrically with respect to the test specimen. The strobes cause an instantaneous temperature increase, followed by cooling due to diffusion of heat into the interior. The cooling trend is captured by the FLIR^{TM} A320G Infrared camera which acquires data at 60Hz. The detector is a focal plane array uncooled microbolometer with a spectral range of $7.5 - 13\mu m$ and the resolution is 240x320 pixels. The detector pitch is $25\mu m$ and the detector time constant is $12ms$. The Thermal Sensitivity of the camera is 50mK. The focal length of the lens is $18mm$ and the f-number is 1.3 with a spatial resolution of 1.3 mrad. The 16 bit data was transferred to a laptop via ethernet where it is further processed.

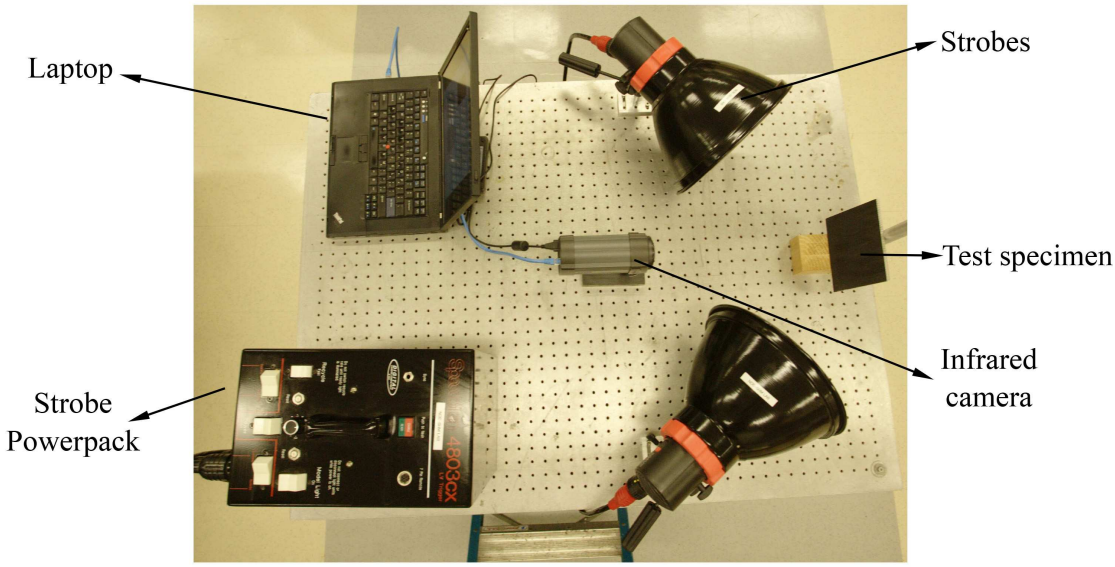

Figure 5.7: Pulsed thermography experimental setup that is used to detect defects in composite test specimen

Detailed experiments were performed on a composite panel containing rectangular flat-bottom holes of different sizes and depths as shown in Figure 5.8. The quasi-isotropic composite plate contained layers that were oriented in the $[0/-45°/+45°/90°]$ directions. The panel was 6mm thick and contained rectangular flat-bottom defects at depths of 2mm, 3mm, 4mm and 5mm from the top surface. The dimensions of the defects were 12mmx12mm, 25mmx25mm and 37mmx37mm. Table 5.1 contains the depth and size information about the nine defects present in the composite panel. The defect indices are marked as shown in Figure 5.8. A picture of the composite panel containing defects is shown in Figure 5.9. However, it is to be noted that Pulsed Thermography experiments were performed on the other side of the panel, where the defects are not visible. The surface of the composite panel was coated with a thin layer of black paint to improve the heat absorption at the surface when a thermal loading is applied. The front and back surfaces of the composite test specimen are assumed to be insulated in the proposed heat diffusion model. In reality, there is a small convective heat loss to the surroundings.

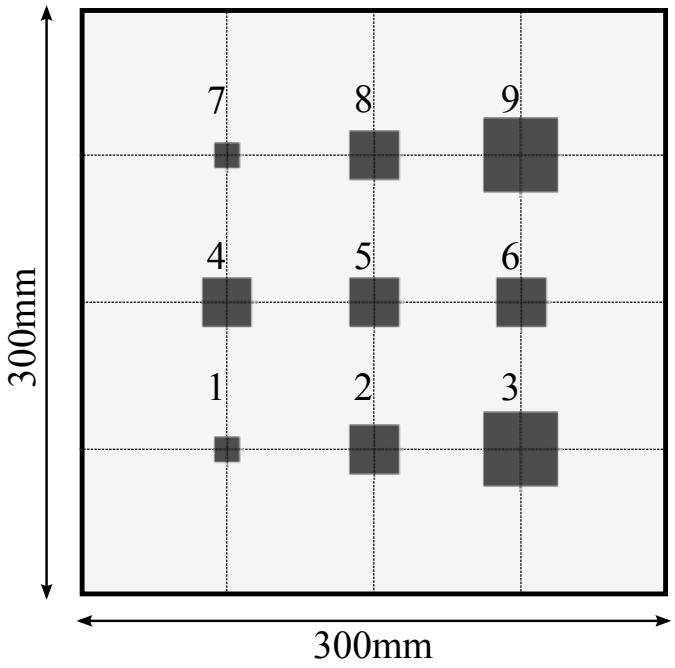

Figure 5.8: Schematic of the composite panel consisting of rectangular flat-bottom holes of different sizes, present at different depths

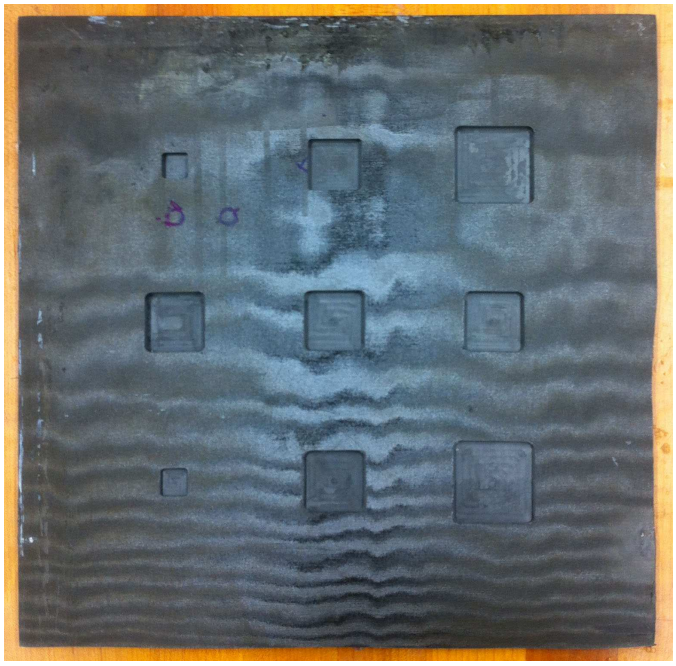

Figure 5.9: The composite panel consisting of rectangular flat-bottom holes of different sizes, present at different depths

Table 5.1: Defect depth and size of the 9 rectangular flat-bottom defects present in the composite panel

Defect Index	Defect Dimensions	Defect Depth
1	12mmx12mm	3mm
2	25mmx25mm	3mm
3	37mmx37mm	3mm
4	25mmx25mm	2mm
5	25mmx25mm	3mm
6	25mmx25mm	4mm
7	12mmx12mm	5mm
8	25mmx25mm	5mm
9	37mmx37mm	5mm

In the Pulsed Thermography process, the data was acquired for a period of 30 seconds after the composite panel was subjected to thermal loading. The camera was operated at a speed of 15Hz. The excess temperature was computed by calculating the average temperature profile within an area of interest and subtracting from it the average temperature profile of an equivalent area surrounding the area of interest. Figure 5.10 compares the experimentally obtained excess temperature that was obtained over regions containing defects of three different size at the same depth. The dimensions of the defects modeled were 12mmx12mm, 25mmx25mm and 37mmx37mm, respectively. All the three defects were present at a depth of 3mm from the surface. As noted before from Figure 5.5, the largest defect offers the most resistance to the flow of heat and hence, the maximum excess temperature when compared to the smaller defects. Figure 5.11 compares the experimentally obtained excess temperature that was obtained over regions containing defects of the same size at three different depths from the surface. The dimensions of the defects were 25mmx25mm and they were present at depths of 2mm, 3mm and 4mm, respectively, from the surface. Similar to the modeled results, as shown in Figure 5.6, the shallowest defect offers most resistance to the heat flow, causing the highest excess temperature relative to the deeper defects.

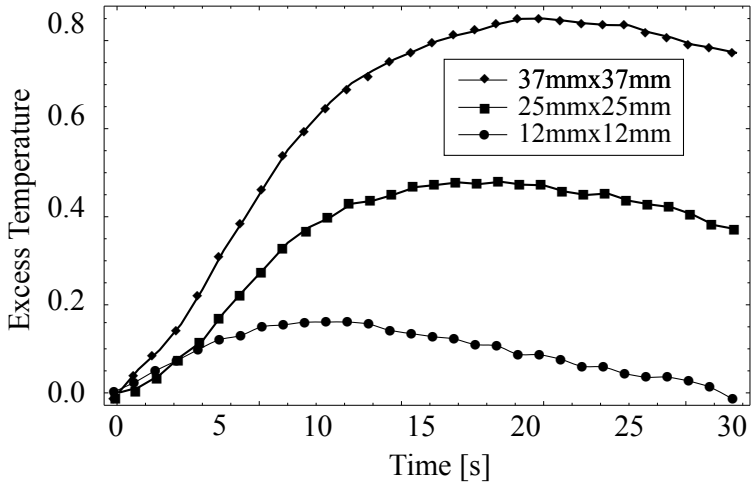

Figure 5.10: Comparison of experimentally obtained excess temperature obtained over rectangular flat-bottom defects that are 12mmx12mm, 25mmx25mm and 37mmx37mm at a depth of 3mm from the surface

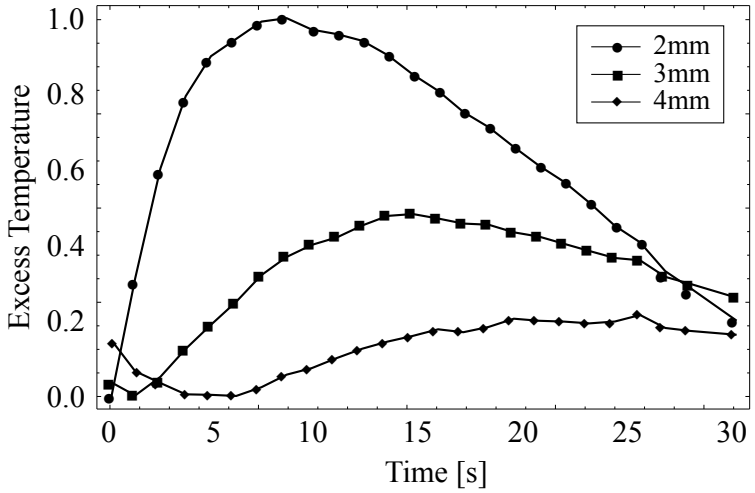

Figure 5.11: Comparison of experimentally obtained excess temperature obtained over rectangular flat-bottom defects that are 25mmx25mm at depths of 2mm, 3mm and 4mm from the surface

The model predicted excess temperature is compared with the experimentally computed excess temperature for the defects 1-6 as shown in Figures 5.12-5.17. In all cases, there is a reasonably good match between the theory and experiments, validating the proposed model. The thickness and depth of defects 7–9 could not

be estimated accurately. These defects did not present any excess temperature, and hence the depth and size could not be estimated for these defects. This could be because of the limitations of the Pulsed Thermography setup that was used in the experiments.

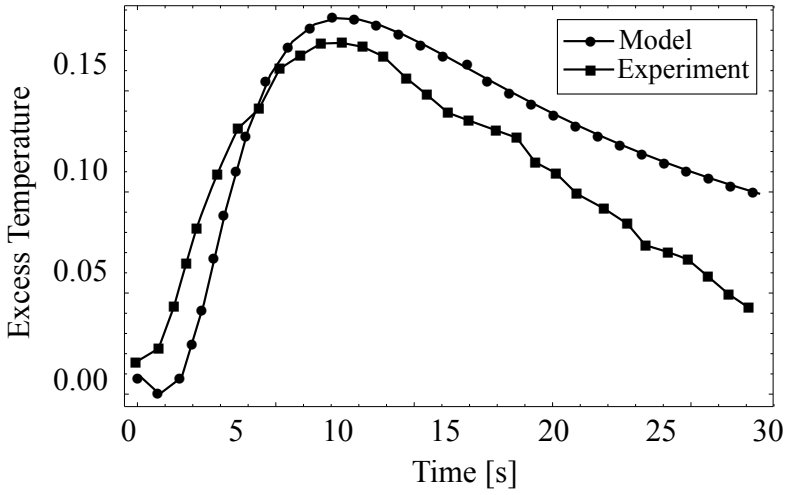

Figure 5.12: Comparison of experimentally obtained excess temperature and model predicted excess temperature over a location containing a 12mmx12mm rectangular flat-bottom hole at a depth of 3mm from the surface

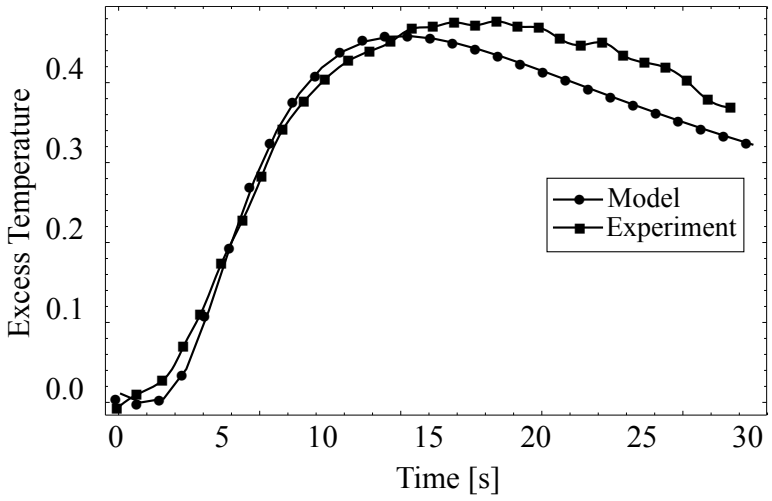

Figure 5.13: Comparison of experimentally obtained excess temperature and model predicted excess temperature over a location containing a 25mmx25mm rectangular flat-bottom hole at a depth of 3mm from the surface

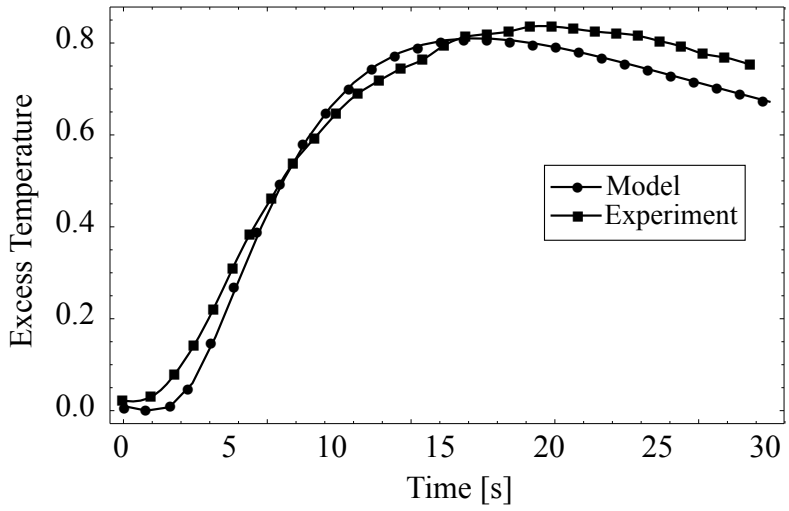

Figure 5.14: Comparison of experimentally obtained excess temperature and model predicted excess temperature over a location containing a 37mmx37mm rectangular flat-bottom hole at a depth of 3mm from the surface

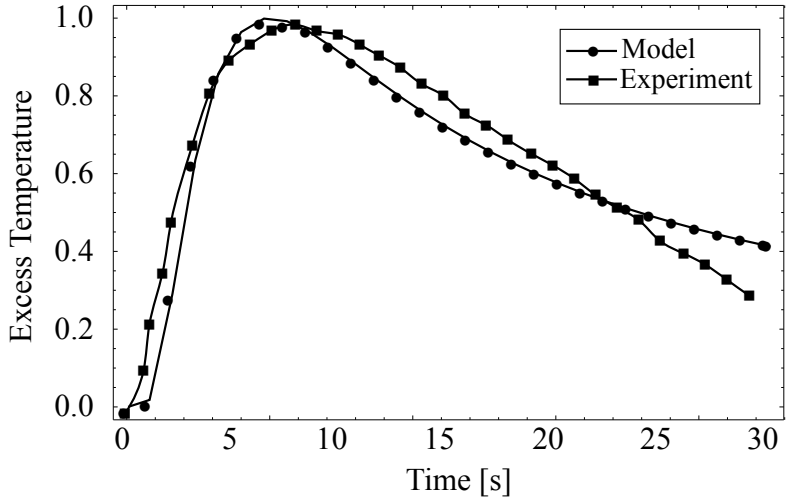

Figure 5.15: Comparison of experimentally obtained excess temperature and model predicted excess temperature over a location containing a 25mmx25mm rectangular flat-bottom hole at a depth of 2mm from the surface

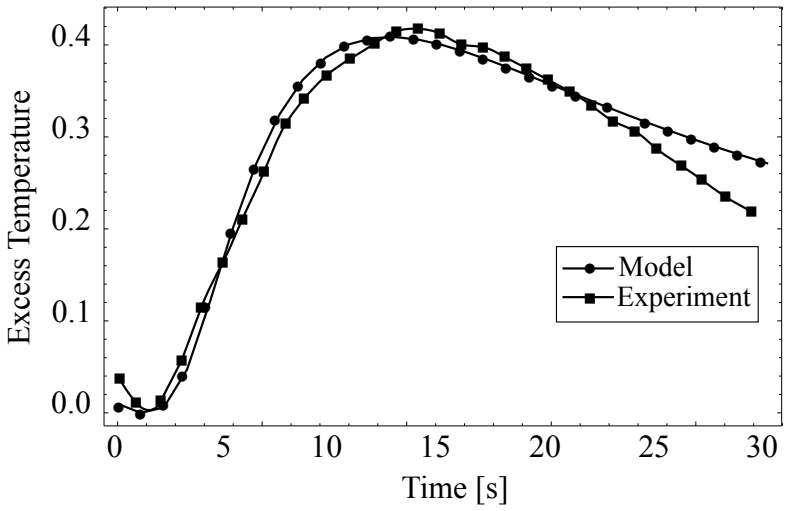

Figure 5.16: Comparison of experimentally obtained excess temperature and model predicted excess temperature over a location containing a 25mmx25mm rectangular flat-bottom hole at a depth of 3mm from the surface

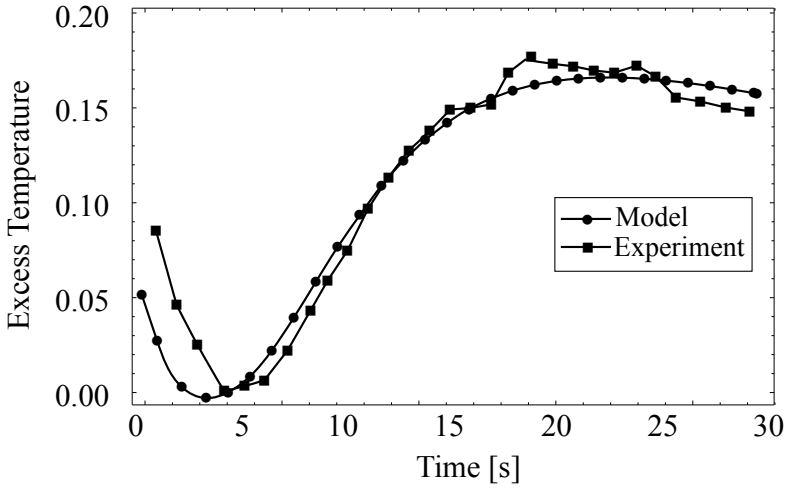

Figure 5.17: Comparison of experimentally obtained excess temperature and model predicted excess temperature over a location containing a 25mmx25mm rectangular flat-bottom hole at a depth of 4mm from the surface

5.5 Conclusions

A novel approach based on 3D heat conduction was developed to estimate the defect depth and size in quasi-isotropic composite structures. Based on the cooling curve obtained over a defective area with respect to the sound area, referred to as "excess temperature", the author has proposed a method to accurately determine the defect size and depth in quasi-isotropic composites containing rectangular defects. The heat flow interaction with extended defects was modeled and a closed-form analytical solution was derived to represent the excess temperature obtained over a defective area with respect to a sound area. The modeling process involved extensive coordinate transformations to reduce the anisotropic heat conduction problem to the isotropic domain, followed by separation of variables to solve the partial differential equation. The results of the model were compared with detailed Pulsed Thermography experiments that were performed on a 6mm thick quasi-isotropic composite panel containing rectangular flat-bottom holes of different sizes, present at different depths. The experimental results obtained sufficiently validated the model.

In the presented study, the calculation of the excess temperature is a critical step, which is used in the estimation of defect depth and size. The excess temperature is calculated as the temperature profile that is obtained over a defective area with respect to the sound area. Hence, there is need for a reference area for the proposed approach to work. The accuracy of results presented in this study could be affected by a variety of factors. Non-uniform heating of the front surface could potentially affect the accuracy of the results. Though, care was taken to ensure uniform heating by placing the strobes symmetrically, perfectly uniform heating is very difficult to achieve in a practical scenario. The Infrared camera used in the tests had a thermal sensitivity of about 50mK which is quite low compared to the more costly Infrared cameras that are typically used in Pulsed Thermography experiments, which have a thermal sensitivity of about 18mK. In the modeling process, perfectly insulated boundary conditions were assumed, whereas, in reality there is a small convective heat loss to the surroundings which could cause minor errors in the predicted excess temperature. The calculation of the exact values of

longitudinal thermal conductivity, K_p, and transverse thermal conductivity, K_z, of plate is beyond the scope of this study. The values of K_p and K_z for quasi-isotropic CFRP plates were taken from literature. The lack of exact values could affect the accuracy of the results.

5.6 Acknowledgements

The authors would like to thank the National Science Foundation (Grant #1028365, Dr. George Maracas – Program Manager) and the von Liebig center at the University of California, San Diego. This chapter, in part, has been submitted for publication in the Experimental Mechanics journal, Manohar, Arun; Lanza di Scalea, Francesco; (2012). The title of this paper is *Estimation of Defect Size and Depth in Quasi-Isotropic Composite Materials Using Infrared Thermography.* The dissertation author was the primary investigator and primary author of this paper.

Chapter 6

Conclusions and Suggestions for Future Work

NDT is a critical tool to increase the useful service life of critical structures. The potential of active Infrared Thermography as a NDT technique was explored and furthered in this dissertation. Infrared Thermography is an appealing NDT technique because it is non-contact, and it has full-field defect imaging capability. Two problems in the field of Infrared Thermography NDT were explored in this dissertation. The first problem dealt with the detection of defects using two different techniques – Pulsed Thermography and Lock-In Thermography. The second problem was the estimation of defect parameters like size and depth using Infrared Thermography.

A Wavelet-aided Multivariate Outlier Analysis was developed for enhancing the contrast of raw thermal images. The method was able to function without a reference frame. In the first stage, the raw thermal curve at each pixel was filtered using Wavelet processing. In the second stage, Multivariate Outlier Analysis was performed on the Wavelet filtered data using a specific set of signal features. Five features, based on the cooling curve and on the rate of cooling curve, were chosen and used. Based on the results presented on a composite plate with delaminations and on a sandwich plate with skin-core disbonds, it was clear that the two-stage approach substantially increased the contrast of the defective areas.

As in other applications of Multivariate Outlier Analysis, different types and number of features can be chosen. Future studies could be conducted in a parametric manner, to identify optimum feature combinations from the Wavelet processed thermal images for maximizing the contrast of defects.

A novel approach combining Lock-In Infrared Thermography, image processing and statistical analysis addressed the problem of defect detection on a composite wind turbine blade. Sixteen defects located in a CX-100 wind turbine blade were considered in the study. Since "blind frequencies" affected defect detection, Lock-In tests were performed at five different frequencies at each defect location, to ensure that any defect could be detected by at least one of the Lock-In frequencies. Multivariate Outlier Analysis was then performed on the spatially registered multi-frequency Lock-In data to combine in a statistically robust manner, the defect detection performance of the multiple Lock-In frequencies. Prior

to the application of Multivariate Outlier Analysis, image processing algorithms including binarization and morphological operations were performed on the raw Lock-In thermal phase images. The defect detection performance of the single Lock-In frequencies, and the combined MOA, for various detection thresholds, was quantified via Receiver Operating Characteristic (ROC) curves for the sixteen test defects. The ROC results demonstrate that the approach of sweeping multiple Lock-In frequencies and combining the phase image results via MOA provides the best overall defect detection performance compared to any single Lock-In frequency. This result is important in Infrared Thermographic detection of defects in composite structures, where Lock-In schemes are necessary to ensure enough penetration. The effectiveness of the MOA applied to Lock-In thermal phase images derives from (1) the statistical addition of defect contrast yielded by multiple Lock-In frequencies, and (2) the mitigation of the "blind frequency" problem affecting conventional Lock-In Thermography because several Lock-In frequencies are applied at each of the defective areas.

However, the detection of defects using Lock-In thermography was a rather slow process. A bulk of the time was spent in the data acquisition process. This could be a concern for deeper defects, since very low Lock-In frequencies are needed to achieve the required thermal diffusion length, especially when five different Lock-In frequencies are used at each location. In a typical carbon fiber composite material, to achieve a thermal diffusion length of about 1", a 1mHz Lock-In frequency needs to be used. The time period is 1000s, corresponding to an acquisition time as long as 3000s. Hence, there is a trade-off between depth of defects targeted and inspection time.

Defect depth and size estimation in Pulsed Infrared Thermography is usually based on 1D heat conduction models. However, 1D heat conduction based models are generally inadequate in predicting the heat flow around defects, especially in composites. A novel method based on virtual heat sources was proposed to account for the 2D axisymmetric heat diffusion around defects and accurately predict the defect depth and size using Pulsed Thermography. The model predictions of surface temperature cooling trends were compared to experimental results

obtained on a stainless steel plate specimen with flat-bottom holes drilled at different depths. The match was found to be quite satisfactory, validating the model. Due to the low Thermal Sensitivity of the Infrared camera that was used, the two deepest defects could not be detected in the experiments. The model uses values of defect depth and defect size independently, and it can therefore be parameterized to predict both of these quantities.

The presented study could only model the presence of circular flat-bottom holes and circular cracks that are oriented parallel to the specimen surface. In the future, the model could be extended to deal with defects of different geometries, present at arbitrary orientations.

Subsequently, the approach was extended to model 3D heat flow in quasi-isotropic composite structures to estimate the defect depth and size. Based on the cooling curve obtained over a defective area with respect to the sound area, referred to as "excess temperature", a method to accurately determine the defect size and depth in quasi-isotropic composites containing rectangular defects was developed. The heat flow interaction with extended defects was modeled and a closed-form analytical solution was derived to represent the excess temperature obtained over a defective area with respect to a sound area. The modeling process involved coordinate transformations to reduce the anisotropic heat conduction problem to the isotropic domain, followed by separation of variables to solve the partial differential equation. The results of the model were compared with Pulsed Thermography experiments that were performed on a 6mm thick quasi-isotropic composite panel containing rectangular flat-bottom holes of different sizes, present at different depths. The experimental results obtained sufficiently validated the model. Again, due to the low Thermal Sensitivity of the Infrared camera that was used, the three deepest defects could not be detected in the experiments. In the presented study, the calculation of excess temperature was a critical step, which is used in the estimation of defect depth and size. The excess temperature was calculated as the temperature profile that is obtained over a defective area with respect to the sound area. Hence, there is need for a reference area for the proposed approach to work.

In spite of the promising results and the ease of use, Infrared Thermography does suffer from a few limitations. One of the biggest concerns is the difficulty to deposit, uniformly, a large amount of thermal energy, in short period of time, over a large surface. Non-uniform heating of the front surface could potentially affect the accuracy of the results. In the experiments, care was taken to ensure uniform heating by placing the strobes symmetrically. However, perfectly uniform heating is very difficult to achieve in a practical scenario. In the future, the output of the symmetrically placed strobes could be passed through a grid spot to ensure a perfectly uniform heat front. A large amount of energy needs to be deposited in order to ensure that deeper defects are detected with sufficient contrast. However, too much energy could cause permanent damage to the surface. Hence, Infrared Thermography cannot be used to probe very deep into structures. There is a trade-off between detectability of subtle defects and the extent to which the surface can be heated.

In some cases, the cost of the equipment could be substantial. Some of the research-grade infrared cameras cost more than $80,000. However, for the experiments performed in this study, a low cost, micro-bolometer infrared camera was used. The camera had a thermal sensitivity of about 50mK, which is quite low compared to the more costly liquid-cooled infrared cameras that are typically used in Infrared Thermography experiments, which have a thermal sensitivity in the range of 10-20mK. Moreover, the FLIR^{TM} A320G camera that was in the experiments had a conservative resolution of 240x320pixels, with a maximum frame rate of 60Hz. This is very limiting when compared to the other options available in the market.

Typically, thermal emissivity depends on surface orientation, temperature, and wavelength. For practical reasons, the emissivity is usually considered a constant. This could be a concern in Pulsed Thermography as there is a large variation in the surface temperature of the test specimen. Assuming a constant value of emissivity could affect the accuracy of the results. Using emissivity as a function of temperature could boost the accuracy of the models in future. Usually, the surface of the objects to be inspected is coated with a thin layer of high emis-

sivity black paint to improve the heat absorption at the surface and to minimize the perturbations caused by surrounding objects. However, this may not always possible.

The accuracy of defect quantification results presented in this study could be affected by a variety of factors. In the modeling process, all the heat that was deposited on the surface was assumed to heat the interior by conduction. No convective and radiative losses were accounted for. In reality, a small amount of energy is always lost to the surroundings. Perfectly insulated boundary conditions were assumed, which could cause minor errors in the predicted excess temperature. More accurate results could be obtained by accommodating convective and radiative boundary conditions in the future.

The calculation of the exact values of longitudinal thermal conductivity, K_p, and transverse thermal conductivity, K_z, of the composite plate was beyond the scope of this dissertation. The values of K_p and K_z for quasi-isotropic CFRP plates were taken from literature. The calculation of exact values could improve the accuracy of the results and could be attempted in a future work. Moreover, the defects were assumed not to interact with each other in the modeling process. The interaction of heat flow with multiple defects in a finite space could be modeled in future.

Bibliography

[1] L. Cartz. *Nondestructive testing*. ASM International, Materials Park, OH (United States), 1995.

[2] C. Hellier. *Handbook of Nondestructive Evaluation*. McGraw-Hill, 2001.

[3] J. Blitz and G. Simpson. *Ultrasonic methods of Nondestructive Testing*, volume 2. Springer, 1995.

[4] G. Wang and T.W. Liao. Automatic identification of different types of welding defects in radiographic images. *Ndt & E International*, 35(8):519–528, 2002.

[5] J. Blitz. *Electrical and magnetic methods of non-destructive testing*, volume 3. Springer, 1997.

[6] P.J. Shull. *Nondestructive evaluation: theory, techniques, and applications*, volume 142. CRC, 2002.

[7] A. Sophian, G.Y. Tian, D. Taylor, and J. Rudlin. A feature extraction technique based on principal component analysis for pulsed eddy current ndt. *NDT & E International*, 36(1):37–41, 2003.

[8] YY Hung. Shearography: a new optical method for strain measurement and nondestructive testing. *Optical Engineering*, 21(3):213391–213391, 1982.

[9] R.K. Miller and P. McIntire. Nondestructive testing handbook. vol. 5: Acoustic emission testing. *American Society for Nondestructive Testing, 1987,*, page 603, 1987.

[10] X. Maldague, editor. *Infrared Methodology and Technology*, volume 7. Gordon and Breach Science Publishers, 1994.

[11] A.G Beattie and M. Rumsey. Evaluation of Wind Turbine Blades Using an Infrared Camera. *AIAA*, pages 1–8, 1999.

[12] MR Clark, DM McCann, and MC Forde. Application of infrared thermography to the non-destructive testing of concrete and masonry bridges. *NDT & E International*, 36(4):265–275, 2003.

[13] V.S. Ghali, N. Jonnalagadda, and R. Mulaveesala. Three-dimensional pulse compression for infrared nondestructive testing. *Sensors Journal, IEEE*, 9(7):832–833, 2009.

[14] C. Ibarra-Castanedo, D. Gonzalez, M. Klein, M. Pilla, S. Vallerand, and X. Maldague. Infrared image processing and data analysis. *Infrared physics & technology*, 46(1):75–83, 2004.

[15] C. Ibarra-Castanedo and X. Maldague. Pulsed phase thermography reviewed. *Quantitative Infrared Thermography Journal*, 1(1):47–70, 2004.

[16] T. Inagaki, T. Ishii, and T. Iwamoto. On the ndt and e for the diagnosis of defects using infrared thermography. *NDT & E international*, 32(5):247–257, 1999.

[17] X.P.V. Maldague. Introduction to ndt by active infrared thermography. *Materials Evaluation*, 60(9):1060–1073, 2002.

[18] X. Maldague, F. Galmiche, and A. Ziadi. Advances in pulsed phase thermography. *Infrared Physics & Technology*, 43(3):175–181, 2002.

[19] X. P. V. Maldague and S. Marinetti. Pulse phase infrared thermography. *Journal of Applied Physics*, 79(5):2694–2698, 1996.

[20] A. Manohar and F. Lanza di Scalea. Determination of defect depth and size using virtual heat sources in pulsed infrared thermography. *Experimental Mechanics*, pages 1–11, 2012. 10.1007/s11340-012-9670-9.

[21] A. Manohar and F. Lanza di Scalea. Wavelet-aided multivariate outlier analysis to enhance defect contrast in thermal images. *Experimental Techniques*, 2011.

[22] S. Marinetti, E. Grinzato, P.G. Bison, E. Bozzi, M. Chimenti, G. Pieri, and O. Salvetti. Statistical analysis of ir thermographic sequences by pca. *Infrared Physics & Technology*, 46(1-2):85–91, December 2004.

[23] C. Meola and G.M. Carlomagno. Recent advances in the use of infrared thermography. *Measurement science and technology*, 15(9):R27, 2004.

[24] M. Omar, MI Hassan, K. Saito, and R. Alloo. Ir self-referencing thermography for detection of in-depth defects. *Infrared physics & technology*, 46(4):283–289, 2005.

[25] M.A. Omar, R. Parvataneni, and Y. Zhou. A combined approach of self-referencing and Principle Component Thermography for transient, steady, and selective heating scenarios. *Infrared Physics & Technology*, 53(5):358–362, September 2010.

[26] S. Pickering and D. Almond. Matched excitation energy comparison of the pulse and lock-in thermography nde techniques. *NDT & E International*, 41(7):501 – 509, 2008.

[27] M. Pilla, M. Klein, X. Maldague, and A. Salerno. New absolute contrast for pulsed thermography. *Quantitative Infrared Thermography*, pages 53–58, 2002.

[28] T. Sakagami. Applications of pulse heating thermography and lock-in thermography to quantitative nondestructive evaluations. *Infrared Physics & Technology*, 43(3-5):211–218, June 2002.

[29] S. Shepard and R.J. Ducar. Quantitative infrared defect detection in composite aerospace structures. *Society for the Advancement of Material and Process Engineering, Bridging the Centuries with SAMPE's Materials and Processes Technology,*, 45:1282–1290, 2000.

[30] E. Grinzato and V. Vavilov. Corrosion evaluation by thermal image processing and 3D modelling. *Revue Générale de Thermique*, 37(8):669–679, September 1998.

[31] C. Ibarra-Castanedo, P. Jean-Marc, S. Guilbert, N. P. Avdelidis, M. Genest, A. Bendada, and X. P. V. Maldague. Comparative study of active thermography techniques for the nondestructive evaluation of honeycomb structures. *Research in Nondestructive Evaluation*, 20:1–31, 2009.

[32] S. M. Shepard, J. R. Lhota, B. A. Rubadeux, D. Wang, and T. Ahmed. Reconstruction and enhancement of active thermographic image sequences. *Optical Engineering*, 42(5):1337–1342, 2003.

[33] J.M. Spicer and R. Osiander. Active thermography. *International journal of occupational safety and ergonomics : JOSE*, 15(4):363–71, January 2002.

[34] M.W. Burke. Status of vibroir at lawrence livermore national laboratory. *Proceedings of SPIE*, pages 313–321, 2004.

[35] J. Rantala, D. Wu, and G. Busse. Amplitude-modulated lock-in vibrothermography for nde of polymers and composites. *Research in Nondestructive Evaluation*, 7(4):215–228, 1996.

[36] T. J. Barden, D. P. Almond, S. G. Pickering, M. Morbidini, and P. Cawley. Detection of impact damage in CFRP composites by thermosonics. *Nondestructive Testing and Evaluation*, 22(2):71–82, June 2007.

[37] J.C. Chen, J. Kephart, K. Lick, and W.T. Riddell. Crack growth induced by sonic IR inspection. *Nondestructive Testing and Evaluation*, 22(2):83–92, June 2007.

[38] M. Morbidini and P. Cawley. The relationship between vibration level and minimum detectable defect size in sonic-ir inspection. *ECNDT*, pages 1–9, 2006.

[39] M. Morbidini, P. Cawley, T. Barden, D. Almond, and P. Duffour. Prediction of the thermosonic signal from fatigue cracks in metals using vibration damping measurements. *Journal of Applied Physics*, 100(10):1–10, 2006.

[40] NP Avdelidis and D.P. Almond. Through skin sensing assessment of aircraft structures using pulsed thermography. *NDT & E International*, 37(5):353–359, 2004.

[41] K. Chatterjee, S. Tuli, S.G. Pickering, and D.P. Almond. A comparison of the pulsed, lock-in and frequency modulated thermography nondestructive evaluation techniques. *NDT & E International*, 44(7):655 – 667, 2011.

[42] G. Giorleo and C. Meola. Comparison between pulsed and modulated thermography in glass–epoxy laminates. *NDT & E International*, 35(5):287–292, 2002.

[43] D. Gonzalez, C. Ibarra-castanedo, J. Lopezhiguera, and X Maldague. New algorithm based on the Hough transform for the analysis of pulsed thermographic sequences. *NDT & E International*, 39(8):617–621, December 2006.

[44] M.Y.Y. Hung, Y.S. Chen, S.P. Ng, S.M. Shepard, Y. Hou, and J.R. Lhota. Review and comparison of shearography and pulsed thermography for adhesive bond evaluation. *Optical engineering*, 46(5):051007–051007, 2007.

[45] C. Ibarra-Castanedo, M. Genest, P. Servais, X. P. V. Maldague, and A. Bendada. Qualitative and quantitative assessment of aerospace structures by pulsed thermography. *Nondestructive Testing and Evaluation*, 22(2-3):199–215, 2007.

[46] JA Schroeder, T. Ahmed, B. Chaudhry, and S. Shepard. Non-destructive testing of structural composites and adhesively bonded composite joints: pulsed thermography. *Composites Part A: Applied Science and Manufacturing*, 33(11):1511–1517, 2002.

[47] S. M. Shepard. Advances in pulsed thermography. *Thermosense XXIII*, 4360(1):511–515, 2001.

[48] J. G. Sun. Analysis of pulsed thermography methods for defect depth prediction. *Journal of Heat Transfer*, 128(4):329–338, 2006.

[49] S. Vallerand and X. Maldague. Defect characterization in pulsed thermography: a statistical method compared with kohonen and perceptron neural networks. *NDT & E International*, 33(5):307–315, 2000.

[50] F. Galmiche, X. Maldague, S. Valler, and J.P. Couturier. Pulsed phased thermography with the wavelet transform. In *American Institute of Physics Conference Series*, volume 509, pages 609–616, 2000.

[51] W. Bai and B.S. Wong. Evaluation of defects in composite plates under convective environments using lock-in thermography. *Measurement Science and Technology*, 12(2):142, 2001.

[52] C. Meola, G.M. Carlomagno, A. Squillace, and A. Vitiello. Non-destructive evaluation of aerospace materials with lock-in thermography. *Engineering Failure Analysis*, 13(3):380 – 388, 2006. Papers presented at the First International Conference on Engineering Failure Analysis Part III.

[53] D. Wu and G. Busse. Lock-in thermography for nondestructive evaluation of materials. *Revue Gnrale de Thermique*, 37(8):693 – 703, 1998.

[54] V. Vavilov, T. Kauppinen, and E. Grinzato. Thermal Characterization of Defects in Building Envelopes Using Long Square Pulse and Slow Thermal Wave Techniques. *Research in Nondestructive Evaluation*, 9(4):181–200, 1997.

[55] O. Breitenstein and M. Langenkamp. *Lock-in thermography: basics and use for functional diagnostics of electronic components*, volume 10. Springer Verlag, 2003.

[56] N. Rajic. Principal component thermography for flaw contrast enhancement and flaw depth characterisation in composite structures. *Composite Structures*, 58(4):521–528, December 2002.

[57] A. Yan, G. Kerschen, P. Deboe, and J. Golinval. Structural damage diagnosis under varying environmental conditionspart II: local PCA for non-linear cases. *Mechanical Systems and Signal Processing*, 19(4):865–880, July 2005.

[58] Y. Zhou, A. Mayyas, and M. Omar. Principal Component Analysis-Based Image Fusion Routine with Application to Automotive Stamping Split Detection. *Research in Nondestructive Evaluation*, 22(2):76–91, April 2011.

[59] N Rajic. Principal Component Thermography. Technical report, Aeronautical and Maritime Research Laboratory, 2002.

[60] L.I. Smith. A tutorial on Principal Components Analysis. Technical report, University of Otago, New Zealand, 2002.

[61] D. Bates, G. Smith, D. Lu, and J. Hewitt. Rapid thermal non-destructive testing of aircraft components. *Composites Part B: Engineering*, 31(3):175–185, 2000.

[62] T. D'Orazio, C. Guaragnella, M. Leo, and P. Spagnolo. Defect detection in aircraft composites by using a neural approach in the analysis of thermographic images. *NDT & E International*, 38(8):665–673, 2005.

[63] P.A. Howell. Computational analysis for thermal NDE of composites. *Proceedings of SPIE*, 5191:18–26, 2003.

[64] G. Muzia, Z. M. Rdzawski, M. Rojek, and J. Stabik. Thermographic diagnosis of fatigue degradation of epoxy-glass composites. *Journal of Achievements in Materials and Manufacturing Engineering Volume*, 24(2):123–126, 2007.

[65] C. Silva, E. (Ed) Marotta, M. Schuller, L. Peel, and M. O'Neill. In-Plane Thermal Conductivity in Thin Carbon Fiber Composites. *Journal of Thermophysics and Heat Transfer*, 21(3):460–467, July 2007.

[66] P. Cawley. Inspection of Composites-Current Status and Challenges. In *Proceedings European Conference of Nondestructive Testing*, pages 1–10. Citeseer, 2006.

[67] S. G. Mallat. A theory for multiresolution signal decomposition: The wavelet representation. *IEEE Transactions on Pattern Analysis and Machine Intelligence*, 11(7):674–693, 1989.

[68] P. Rizzo, E. Sorrivi, F. Lanza di scalea, and E. Viola. Wavelet-based outlier analysis for guided wave structural monitoring: Application to multi-wire strands. *Journal of Sound and Vibration*, 307(1-2):52–68, October 2007.

[69] G. Strang and T. Nguyen. *Wavelets and Filter Banks*. Wellesley College, 1996.

[70] R. C. Gonzalez and R. E. Woods. *Digital Image Processing (3rd Edition)*. Prentice-Hall, Inc., Upper Saddle River, NJ, USA, 2006.

[71] V. Barnett and T. Lewis. *Outliers in Statistical Data*. Wiley, 3 edition edition, April 1994.

[72] D. Berry. Cx-100 manufacturing final project report. Technical report, Sandia National Laboratory, 2007.

[73] 20% wind energy by 2030. Technical report, U.S. Department of Energy, July 2008.

[74] C.C. Ciang, J.R. Lee, and H.J. Bang. Structural health monitoring for a wind turbine system: a review of damage detection methods. *Measurement Science and Technology*, 19(12):122001, 2008.

[75] M.C. Garcia, M.A. Sanz-Bobi, and J. del Pico. Simap: Intelligent system for predictive maintenance: Application to the health condition monitoring of a windturbine gearbox. *Computers in Industry*, 57(6):552–568, 2006.

[76] A. Ghoshal, M.J. Sundaresan, M.J. Schulz, and P. Frank Pai. Structural health monitoring techniques for wind turbine blades. *Journal of Wind Engineering and Industrial Aerodynamics*, 85(3):309–324, 2000.

[77] Z. Hameed, YS Hong, YM Cho, SH Ahn, and CK Song. Condition monitoring and fault detection of wind turbines and related algorithms: A review. *Renewable and Sustainable energy reviews*, 13(1):1–39, 2009.

[78] W. Liu, B. Tang, and Y. Jiang. Status and problems of wind turbine structural health monitoring techniques in china. *Renewable Energy*, 35(7):1414–1418, 2010.

[79] M. Rumsey and J. Paquette. Structural health monitoring of wind turbine blades. *Proceedings of SPIE*, 2008.

[80] H. Sutherland and W. Musial. Application of Nondestructive Techniques to the testing of a wind turbine blade. *NDT & E International*, 27(4):209–209, 1994.

[81] J. Tippmann, A. Manohar, and F. Lanza di Scalea. Wind turbine inspection tests at ucsd. *Sensors and Smart Structures Technologies for Civil, Mechanical, and Aerospace Systems 2012*, 8345(1):83451Q, 2012.

[82] D.T. Griffith. Structural Dynamics Analysis and Model Validation of Wind Turbine Structures. In *50th AIAA/ASME/ASCE/AHS/ASC Structures, Structural Dynamics, and Materials Conference*, number May, 2009.

[83] B. Lu, Y. Li, X. Wu, and Z. Yang. A review of recent advances in wind turbine condition monitoring and fault diagnosis. In *Power Electronics and Machines in Wind Applications, 2009. PEMWA 2009. IEEE*, pages 1–7. IEEE, 2009.

[84] M. Rumsey. Sensor Systems and Applications. In *2010 Wind Turbine Blade Workshop*, 2010.

[85] M. Rumsey. Condition Monitoring and Wind Turbine Blades. In *Wind Turbine Reliability Workshop*. Sandia, 2009.

[86] M. Rumsey, J. Paquette, J.R. White, R.J. Werlink, A.G. Beattie, C.W. Pitchford, and J. van Dam. Experimental Results of Structural Health Monitoring of Wind Turbine Blades. In *46th AIAA Aerospace Sciences Meeting and Exhibit, Reno, NV*, pages 1–14, 2008.

[87] C. Pitchford. *Impedance-based structural health monitoring of wind turbine blades*. PhD thesis, Viriginia Polytechnic Institute and State University, 2007.

[88] D. Roach, K. Rackoq, and R. Duvall. Addressing the need for nondestructive inspection of wind turbine blades. Technical report, Sandia National Laboratory, 2010.

[89] S. Kay. *Fundamentals of Statistical Signal Processing, Volume II: Detection Theory*. Prentice-Hall, Englewood Cliffs, NJ, 1998.

[90] J. G. Sun. Method for determining defect depth using thermal imaging. *U.S. Patent 6542849*, April 2003.

[91] H. I. Ringermacher and R. J. Archacki Jr. Nondestructive testing: Transient depth thermography. *U.S Patent 5711603*, 1998.

[92] W. J. Parker, R. J. Jenkins, C. P. Butler, and G. L. Abbott. Flash method of determining thermal diffusivity, heat capacity and thermal conductivity. *Journal of Applied Physics*, 32(9):1679–1684, September 1961.

[93] H.S. Carslaw and J.C. Jaeger. *Conduction of Heat in Solids*. Oxford science publications. Clarendon Press, 1959.

[94] R. Haberman. *Elementary Applied Partial Differential Equations with Fourier Series and Boundary Value*. Hall, Prentice, 3 edition, 1997.

[95] H.I. Syed. Corrosion detection in aircraft skin. *Proceedings of SPIE*, 1933(1 993):160–165, 1993.

[96] S. F. Shuler, S. G. Advani, and V. N. Kaliakin. Transient analysis and measurement of anisotropic heat conduction in transversely isotropic composite materials. *Journal of Composite Materials*, 33(7):594–613, 1999.

[97] M. Krishnapillai, R. Jones, I. Marshall, M. Bannister, and N. Rajic. Ndte using pulse thermography: Numerical modeling of composite subsurface defects. *Composite Structures*, 75(1-4):241–249, September 2006.

[98] F. Mustapha, G. Manson, S. G. Pierce, and K. Worden. Structural Health Monitoring of an Annular Component using a Statistical Approach. *Strain*, 41(3):117–127, August 2005.

[99] S. Ogihara, M. Okita, T. Chiba, and Shimizu C.J. Experimental and Analytical Investigation of Thermal Conductivity in Carbon Fiber Reinforced Plastics.

[100] XE Gros, J. Bousigue, and K. Takahashi. NDT data fusion at pixel level. *NDT & E International*, 32(5):283–292, 1999.